

Magneto-optics of complex oxides at terahertz frequencies

Samuel Peter Philip Jones
Keble College, University of Oxford

A thesis submitted for the Degree of
Doctor of Philosophy in Condensed Matter Physics

Trinity Term 2014



Abstract

Magneto-optics of complex oxides at terahertz frequencies

Samuel Peter Philip Jones, Keble College, University of Oxford

A thesis submitted for the Degree of Doctor of Philosophy in Condensed Matter Physics, Trinity Term 2014

This thesis presents experimental results on two complex oxide systems: $\text{Cu}_{1-x}\text{Zn}_x\text{O}$ and $\text{La}_{0.7}\text{Sr}_{0.3}\text{MnO}_3:\text{ZnO}$. The dynamic magnetoelectric response of these materials is obtained using terahertz time-domain spectroscopy, supported by Fourier-transform infrared spectroscopy, Raman spectroscopy and X-ray diffraction.

Evidence for an electromagnon in the multiferroic phase of CuO is presented for the first time. This high temperature (213–230 K) electromagnon is linked to intersublattice exchange between two Cu sublattices. The temperature dependence of a magnon in the collinear antiferromagnetic phase is indicative of biquadratic exchange.

Broadening of the multiferroic phase on substitution of copper with zinc is reported along with a 25% depression of the Néel temperature due to spin dilution. Phonons and magnons broaden and shift in energy on alloying. However, the electromagnon is relatively insensitive, increasing in energy without widening. This indicates that electromagnons and dynamic magnetoelectric coupling can be maintained even in disordered spin systems. Strong spin-phonon coupling is present in both magnetically ordered phases as shown by the anomalous behaviour of the A_u^3 phonon at T_{N1} and a Raman-active mode associated with a magnetic modulation of a zone-folded acoustic phonon.

Dynamic 1 THz magnetoresistance is found to be significantly larger than static magnetoresistance in $\text{La}_{0.7}\text{Sr}_{0.3}\text{MnO}_3:\text{ZnO}$ vertically-aligned nanocolumn films on LaAlO_3 substrates. The metal-insulator transition temperature is determined to be 300 K. Temperature dependent static and dynamic resistivity and magnetoresistance are discussed in terms of strain and grain boundary effects. Negative photoconductivity is observed and the dynamic response analysed.

List of publications

- **S. P. P. Jones**, E. M. Choi, A. Chen, Q. X. Jia, J. L. MacManus-Driscoll, J. Lloyd-Hughes *Manuscript in preparation based on Chapter 6*.
- **S. P. P. Jones**, N. Wurz, M. Failla, D. Prabhakaran, C. F. McConville, J. Lloyd-Hughes *Manipulating the multiferroic phase of CuO by non-magnetic zinc substitution: influence on electromagnons and spin-phonon coupling*, Phys. Rev. B **under review** (2014).
- **S. P. P. Jones**, S. M. Gaw, K. I. Doig, D. Prabhakaran, E. M. Hétyó, Wheeler, A. T. Boothroyd, J. Lloyd-Hughes *High temperature electromagnons in the magnetically induced multiferroic cupric oxide driven by intersublattice exchange*, Nat. Commun. **5:3787** (2014).
- J. Lloyd-Hughes, **S. P. P. Jones**, E. Castro-Camus, K. I. Doig, J. L. MacManus-Driscoll *Modifying the polarization state of terahertz radiation using anisotropic twin-domains in LaAlO₃*, Opt. Lett. **39**, 1121 (2014).
- K. I. Doig, F. Aguesse, A. K. Axelsson, N. M. Alford, S. Nawaz, V. R. Palkar, **S. P. P. Jones**, R. D. Johnson, R. A. Synowicki, J. Lloyd-Hughes *Coherent magnon and acoustic phonon dynamics in tetragonal and rare-earth-doped BiFeO₃ multiferroic thin films*, Phys. Rev. B **88**, 094425 (2013).

Acknowledgements

It is my pleasure to thank the many people who have offered help, advice, encouragement and diversion throughout my DPhil. Firstly, my thanks to my supervisor Dr. James Lloyd-Hughes for all his enthusiasm and time since I arrived in Oxford. Thanks to Katie Doig, Callum Docherty and all of the Lloyd-Hughes and Johnston groups for their excellent company. Likewise to my office-mates in 241.2. Ben Williams, Dr. Ben Reid, and Dr. Patrick Parkinson gave their time to read various parts of this thesis, resulting in numerous improvements - thank you.

I am grateful to all those who freely gave of their time and expertise as I learnt new experimental techniques. In Oxford, Fred Wondre and Dr. Roger Johnson for their knowledge of X-rays; Keith Belcher and Dr. Bob Watkins for their care and patience whilst preparing samples. In Warwick, Matthew Dale for his assistance with Raman measurements and Sep Farahani with the FTIR. I am indebted to Dr. Michael Johntson for the use of his laboratory, especially after James moved to Warwick.

My work on cupric oxide would not have been possible without Dr. Dharamalingam Prabhakaran who grew single crystal samples of CuO and $\text{Cu}_{1-x}\text{Zn}_x\text{O}$. I would like to formally acknowledge Stephen Gaw and Prof. Andrew Boothroyd, for performing the inelastic neutron scattering measurements presented in Chapter 4 and, along with Dr. Kun Cao, for many fruitful discussions. I thank Dr. Peter Babkevich for providing the *ac*-plane sample used in Ref. [1].

Chapter 6 was borne out of a collaboration with Prof. Judith MacManus-Driscoll (University of Cambridge). I thank her for this opportunity; Dr. Aiping Chen (Los Alamos National Laboratory) for growing the samples; and Dr. Eun-Mi Choi (Cambridge) for performing the transport measurements.

I would like to acknowledge the EPSRC for financial support, along with Keble College and the IOP for bursaries that enabled me to attend international conferences.

I have been lucky enough to make some good friends in Oxford. I thank you all. To my fellow members of the Falcon Boat Club for many joyful hours out on the Isis; Nick Roberts who got it all started; and especially Michael Wright, a fellow obsessive. To my family for their constant love and support. Diolch o galon Mam a Dad. Lastly to Magnhild. Thank you for everything, my love. I would not have done it without you.

Til Magnhild

Contents

Abstract	i
List of publications	iii
Acknowledgements	v
1 Introduction	1
1.1 Multiferroic materials	2
1.2 Electromagnons	11
1.3 Manganites and the colossal magnetoresistance effect	26
1.3.1 $\text{La}_{0.7}\text{Sr}_{0.3}\text{MnO}_3$	29
1.4 Structure of this thesis	33
2 Magnons and electromagnons	35
2.1 Magnons	36
2.1.1 1-D Heisenberg ferromagnet	37
2.1.2 Turning on the interactions	39
2.1.3 Frequency-dependent permeability tensor	41
2.1.4 Simple collinear antiferromagnet	43
2.1.5 Incommensurate spin cycloid	44
2.2 Electromagnons	47
2.2.1 Dzyaloshinskii-Moriya model	47
2.2.2 Heisenberg model	50
2.3 Summary	55
3 Experimental Methods	57
3.1 Terahertz Time-Domain Spectroscopy	58
3.1.1 Performing a THz-TDS experiment	60
3.1.2 Extracting the complex refractive index	69
3.1.3 Optical pump - THz probe spectroscopy	72
3.2 Fourier Transform Infrared Spectroscopy	76
3.3 Raman Spectroscopy	77

4	Cupric Oxide: electromagnons in a high temperature induced multiferroic	79
4.1	An introduction to CuO	80
4.2	Sample preparation	84
4.3	Room temperature characterisation	85
4.3.1	Contribution of phonons to absorption coefficient	87
4.4	Dynamic magneto-electric response	88
4.5	Electromagnon	90
4.5.1	Electromagnon spectra and oscillator strength	92
4.5.2	Static dielectric constant and spectral weight transfer	94
4.6	Magnon	95
4.6.1	Polarised inelastic neutron scattering	100
4.7	Optical-pump THz-probe spectroscopy	100
4.8	Summary	101
5	Manipulating the multiferroic phase of CuO via Zn alloying	105
5.1	Background: the influence of pressure or alloying	106
5.2	Growth and characterisation	107
5.3	Dynamic magneto-electric response	111
5.3.1	Terahertz-time domain spectroscopy	111
5.3.2	Results: electromagnon	112
5.3.3	Results: magnon	114
5.4	Dynamic lattice response	116
5.4.1	Symmetry analysis	116
5.4.2	FTIR and Raman spectroscopy	117
5.4.3	Results: IR-active phonons	118
5.4.4	Results: Raman-active phonons	122
5.4.5	Discussion: Influence of alloying	126
5.5	Discussion	127
5.6	Summary	128
6	Magnetoresistance in $\text{La}_{0.7}\text{Sr}_{0.3}\text{MnO}_3\text{:ZnO}$ nanocolumnar thin films	131
6.1	$\text{La}_{0.7}\text{Sr}_{0.3}\text{MnO}_3$	131
6.2	Sample preparation and structural characterisation	133
6.3	A. c. and d. c. temperature dependent dielectric response	136
6.4	A. c. and d. c. magnetoconductivity	138
6.5	Pump-probe conductivity	139
6.6	Discussion	140
6.7	Summary	144
7	Conclusions	145

Contents

xi

Bibliography

149

Chapter 1

Introduction

A vast range of materials are labelled ‘complex oxides’, but it is their common exotic electric and magnetic properties that make this an exciting class of substances for a physicist to study. There is no hard and fast definition of a complex oxide but these materials will always consist of oxygen and other (typically, but not necessarily, metallic) ions, usually with highly anisotropic electronic interactions, competition between charge, spin and orbital ordering, and often exhibiting exotic phases of matter. A defining factor is that these are correlated-electron systems with properties that cannot be deduced from simple free-electron or tight-binding models [2]. Complex oxides can be high- T_C superconductors (e.g. $\text{YBa}_2\text{Cu}_4\text{O}_8$), multiferroics (e.g. TbMnO_3 , CuO), one-dimensional magnets (e.g. $\text{PbNi}_2\text{V}_2\text{O}_8$), two-dimensional electron gases (e.g. $\text{ZnO}:\text{Zn}_{1-x}\text{Mg}_x\text{O}$), half-metals and colossal-magnetoresistive materials (e.g. $\text{Pr}_{1-x}\text{Ca}_x\text{MnO}_3$, $\text{La}_{0.7}\text{Sr}_{0.3}\text{MnO}_3$). Not only do complex oxides display a wealth of interesting physical properties, but also they hold great promise for technological applications. As the limits of silicon-based electronics approach, researchers are looking towards the complex oxides as the next generation of materials to work with [3]. Novel functionalities are required in

the field of spintronics where half-metals have been used to make spin-valves and CMR materials for magnetic tunnel junctions [4]. Multiferroic heterostructures have been tested as next-generation memory elements [5].

In this thesis I report an experimental investigation into two different complex oxide systems: $\text{Cu}_{1-x}\text{Zn}_x\text{O}$, a high-temperature induced multiferroic, and $\text{La}_{0.7}\text{Sr}_{0.3}\text{MnO}_3:\text{ZnO}$, a colossal magnetoresistance material. The key idea connecting these investigations is understanding how manipulating material properties affects the dynamic optical response. In $\text{Cu}_{1-x}\text{Zn}_x\text{O}$ I investigated the effect of alloying copper with zinc on the multiferroic state; in $\text{La}_{0.7}\text{Sr}_{0.3}\text{MnO}_3:\text{ZnO}$ the strain and grain boundaries imposed by adding a second phase of ZnO to the material affects the THz magnetoresistance properties significantly.

This chapter will introduce multiferroic materials in Sec. 1.1 and then in Sec. 1.2 survey the literature on electromagnons; coupled spin-charge excitations which form the key results of Chapters 4 and 5. The colossal magnetoresistance manganites are briefly introduced in Sec. 1.3 the end of this chapter, before an outline of the rest of the thesis in Sec. 1.4.

1.1 Multiferroic materials

A multiferroic crystal has two or more forms of ferroic ordering present in a single homogeneous phase. In the literature, multiferroic heterostructures such as stacked alternate layers of ferroelectric and ferromagnetic materials coupled by a secondary order parameter like strain are referred to as multiferroics too, as are exchange bias coupled layers [6].

The study of multiferroic materials and their properties is an exciting and challenging area of condensed matter physics that has seen rapid growth in re-

cent years. Magnetism was well known to the ancients through lodestones, and magnetic compasses were used by the Chinese for navigation in the 12th century. Ferroelectricity was discovered in the 1920s when Valasek observed a spontaneous electric polarisation in Rochelle salt, $\text{KNa}(\text{C}_4\text{H}_4\text{O}_6) \cdot 4\text{H}_2\text{O}$ [7]. Electricity and magnetism were combined into one discipline in the 19th century, culminating in Maxwell's equations. However, electric and magnetic ordering in solids remained separate fields, and for good reason. Electric phenomena are caused by the charge of the electron whilst permanent magnetic phenomena occur due to its spin. In the vast majority of materials these are independent and in general ferroelectricity and ferromagnetism do not occur in the same material. Two developments began to change this picture. First came an observation of the magneto-electric effect; that is the coupling of spontaneous magnetisation to an applied electric field or of spontaneous polarisation to an applied magnetic field. Second was the discovery of single crystal multiferroics where both ferromagnetism and ferroelectricity are present in a single homogeneous phase.

The magneto-electric effect was first proposed by Pierre Curie in 1894. Despite many attempts the effect was not theoretically predicted to occur in a specific compound until 1959 when Dzyaloshinskii did so for antiferromagnetic Cr_2O_3 [8]. This prediction was experimentally confirmed in the following year by Astrov [9]. In the years following this breakthrough many more compounds exhibiting the magneto-electric effect were discovered, with the total to date of a few hundred [10].

The first multiferroic material studied was nickel boracite, $\text{Ni}_3\text{B}_7\text{O}_{13}\text{I}$, in 1966 [11]. This is a ferroelectric ferromagnetic multiferroic meaning that both forms of ordering are present in the same phase. Weak magnetic and electrical ordering occur simultaneously around 60 K and a magnetic-field-induced reversal of the

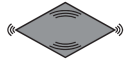
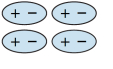

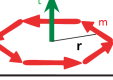
	Space	Invariant	Change
Time	Invariant	Ferroelastic 	Ferroelectric 
Change	Change	Ferromagnetic 	Ferrotoroidic 

Figure 1.1: All forms of ferroic order under the parity operations of space and time, as described in Section 1.1. Reproduced from Ref. [13].

magnetisation was found to flip the spontaneous polarisation $P_S = 0.076 \mu\text{Ccm}^{-2}$.

In 1994 Hans Schmid made a general classification of multiferroics based on symmetry considerations [12]. Using the 122 Shubnikov-Haas magnetic point groups he tabulated all possible forms of ferroic ordering permitted by each point group. Schmid first used the term multiferroic in this article and based on behaviour under space and time reversal symmetry he added two more forms of ferroic ordering to the classification: ferroelasticity and ferrotoroidicity.

Ferroelectrics

A ferroelectric material has a high temperature paraelectric phase and a low temperature ferroelectric phase. In the ferroelectric phase the system exhibits a stable electrical polarisation \mathbf{P} that can be switched hysteretically by application of an electric field \mathbf{E} ; see Fig. 1.2. Cooperative atomic displacements are responsible for the net polarisation in the low temperature phase. The phase transition is accompanied by a divergence in the static permittivity ϵ as shown in Fig. 1.3 [7; 14]. Ferroelectricity can only occur in a material with a non-centrosymmetric point group. Ferroelectrics can be classified as either ‘proper’ or ‘improper’. A proper ferroelectric is one where the polarisation is the primary order parameter for the phase transition and therefore determines the symmetry of the low

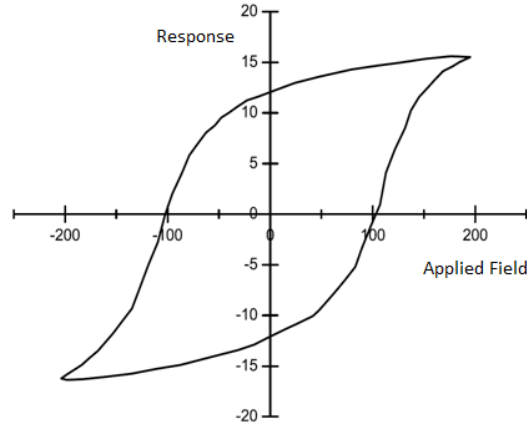


Figure 1.2: Schematic showing the response of a ferroic material to an applied field. The applied fields would be; \mathbf{E} , \mathbf{H} , σ , $\mathbf{E} \times \mathbf{H}$ and the responses; \mathbf{P} , \mathbf{M} , \mathbf{x} and \mathbf{t} for ferroelectrics, ferromagnets, ferroelastics and ferrotoroids respectively. Symbols are defined in the text in Section 1.1.

temperature phase, e.g. BaTiO_3 . However, other physical quantities may appear spontaneously below the transition. These secondary order parameters do not alter the symmetry of the phase but may display domains and critical anomalies at the transition. Examples include strain in BaTiO_3 and polarisation in the improper ferroelectric TbMnO_3 , where the primary order parameter is the magnetisation.

Ferromagnets

A ferromagnetic material has a high temperature paramagnetic phase and a low temperature ferromagnetic phase where spins are aligned. In the ferromagnetic phase the system exhibits a stable magnetisation \mathbf{M} that can be switched hysteretically by the application of an external magnetic field \mathbf{B} . Spin ordering is caused by the quantum mechanical phenomenon of exchange. Magnetism generally involves localised electrons, often in the partially filled d- or f- orbitals of transition metal or rare earth ions, except for itinerant ferromagnets like iron

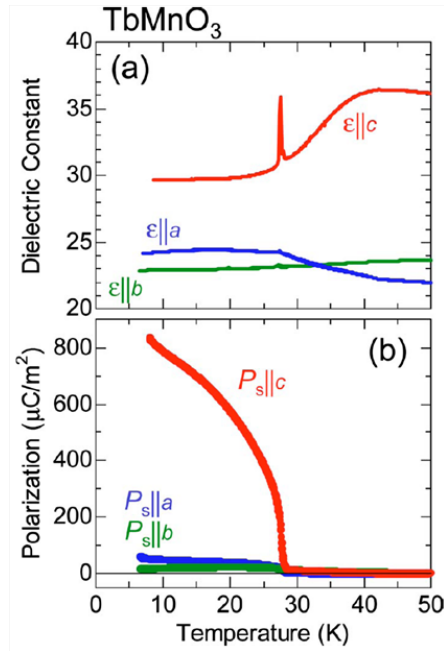


Figure 1.3: Experimental data showing how the polarisation and dielectric constant change with temperature in a ferroelectric material. Reproduced from Ref. [15].

which are not of interest here: as conductors they cannot be ferroelectric. A magnetic phase transition can be identified by a change in the behaviour of the magnetic susceptibility, χ [16].

It is important to be aware that in the literature on multiferroics, especially in some articles discussing symmetry, the term “ferromagnet” can be used to mean “a system with magnetic ordering” in a more general sense. That is, “ferromagnet” could denote a magnetically ordered material with antiferromagnetic, ferrimagnetic, helical or spin spiral symmetries.

Ferroelastics

Ferroelasticity is the mechanical analogue of ferroelectricity and ferromagnetism. A crystal is ferroelastic if it has two or more orientation states differing in spontaneous strain which can be switched by applying an external mechanical stress.

It is a type of mechanical twinning and does not involve diffusion or the breaking of chemical bonds; just small atomic displacements. Unlike the \mathbf{E} and \mathbf{P} in a ferroelectric and \mathbf{B} and \mathbf{M} in a ferromagnet, the stress σ_{ij} and strain x_{ij} are symmetric second rank tensors. The induced strain is measured relative to the unit cell parameters of the prototype (high temperature) phase [17].

Ferrotoroids

Recently, there has been a great effort to find evidence for a new ferroic order parameter. Using the ‘missing box’ argument (see Fig. 1.1) it was suggested that there must be a form of ferroic ordering that broke both space-inversion and time-reversal symmetries to complement the existing ferroic orders: ferroelastics are both space and time inversion symmetric, ferroelectrics are invariant under time reversal but not space inversion and ferromagnets are spatially symmetric but asymmetric under time reversal [18]. There is some disagreement in the literature about the correct form for the toroidal moment and the connection between the macroscopic symmetry of the toroidal component of the free energy and the microscopic origin of the term. Ederer and Spaldin [19] distinguish between the electric and magnetic toroidal moments, which have different symmetry properties, stating clearly that it is the magnetic toroidal moment $\mathbf{t} = \frac{1}{2} \sum_{\alpha} \mathbf{r}_{\alpha} \times \mathbf{m}_{\alpha}$ that breaks both space and time reversal symmetries, assuming a distribution of local magnetic moments, \mathbf{m}_{α} , at sites \mathbf{r}_{α} . They go on to calculate \mathbf{t} for four known multiferroics; BaNiF_4 , LiCoPO_4 , GaFeO_3 and BiFeO_3 . Van Aken *et al.* claim that optical second harmonic generation (SHG) spectroscopy has been used to image ferrotoroidal domains in LiCoPO_4 , however the authors do not demonstrate that the domains are switchable on application of crossed \mathbf{E} and \mathbf{H} fields, so this cannot be taken as conclusive evidence for true ferroic ordering [13]. In

September 2010, Ressouche *et al.* [20] claimed to observe ferrotoroidic domains in MnPS_3 that can be switched under application of crossed electric and magnetic fields, using neutron diffraction and polarimetry.

Finally it is worth mentioning that some authors suggest that the electric toroidal moment $\mathbf{g} = \frac{1}{2} \sum_{\alpha} \mathbf{r}_{\alpha} \times \mathbf{p}_{\alpha}$ would be a better candidate than the ferroelastic strain tensor x_{ij} for the time and space inversion symmetric ferroic order parameter, as it is a vector like all the others [19]. Here, \mathbf{p}_{α} are local electric dipole moments at positions \mathbf{r}_{α} . Of course this multiplicity of possible ferroic order parameters with the same symmetry raises the question of whether there are more second rank tensors that could be associated with other symmetry groups.

Multiferroics

This thesis will focus exclusively on ferroelectric ferromagnetic multiferroics; first classifying the materials by briefly describing some of the mechanisms for multiferroicity and then reviewing the literature on coupled excitations in Section 1.2. The different mechanisms causing multiferroicity are well covered by Khomskii [21] and references therein.

Type I multiferroics are materials that are independently ferroelectric and ferromagnetic, i.e. the two properties come from different sources. Generally these have high spontaneous polarisations ($\sim 10\text{-}100 \mu\text{Ccm}^{-2}$) and high ($\gtrsim 100\text{ K}$) ferroelectric and ferromagnetic transition temperatures. Often the magnetoelectric coupling is weak and the challenge is to enhance this coupling without compromising their other good properties. Fig. 1.4 illustrates four different microscopic mechanisms. In mixed perovskites with ferroelectrically active d^0 ions (green circles in Fig. 1.4(a)) and magnetic d^n ions (red), shifts of d^0 ions from the centres of O_6 octahedra (yellow squares) lead to polarisation (green arrows) coexisting

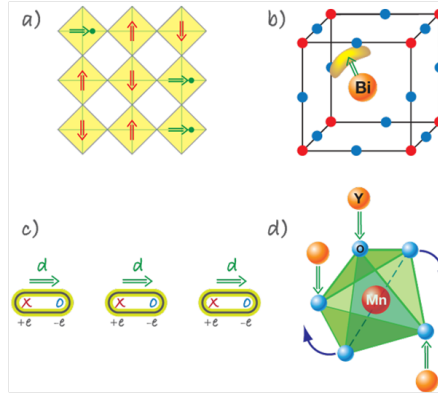


Figure 1.4: Different microscopic mechanisms found in type I multiferroics. Mixed perovskites (a), lone pair ordering (b), charge ordering (c), and a “geometric” mechanism (d). The mechanisms are explained with reference to the figures in Section 1.1. Reproduced from Ref. [21].

with magnetic order (red arrows). Fig. 1.4(b) shows how the ordering of 6s lone pairs (yellow lobes) of Bi^{3+} ions (orange) gives rise to a polarisation (green arrow) in BiFeO_3 . In charge ordered systems, the coexistence of sites with different charges and inequivalent (long and short) bonds leads to ferroelectricity as in Fig. 1.4(c). Finally, see Fig. 1.4(d) for the “geometric” mechanism of generation of polarisation in YMnO_3 . This describes the tilting of a rigid MnO_5 block with a magnetic Mn remaining at the centre. When rotated out of the plane the Y-O bonds form dipoles (green arrows), and two “down” dipoles form per one “up” dipole so that the system becomes ferroelectric (and hence multiferroic when Mn spins order at lower temperatures).

Type-II multiferroics are systems where ferroelectricity is caused by magnetic ordering and would not exist without it. Also called improper ferroelectric multiferroics as polarisation is not the primary order parameter for the multiferroic phase transition. These materials often have low transition temperatures (~ 10 K) and weak polarisations ($\sim 0.01 \mu\text{Ccm}^{-2}$). However the order parameters are generally very strongly coupled. Further subdividing the class, we have spiral magnets

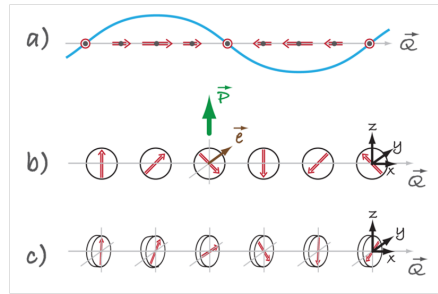


Figure 1.5: Spin structures relevant for type-II multiferroics. Sinusoidal spin density wave (a), cycloidal spiral where spins rotate in a plane containing the wavevector Q (b), and a so-called “proper screw” where the spins rotate in a plane perpendicular to Q (c). Reproduced from Ref. [21].

where the polarisation is caused by a Dzyaloshinskii-Moriya type interaction (see Chapter 2) such as TbMnO_3 , $\text{Ni}_3\text{V}_2\text{O}_6$ and MnWO_4 , as in Fig. 1.5(b). Collinear magnetic structures can also exhibit a spontaneous polarisation. A lattice commensurate sinusoidal spin density wave (see Fig. 1.5(a)) in which spins point along one direction but vary in magnitude is centrosymmetric and consequently not ferroelectric. However a polarisation can be induced by exchange striction as in $\text{CaMn}_7\text{O}_{12}$ [22].

Multiferroics: Applications

A desire to use the unique properties of multiferroics for technological applications has been a driving force behind the rapid development of the field. Abundant possibilities for multiferroics include photovoltaics [23], spin valves [24], sensors and actuators [25]. Perhaps the two most important areas of application are in novel solid state memories and spintronic devices.

A 4-state logic device ($\mathbf{P}\uparrow$, $\mathbf{P}\downarrow$, $\mathbf{M}\uparrow$, $\mathbf{M}\downarrow$) has been suggested along with a two state electronic-write magnetic-read memory to improve on ferroelectric memories currently used in some consumer electronic devices. A multiferroic heterostructure is already being tested for possible use in a commercial device

[5].

The electric-field tuning of electromagnons in DyMnO_3 , an improper ferroelectric multiferroic [26], and of magnons in bulk BiFeO_3 , a proper ferroelectric multiferroic [27], establish the potential of spin waves in data processing and communications [28].

Multiferroics: Reviews

Several reviews have been written over the last ten years focussing on different aspects of the field. Schmid [12; 29] is invaluable on the symmetry aspects of multiferroics; Fiebig [30] deals comprehensively with the magneto-electric effect; Hill (now Spaldin) [18] investigates the microscopic mechanisms through which multiferroic properties are manifested; Khomskii [21] introduces Type-I and Type-II multiferroics; Wang *et al.* provide a comprehensive historical overview including experimental data [10]; and finally Eerenstein, Mathur and Scott [6] provide a useful overview for the non-expert and clarify some confusing nomenclature.

1.2 Electromagnons

The coexistence of magnetic and ferroelectric ordering in the same material is accompanied by a fundamentally new set of coupled excitations: electromagnons. These are electric-dipole active magnons; that is, spin waves that can be excited by electric fields.

Electromagnons were first observed by Pimenov *et al.* as described by their much cited paper of January 2006 [32]. They performed THz transmittance experiments on samples (typically $5 \times 5 \times 1 \text{ mm}^3$) using a Mach-Zender interferometer. Measuring the transmittance and phase shift of the sample as functions

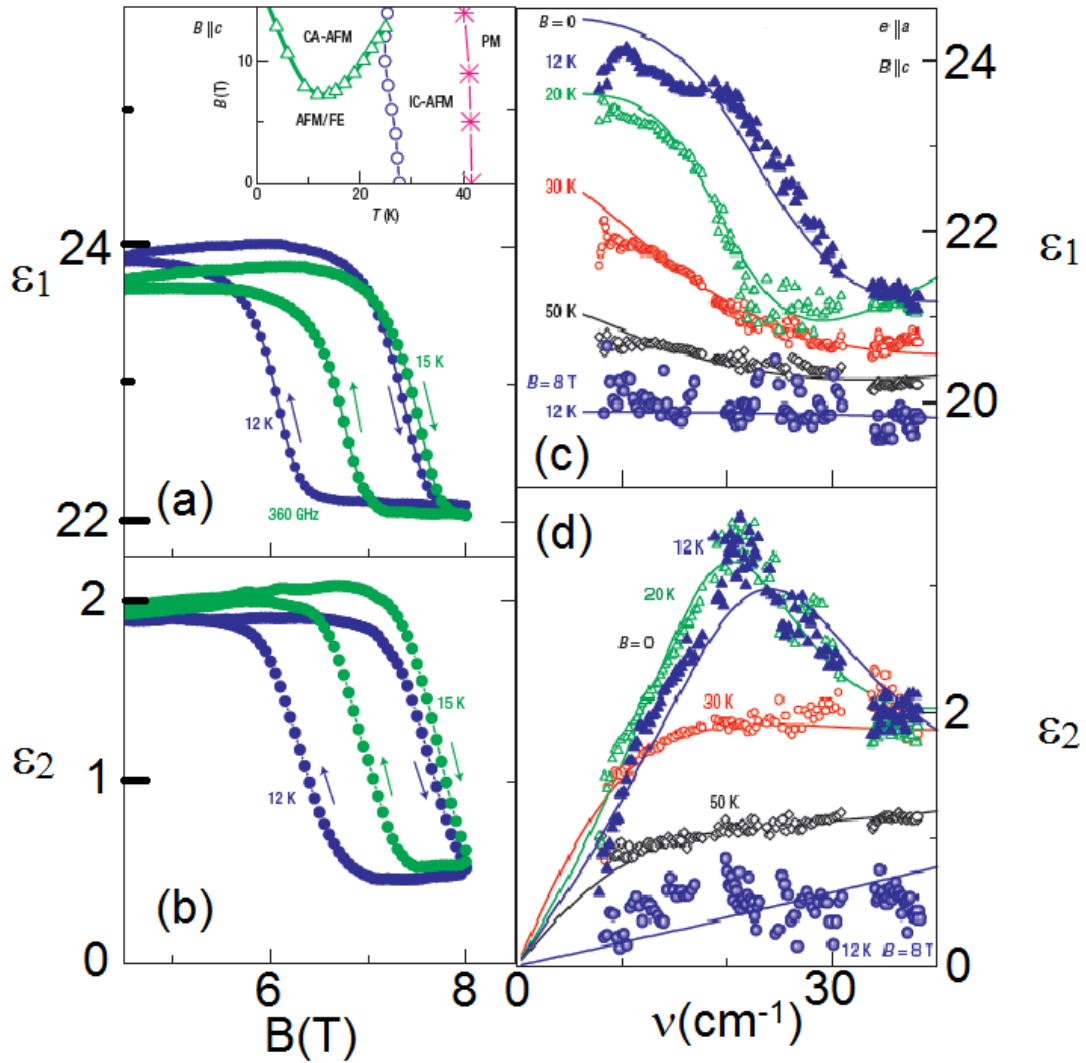


Figure 1.6: **First experimental evidence for an electromagnon** Changes in the real (a) and imaginary (b) parts of the permittivity at 360 GHz with applied magnetic field. Frequency-dependent dielectric response of TbMnO₃ at various temperatures and magnetic fields. Panel (c) shows the real part and panel (d) shows the imaginary part. Reproduced from Ref. [31].

of frequency (0.1–1.2 THz), temperature (1.8–300 K) and magnetic field (0–7 T), their two main results were as follows:

1. A step like increase in the permittivity was observed on switching between the two low temperature magnetic phases of perovskite manganites GdMnO_3 and TbMnO_3 , indicating that there is a strong coupling between the magnetic and electric order. See Fig. 1.6 (a-b).
2. A peak in the imaginary part of the permittivity exists in the low temperature phase of the material, which broadens with increasing temperature and disappears on magnetically switching to the paraelectric spin-canted antiferromagnetic phase. This peak was identified as an electric dipole active resonance by determining the selection rules from three samples, each one oriented along a different crystal axis. See Fig. 1.6 (c-d).

Later in the year, Pimenov *et al.* extended their study of GdMnO_3 into the infrared up to 21.2 THz (700 cm^{-1}) to probe the IR active phonons. They concluded that at the transition to a paraelectric phase the spectral weight of electromagnons is transferred to an optical phonon, which in addition reveals a slight softening of the eigenfrequency [31].

This pair of papers stimulated much activity, and with good reason. The authors had identified an excitation long sought after and fundamentally new to condensed matter physics. There was tantalising evidence that this excitation was indeed an electric dipole active magnon; however, the story was far from complete. There was some ambiguity as to whether this peak in the dielectric function was not in fact caused by f-f shell electronic transitions, a complete set of polarisation measurements were not presented and the authors extracted the complex electric permittivity from the transmission spectra, via the Fresnel

optical equations, by assuming that the complex magnetic permeability $\mu = 1$, something far from obvious in these magnetically ordered materials.

An ideal test system: TbMnO₃

TbMnO₃ is an ideal test system for investigating the origins and dynamics of the electromagnon, as shown by the more than twenty papers published related to electromagnons in this compound since 2006. Investigations using THz, infrared (IR) and Raman spectroscopies; elastic and inelastic neutron scattering and theoretical studies have been made. Here we review the most important of these in order to build a complete picture of our knowledge of electromagnons to date, adding experimental details only for the THz and IR studies.

The magnetoelectric phase diagram of TbMnO₃ was determined by a comprehensive set of measurements in 2005 by Kimura *et al.* as shown by Fig. 1.7 [33]. This well studied system has a distorted perovskite structure (orthorhombic, space group *Pbnm*) and the Mn³⁺ ion is the only magnetic species present. This greatly simplifies the considerations compared to systems where two or more magnetic species are present such as *RMn₂O₅*, which contains both Mn²⁺ and Mn³⁺ ions.

Inelastic Neutron Scattering The magnetic field dependence of elastic and inelastic neutron scattering in TbMnO₃ was investigated by Senff [34; 35]. It was found that the magnetic superstructure reflections exhibit strong hysteresis across the magnetic transition that accompanies the flop of the electronic polarisation (see Fig. 1.7) and there is a clear magnetic memory effect. The authors state that this is a generic feature at incommensurate to commensurate spin flop transitions in spiral magnets (see Fig. 1.8). Their results are consistent with the

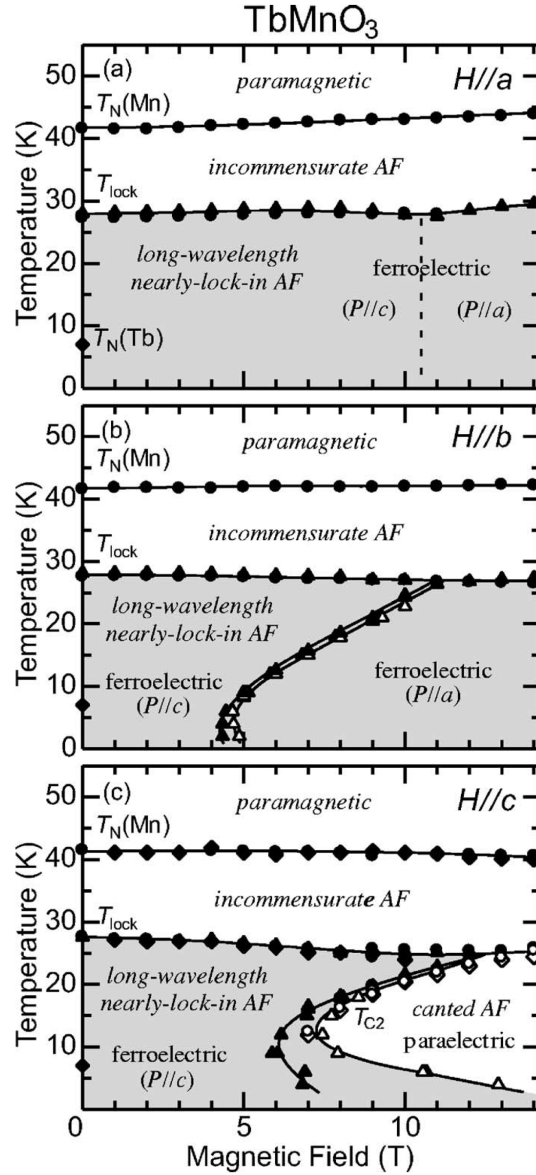


Figure 1.7: Magneto-electric phase diagram of TbMnO₃ with magnetic fields along the (a) a, (b) b, and (c) c axes. Circles, triangles, and diamonds represent the data obtained by measurements of the dielectric constant, pyroelectric (or magneto-electric) current, and magnetization respectively. Open and closed symbols denote the data obtained with decreasing temperature (or increasing magnetic field) and increasing temperature (or decreasing magnetic field), respectively. Grey regions indicate ferroelectric phases. Reproduced from [33].

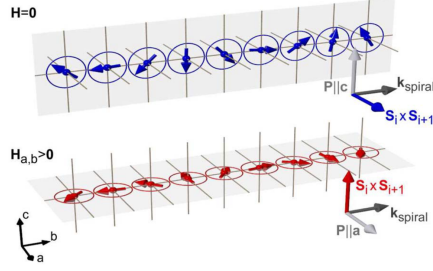


Figure 1.8: Top: Sketch of the magnetic spiral structure in zero field inducing an electric polarisation \mathbf{P} . Bottom: The rotation from \mathbf{P}_c to \mathbf{P}_a in the high-field phase is supposed to originate from a concomitant flop of the spiral rotation axis from a to c . Reproduced from Ref. [34].

assumed field-induced flop of the spiral plane from the bc to ab planes, which explains the giant magnetoelectric effect that arises from the rotation of the electric polarisation from \mathbf{P}_c to \mathbf{P}_a .

Good agreement between the frequencies of the two a -polarised zone-center modes in the cycloidal phase at $T = 17\text{K}$ in inelastic neutron scattering experiments with those obtained in the a -polarised THz response strongly suggests the identification of the THz signal as a magnon. Since the chosen polarisations in the THz experiment [32] would not allow the detection of the magnetically a -polarised mode via the magnetic field, the magnon must couple in the charge channel indicating its hybridized electromagnon character. The strong electromagnon response is always found along the a -axis independently of the orientations of cycloid and polarisation, inconsistent with it being an electro-active eigenmode of the spin cycloid.

THz, IR and Raman spectroscopy Kida *et al.* [36] performed a transmission-THz-TDS study on TbMnO_3 and $\text{Gd}_{0.7}\text{Tb}_{0.3}\text{MnO}_3$, the latter of which has a similar phase diagram to the former but does not undergo a polarisation flop under application of a magnetic field ($B \leq 14\text{T}$). In the low tem-

perature, low magnetic field region of the phase diagram the system exhibits an A-type AFM phase where both ferroelectricity and electromagnons disappear.

The first complete set of light-polarisation measurements, shown in Fig. 1.9, were performed on $\text{Gd}_{0.7}\text{Tb}_{0.3}\text{MnO}_3$. A broad continuum-like spin excitation (1–10 meV) with a peak structure around 2.4 meV was observed in the ferroelectric *ab* spiral spin phase. The spin excitation is electro-active only when \mathbf{E}_ω lies along the *a*-axis. It grows in intensity on cooling into the spin cycloid phase, but disappears upon the transition to the low temperature A-type AFM phase. In the A-type AFM phase there is a magnon active for $\mathbf{H}_\omega \parallel a$ or $\mathbf{H}_\omega \parallel c$. These measurements set the standard for optical investigations of electromagnons.

Aguilar *et al.* extended the investigation of TbMnO_3 into the infrared using a Fourier transform spectrometer (15–100 cm^{-1}) and identified the high field *a*-axis peak as a pure magnon [37]. This was the first paper to introduce a theoretical model for electromagnons in the $R\text{MnO}_3$ (R =rare earth) compounds, discussed further in Chapter 2. Here, the first hints are given that the static and dynamic properties of the system are governed by different interactions. Pimenov and co-workers revisited TbMnO_3 in March 2009 [38] with a Mach-Zender interferometry study that confirmed the ideas of Aguilar *et al.* who were able to separate electromagnons from magnons. The frequencies of two magnon modes coincide with the electromagnon frequencies indicating that both excitations correspond to the same eigenmode of the magnetic cycloid. Once more, no electromagnon contribution was detected along the *c* axis on a *B*-field induced rotation of the magnetic cycloid from *bc* to *ab* plane. This excludes any explanation of electromagnons based on the magnetic cycloid.

Raman studies revealed two magnetic excitations at 30 cm^{-1} and 60 cm^{-1} with light polarisation $E_\omega \parallel a$ [39]. In contrast to THz experiments, the Raman data

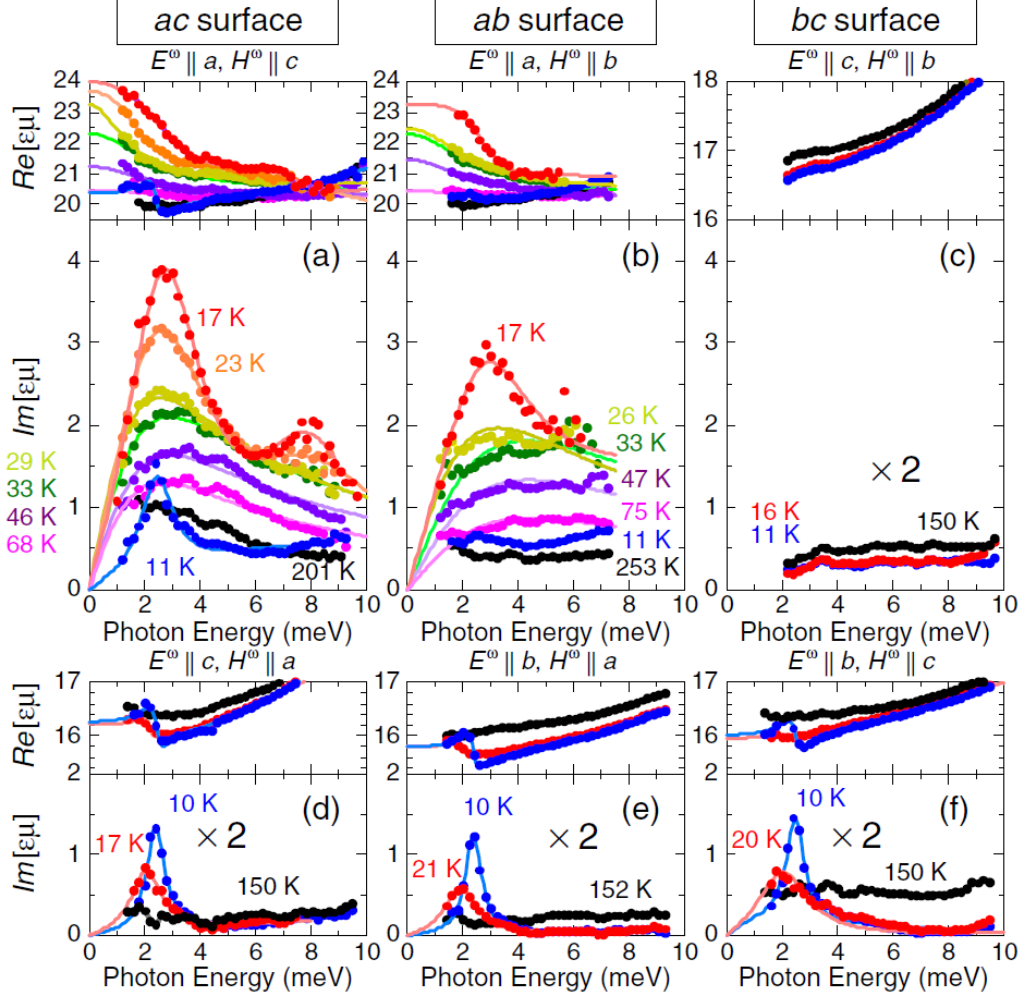


Figure 1.9: Temperature variations of the low-energy electrodynamic properties of $\text{Gd}_{0.7}\text{Tb}_{0.3}\text{MnO}_3$ in a variety of thermally induced phases. Upper and lower panels show the real and imaginary parts of $\epsilon\mu$ spectra (closed circles) when E_ω and H_ω were set parallel to the crystallographic axes of ac -, ab -, and bc -surface crystal planes. For the case of $E_\omega \parallel a$, the $\epsilon\mu$ spectra in the paraelectric collinear spin phase can be fitted with a Debye relaxation model, and those in the ferroelectric ab spiral spin phase with two Lorentz oscillators for ϵ , as shown by solid lines. In the A-type antiferromagnetic phase, the μ component becomes active and the $\epsilon\mu$ spectrum can be fitted with two Lorentz oscillators for ϵ and μ (solid lines). Reproduced from Ref. [36].

show that the 30 cm^{-1} mode (close in energy to the IR active mode at 24 cm^{-1}) is enhanced by light polarised such that $E_\omega \parallel P \parallel c$. Both modes are only present in the cycloidal phase, underlying their unusual magnetic character. The mode at 60 cm^{-1} is interpreted as the zone-edge magnon-phonon hybridization with the phonon part describing the electric polarisation parallel to a .

Fourier-transform infrared spectroscopy (FTIR) was used to assign all phonons for $E_\omega \parallel a$ and $E_\omega \parallel c$ to the modes predicted by group theory. Most phonon modes revealed anomalies in their eigenfrequencies or damping constants close to phase transitions, indicating magnetoelectric coupling effects. A transfer of the spectral weight between phonons with $E_\omega \parallel a$ and electromagnons was reported, resulting in a decrease in permittivity of ~ 0.5 just below the phonon frequencies [40].

Theoretical studies In the low temperature ferroelectric phase of TbMnO_3 the spins order in an incommensurate cycloidal spiral state. The microscopic origin of ferroelectricity for this case relies on lowering the energy of the anti-symmetric Dzyaloshinskii-Moriya (DM) exchange in the spiral state by a polar lattice distortion. This induces an electric polarisation $\mathbf{P} \propto \mathbf{Q} \times (\mathbf{S}_i \times \mathbf{S}_{i+1})$, where the cross product of nearest neighbour spins, $\mathbf{S}_i \times \mathbf{S}_{i+1}$, gives the spin rotation axis and \mathbf{Q} is the wave vector of the spiral. Naturally, the starting point for a theory of the dynamics of a system where spin ordering is governed by a DM exchange interaction would be an excitation also governed by this interaction, involving an eigenmode of the spin cycloid, as investigated by Katsura *et al.* [41] in 2007. However, this theory requires that the following selection rules are obeyed: $\mathbf{P} \parallel a$ is excited by $E_\omega \parallel a$ only while $\mathbf{P} \parallel c$ is excited by $E_\omega \parallel c$ only. Experimentally this is not observed. In fact the electromagnon is excited only by $E_\omega \parallel a$ regard-

less of the orientation of the static polarisation as discussed above and in Refs. [15; 31; 32; 36–38; 42].

Various theories have been proposed to explain these selection rules; including a spin current model, two-magnon processes, coupling to optical phonons and a Heisenberg exchange process, as discussed in the following paragraphs. The observed selection rule clearly indicates that any theory must take account of the specific characteristics of these manganites, such as the crystal structure and anisotropic magnetic interactions, in order to find an accurate description of the electromagnon excitations. Aguilar *et al.* suggested that electromagnon excitations in multiferroic orthorhombic $RMnO_3$ result from Heisenberg coupling between spins despite the fact that the static polarisation arises from the much weaker Dzyaloshinskii-Moriya exchange interaction. Using the Hamiltonian $\mathcal{H} = \frac{1}{2} \sum_{i,j} \mathbf{J}_{ij} \cdot \mathbf{S}_i \cdot \mathbf{S}_j$ the qualitative behaviour of the system can be replicated [37].

Mochizuki, Furukawa and Nagaosa used a five term Hamiltonian to reproduce the electromagnon spectrum of $TbMnO_3$ in a Monte-Carlo simulation. First they showed that the experimentally observed polarisation can be well modelled as a sum of symmetric (Heisenberg) and anti-symmetric (DM) polarisations [43]. Furthermore, they successfully reproduce the electromagnon spectrum for $TbMnO_3$ and other rare earth manganites, including energies and wavevectors. The model reproduces the THz data but the wavevectors are not known for all systems to which the theory applies; neutron scattering experiments may further test the model's validity.

The Heisenberg and DM models for electromagnons are discussed in detail in Chapter 2. Selection rules, optical sum rules and changes in the static permittivity and permeabilities all provide information needed to understand the mechanisms behind electromagnons and validate theoretical models.

Changing ionic radius Experiments involving systematic chemical substitution to investigate the effect of ionic radius on the nature of the magnetoelectric phase diagram and associated excitations have been important in producing a theory of electromagnons. Two THz and one FTIR studies of the compound $\text{Eu}_{1-x}\text{Y}_x\text{MnO}_3$ for $0 \leq x \leq 0.5$ have been made [40; 44; 45]. These experiments support selection rules discovered for TbMnO_3 and provide strong evidence for a transfer of the spectral weight between electromagnons and phonons.

The Tokyo group [46] have made two excellent THz and FTIR studies along these lines. Using a series of samples (Gd, Tb, Dy and alloys thereof) of the multiferroic perovskite manganites RMnO_3 . Fig. 1.10 shows beautifully how the peak structure changes with ionic radius. Using a Heisenberg exchange model they reproduced their results, which allowed them to deduce that the strength of the spin-exchange interaction energy is directly proportional to the R -ion radius [46]. In a second study, they produce a phase diagram (reproduced in Fig. 1.11) showing how the magnetic structure changes with ionic radius of the R -ion for the system $\text{Eu}_{1-x}\text{Y}_x\text{MnO}_3$ for $0.1 \leq x \leq 1$ and $\text{Y}_{1-y}\text{Lu}_y\text{MnO}_3$ for $0 \leq y \leq 1$ [47].

Electromagnons in other materials Whilst the main focus of research into electromagnons has been on the perovskite manganites, other materials have been investigated. Some of the early papers were on hexagonal manganites, RMnO_3 ($R=\text{Y}, \text{Eu}$). Selection rules for electric dipole active resonances were determined (again tied to the lattice), the optical conductivity was measured, and the electromagnon was found to be responsible for a step change in the dielectric constant [48]. Theoretical studies have been made which suggested that these were Heisenberg exchange electromagnons. However the form of the theory is different from the RMnO_3 materials and highlighting how important the local atomic environ-

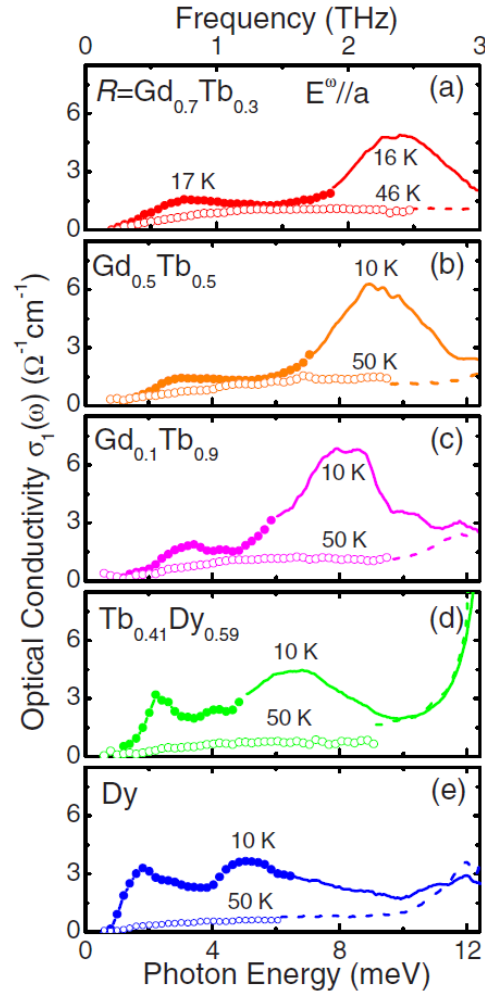


Figure 1.10: The optical conductivity spectra $\sigma_1(\omega)$ of $RMnO_3$ in the spiral spin (ferroelectric) state and the paramagnetic/ paraelectric state for (a) $R=\text{Gd}_{0.7}\text{Tb}_{0.3}$, (b) $\text{Gd}_{0.5}\text{Tb}_{0.5}$, (c) $\text{Gd}_{0.1}\text{Tb}_{0.9}$, (d) $\text{Tb}_{0.41}\text{Dy}_{0.59}$, and (e) Dy . In each curve, the symbols correspond to the results obtained by THz time-domain spectroscopy and the solid and dashed lines by Fourier-transform spectroscopy. Reproduced from Ref. [46].

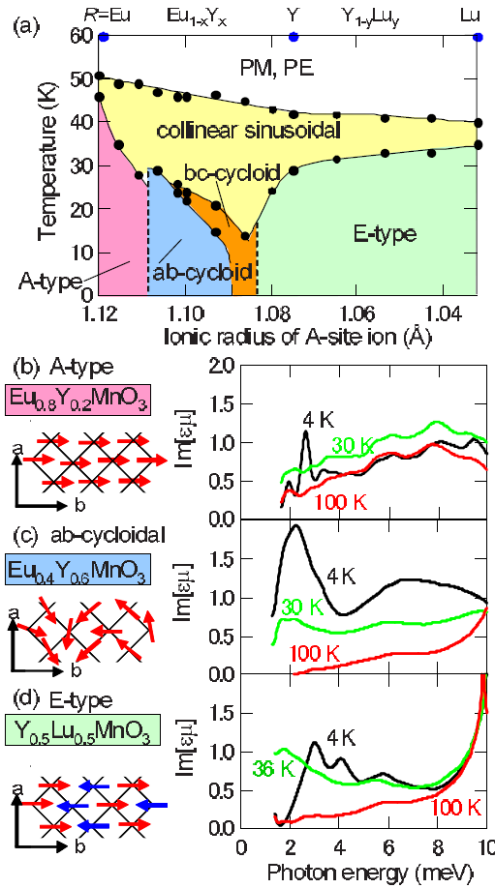


Figure 1.11: (a) The phase diagram of $\text{Eu}_{1-x}\text{Y}_x\text{MnO}_3$ for $0.1 \leq x \leq 1$ and $\text{Y}_{1-y}\text{Lu}_y\text{MnO}_3$ for $0 \leq y \leq 1$. The $\text{Im}[\epsilon\mu]$ spectra for (b) A-type, (c) *ab*-cycloidal, and (d) E-type spin phase with the schematic spin structures. Reproduced from Ref. [47].

ment is in producing any model for these excitations [49; 50].

The complex THz absorption spectrum of multiferroic LiCu_2O_2 presented “tantalising evidence” for electromagnons [51], modelled using a Heisenberg model with a single-ion anisotropy term [52].

Electromagnons were identified in the conical spin phase of $\text{Ba}_2\text{Mg}_2\text{Fe}_{12}\text{O}_{22}$ in a study using THz-TDS and inelastic neutron scattering. Giant thermochromism and magnetochromism led the authors to suggest a future device application in a tunable THz colour filter controlled by \mathbf{H} [53].

THz-TDS has experimentally revealed an electromagnon excitation in the paraelectric ($\uparrow\uparrow\downarrow\downarrow$) collinear magnetic phase of triangular lattice antiferromagnet $\text{CuFe}_{1-x}\text{Ga}_x\text{O}_2$. This mode was found to vanish in the ferroelectric helimagnetic phase. The paper suggests that neither ferroelectricity nor noncollinear magnetism is a necessary condition for the appearance of electromagnon excitation, despite the current focus on such systems. The anticorrelation between the noncollinear magnetism and the emergence of electromagnons in $\text{CuFe}_{1-x}\text{Ga}_x\text{O}_2$ excludes the exchange-striction mechanism as the origin of dynamic magnetoelectric coupling. The electric activity of the magnon in this compound is ascribed to the modulation of the p-d hybridisation at the spin-twisted excited state via the spin-orbit interaction. Their discovery suggests that similar electromagnon modes may be observable in a wide range of paraelectric collinear magnets [54].

Finally, the results in this thesis present compelling evidence for an electromagnon in the high temperature induced multiferroic CuO , as detailed in Chapters 4 and 5.

Summary

In the eight years since 2006 when electromagnons were first observed by Pimenov *et al.* much progress has been made towards understanding these novel quasi-particles. The excitations are well characterised, with intensities, energies and selection rules extensively studied for a handful of materials, most notably the rare-earth manganites and various hexaferrites. Electromagnons have been described theoretically in some compounds, with the focus on $RMnO_3$ compounds and various microscopic models are covered in detail in Chapter 2. From the experiments made so far, some useful lessons can be drawn. Firstly, THz time domain spectroscopy is essential for a full characterisation and all of the best studies have separated the contributions from the complex electric permittivity and magnetic permeability tensors. Next, a complementary second probe is very useful for definitively assigning resonances, either inelastic neutron or Raman spectroscopy. Extending experiments into the infrared is desirable in order to determine if phonon modes mix with the electromagnon, which can give vital clues as to the microscopic mechanisms at work. There have been tantalising hints that electromagnons may not be restricted to multiferroics.

Electromagnons: Applications

Electromagnons may permit novel THz optical components, such as chromatic filters, waveplates, or directionally dichroic filters [55]. Room temperature, tunable electromagnons (under readily accessible electric or magnetic fields) are therefore strongly desired. Time resolved X-ray diffraction has shown that intense THz pulses coupled to an electromagnon resonance can alter the magnetic order in $TbMnO_3$, raising the possibility of THz magnetic switches [56].

Electromagnons: Reviews

A number of reviews have been written on electromagnons. The first collection of material related to this topic was in a special issue of the Journal of Physics: Condensed Matter (vol. 20, issue 43) in 2008. This is an excellent starting point to get an overview of research in multiferroics at the time, including the first review specifically on electromagnons by Pimenov *et al.* [42]. The following year Kida *et al.* published a comprehensive review of THz-spectroscopy of electromagnons in multiferroic manganites [15]. Later, in 2012, another short review by Kida focussed on the exchange striction model of electromagnons [57] and Krivoruchko reviewed the theoretical modelling of electromagnons in various types of magnetic system [58], in addition to re-introducing the earliest theoretical work on electromagnons from Russia in the 1960's.

1.3 Manganites and the colossal magnetoresistance effect

Manganite compounds have been of great interest to condensed matter physicists since a paper by Jonker and van Santen was published in 1950 [59], describing the synthesis and magnetic characterisation of a range of such materials. Sixty-four years later, in May 2014, nearly 10,000 papers have been published on the topic [60]. This section presents a brief and general introduction to the physics of manganite compounds exhibiting colossal magnetoresistance by way of some key experimental results. Then, in some more detail, I will describe the particular compound $\text{La}_{0.7}\text{Sr}_{0.3}\text{MnO}_3$ which forms the basis for the study in Chapter 6.

Jonker and van Santen prepared a series of polycrystalline samples of

$R_{1-x}A_x\text{MnO}_3$ (R =rare earth ion, in this case La, and A =alkaline earth, in this case Ca, Ba, and Sr) across the full range of concentrations. The compounds that crystallised in perovskite structures were found to be ferromagnetic. The saturation magnetisation and Curie temperatures varied strongly with composition, which the authors discussed in terms of the valency of the manganese ions. Already it was clear that the manganites had a rich and complicated phase diagram. In a subsequent paper, the same authors measured the resistivity as a function of temperature and found anomalies at the Curie temperature across the range of compositions [61]. This marked out the manganites as being of a different nature to well known ferromagnetic metals such as Fe, Co, Ni and Gd which are metallic at all temperatures below their melting points. Indeed at some compositions there was clear evidence for a metal-insulator transition at the Curie temperature. A comprehensive study of the transport properties across the composition series $\text{La}_{1-x}\text{Sr}_x\text{MnO}_3$ was published by another researcher in the same laboratory in 1954 [62]. In addition to the magnetisation and resistivity; specific heat, Hall effect, Seebeck effect and magnetoresistance measurements were made. Notably, there was negative magnetoresistance below T_C proportional to the magnetisation, except for at a strong peak at the ordering temperature, with for example $-\Delta R/R = 10\%$ for $B = 3.75$ T in $\text{La}_{0.8}\text{Sr}_{0.2}\text{MnO}_3$. The first major neutron diffraction study on the manganites soon followed: magnetic structures were determined for the series $\text{La}_{1-x}\text{Ca}_x\text{MnO}_3$ [63]. An interesting phase diagram emerged showing a progression from A-type antiferromagnetic order in pure LaMnO_3 , through a mixed phase range with both FM and AFM regions for $0 < x < 0.25$, unbroken FM order for $0.25 < x < 0.5$, a complex C-E AFM phase with enlarged magnetic unit cell for $0.5 < x < 0.8$, and finally G-type AFM order for pure CaMnO_3 . The results are discussed in terms of the majority valency of

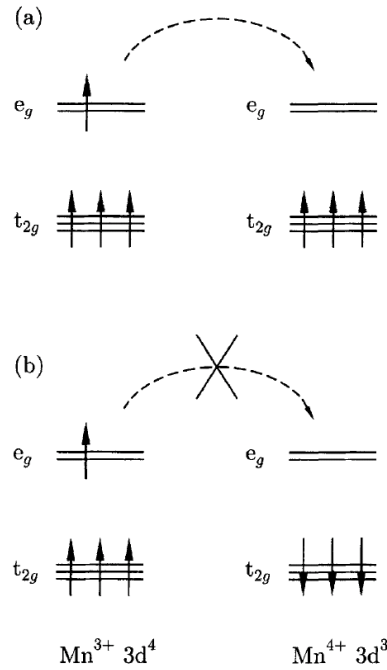


Figure 1.12: **Double exchange mechanism** Electrons save energy by hopping from Mn^{3+} to Mn^{4+} sites if neighbouring ions are ferromagnetically aligned (a) but not if they are antiferromagnetically aligned (b). Figure reproduced from [16].

the Mn ions changing from trivalent through to tetravalent as x varies from 0–1.

Shortly after the synthesis and measurement of the first manganite compounds to be studied as such, Zener published a theory explaining the ferromagnetic ordering for certain compositions [64]. Whilst the dominant interaction in the end-members of the series (RMnO_3 and AMnO_3) is superexchange leading to antiferromagnetic order, the situation is quite different for the mixed valence Mn ions in the intermediate doping regions. For octahedrally coordinated Mn ions the 3d energy levels are split into doubly degenerate e_g and triply degenerate t_{2g} energy levels, as shown in Fig. 1.12. Following Hund's rules, Mn^{4+} has three spin-parallel electrons in the low energy t_{2g} levels and Mn^{3+} has an extra electron also spin-aligned in the higher energy e_g level. If the t_{2g} Mn spins are ferromagnetically aligned, the system can save kinetic energy by allowing electron

hopping or delocalisation between sites. This double exchange mechanism formed the basis on which to understand the magnetic ordering in the manganites and despite our current knowledge that there is more complicated physics at work it remains a very useful simple model within which to think about these materials. In fact, carriers interact with phonons due to the Jahn-Teller effect causing the formation of polarons. Above the magnetic ordering temperature these magnetic polarons are self-trapped in the lattice; when spins order below T_C the polarons are unbound [16]. Work on the manganite compounds continued in the following decades with a large expansion in the materials studied finding even more types of ordering including charge, spin and orbitally ordered materials.

Enthusiasm for the manganites exploded in the 1990s after a paper was published in Science reporting a magnetoresistance of $-\Delta R/R_0 = 99.992\%$ (alternatively $-\Delta R/R_H = 127,000\%$) under a 6 T applied magnetic field at 77 K in thin films of $\text{La}_{0.67}\text{Ca}_{0.33}\text{MnO}_3$ [65]. Even at room temperature the effect was still large: $-\Delta R/R_0 = 93.3\%$ (alternatively $-\Delta R/R_H = 1400\%$) under $B=6$ T. This colossal magnetoresistance cannot be explained within the basic double exchange model where applying a magnetic field increases spin alignment, probability of hopping between sites, and therefore the conductivity. Consideration of polarons and the Jahn-Teller lattice distortion, nanoscale phase separation, and charge ordering in the high temperature phase have all been used to discuss this effect. These theories are beyond the scope of this thesis and will be referred to in the collection of reviews on the subject that follows in Section 1.3.1.

1.3.1 $\text{La}_{0.7}\text{Sr}_{0.3}\text{MnO}_3$

In this section I will focus on $\text{La}_{0.7}\text{Sr}_{0.3}\text{MnO}_3$ to introduce its properties in preparation for Chapter 6. Urushibara *et al.* made a comprehensive analysis of the

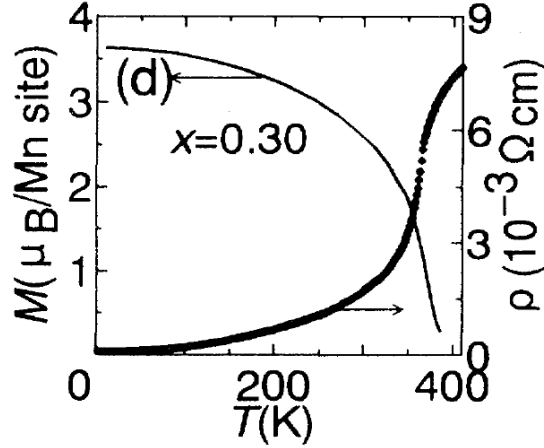


Figure 1.13: Magnetisation and resistivity of $\text{La}_{0.7}\text{Sr}_{0.3}\text{MnO}_3$ Data taken at $B = 0.5$ T. Figure reproduced from [66].

$\text{La}_{1-x}\text{Sr}_x\text{MnO}_3$ series in 1995 [66]. This study emphasised the importance of good quality single crystal samples in order to separate the intrinsic material properties from effects due to inconsistent oxygen content and grain boundary effects in polycrystalline materials. $\text{La}_{0.7}\text{Sr}_{0.3}\text{MnO}_3$ was found to crystallise in a rhombohedral unit cell, space group $R\bar{3}c$, with $a = 5.55 \text{ \AA}$ and $\alpha = 60.3^\circ$. Magnetisation and resistivity are shown in Fig. 1.13 from which the Curie temperature, $T_C = 369 \text{ K}$, and saturation magnetisation, $M_S = 3.5 \mu_B/\text{Mn site}$, are extracted. The resistivity follows a quadratic temperature dependence below 200 K indicating that electron-electron scattering is important in charge transport and thus the strongly correlated nature of the system. A phase diagram of the $\text{La}_{1-x}\text{Sr}_x\text{MnO}_3$ series (Fig. 1.14) shows that $\text{La}_{0.7}\text{Sr}_{0.3}\text{MnO}_3$ is on the cusp of a paramagnetic insulator to paramagnetic metal transition in the high temperature phase.

Practical applications require CMR at room temperature under low magnetic fields ($B < 1 \text{ T}$). $\text{La}_{0.7}\text{Sr}_{0.3}\text{MnO}_3$ is a good candidate given its high T_C . Pulsed laser deposition (PLD) of thin films offers the possibility of controlling the magnetoresistance of manganites through film thickness, epitaxial strain, and the

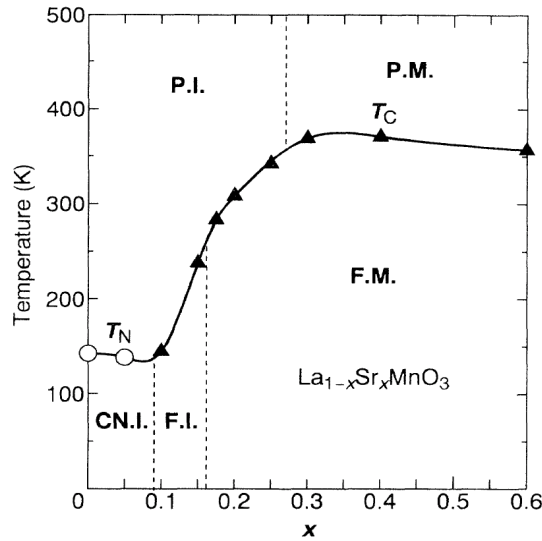


Figure 1.14: **Phase diagram of $\text{La}_{1-x}\text{Sr}_x\text{MnO}_3$** Open circles and filled triangles are Néel (T_N) and Curie (T_C) temperatures, respectively. The electronic phases are labelled: paramagnetic insulator (PI), paramagnetic metal (PI), spin-canted insulator (CNI), ferromagnetic insulator (FI), and ferromagnetic metal (FM). Figure reproduced from [66].

introduction of grain boundaries in an ordered manner. Epitaxial strain has been shown to control the resistivity by orders of magnitude and the Curie temperature by ~ 100 K in manganite thin films [67]. Careful manipulation of these parameters could lead to exciting device applications. Vertically-strained self-assembled nanocolumn thin films are particularly promising as vertical strain should be uniform throughout the sample, unlike horizontal strain due to substrate-film lattice mismatch which relaxes with distance away from the substrate interface. Fig. 1.15 shows the impressive control of magnetoresistance gained by altering the laser deposition frequency in PLD grown LSMO:ZnO on SrTiO_3 which, in turn, affects the width of nanocolumns [68].

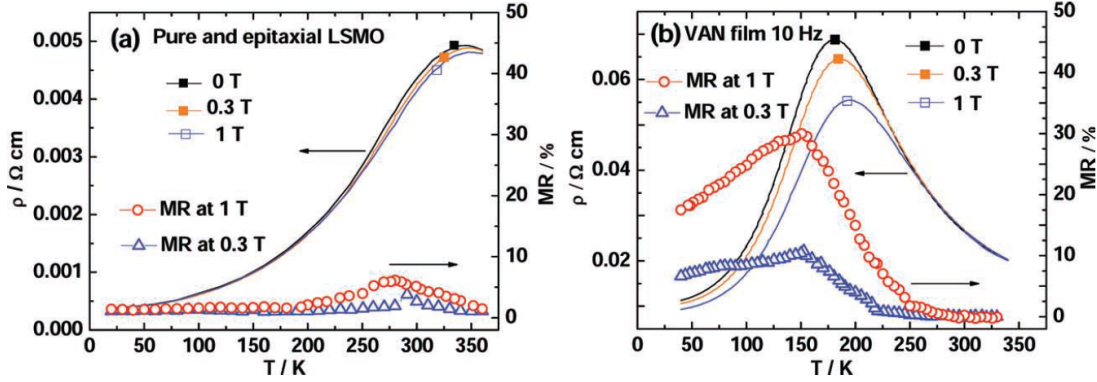


Figure 1.15: **Temperature dependence of resistivity and magnetoresistance** (a) Pure epitaxial $\text{La}_{0.7}\text{Sr}_{0.3}\text{MnO}_3$ film on SrTiO_3 substrate. (b) Vertically aligned nanocolumn $\text{La}_{0.7}\text{Sr}_{0.3}\text{MnO}_3:\text{ZnO}$ film deposited at 10 Hz. Figure reproduced from [68].

CMR manganites: Applications

Devices based on $\text{La}_{0.7}\text{Sr}_{0.3}\text{MnO}_3$ have been made for various spintronics applications [4], including magnetic tunnel junctions which utilise its half-metal property to integrate it into existing spintronic devices [69]. Spin polarised transport in carbon nanotubes has been demonstrated using $\text{La}_{0.7}\text{Sr}_{0.3}\text{MnO}_3$ as electrodes [70]. A giant magneto-caloric effect has been observed in $\text{La}_{0.7}\text{Sr}_{0.3}\text{MnO}_3$ under epitaxial strain prompting investigation of the possibility for ‘environmentally friendly energy efficient refrigeration’ [71].

CMR manganites: Reviews

Below is a select list of review articles on the manganites. Dagotto [72] (2002) comprehensively surveys the physics of manganites including experimental data, with a focus on the role of nanoscale phase separation; Tokura [73] (2006) updates this work; Edwards [74] (2002) focusses on theoretical models, especially the Holstein-double-exchange model which treats polarons outside of the small polaron regime; Basov *et al.* [75] (2011) introduce optical experiments on the

manganites and Bibes and Barthélémy [4] (2007) discuss the role of manganites in oxide spintronics.

1.4 Structure of this thesis

This thesis on the magneto-optics of complex oxides at terahertz frequencies draws together a series of experimental studies of magneto-electric materials. They are all linked by an attempt to control the magneto-electric coupling through materials design: specifically to manipulate the temperature range of the multiferroic phase in CuO by doping, and by imposing strain on $\text{La}_{0.7}\text{Sr}_{0.3}\text{MnO}_3$ via growth of thin films with vertical nanocolumns of a spacer material in order to enhance their magneto-resistance. Both of these techniques alter the unit cell parameters of the original materials and provide the opportunity to study the dynamic response with THz-TDS.

This chapter provided a general introduction to the types of magneto-electric material studied in this thesis. Chapter 2 will introduce the basic physics behind the excitations characteristic of these materials and show how they couple to electromagnetic radiation. The most important experimental results in this thesis probe the interaction of light and matter in these materials, and the three main experimental techniques (terahertz time-domain spectroscopy, Raman spectroscopy and Fourier-transform infrared spectroscopy) are introduced in Chapter 3.

Chapter 4 introduces the high-temperature induced multiferroic CuO and presents an experimental observation of an electromagnon in the multiferroic phase between 213–230 K. This is the first observation of an electromagnon in CuO and to the best of my knowledge the highest temperature electromagnon in

an induced ferroelectric multiferroic yet seen. The magnon in the low temperature antiferromagnetic phase is characterised and shown to be influenced by a biquadratic exchange interaction.

In Chapter 5 an attempt to manipulate the multiferroic phase of CuO by doping with non-magnetic zinc ions is reported. The effect of doping on the static properties such as unit cell parameters and excitations such as phonons, magnons, and electromagnons are investigated.

Chapter 6 documents the effect of vertical strain on the magneto-resistance of $\text{La}_{0.7}\text{Sr}_{0.3}\text{MnO}_3:\text{ZnO}$ thin films. Static and dynamic magnetoresistance is measured and compared to pure epitaxial $\text{La}_{0.7}\text{Sr}_{0.3}\text{MnO}_3$ films. The photoconductivity is measured and its dynamic response is analysed.

Finally the results presented in thesis are summarised in Chapter 7, and some promising extensions of these studies, and other directions for future work in the field, are mapped out.

Chapter 2

Magnons and electromagnons

Phonon, magnon and electromagnon excitations characterise the dynamics of multiferroic materials. This chapter serves to sketch out the existing theoretical models of electromagnons, introducing magnons along the way. In any material with a crystal lattice, a small displacement of atoms from their equilibrium positions produces a restoring force. Since these atoms are coupled together, full equations of motion for all atoms in the solid lead to collective vibrational modes: phonons. These phonons are plane waves characterised by a frequency, ω , wavevector, \mathbf{q} , and polarisation. Similarly, in a material containing a spin lattice, small oscillations of spins about the fully ordered state produce restoring forces and can lead to plane wave spin oscillations known as magnons.

In this chapter I will introduce magnons and show how these collective excitations couple to light. Building on this foundation I will then summarise the theoretical description of two distinct types of electromagnon: the Dzyaloshinskii-Moriya electromagnon and the Heisenberg electromagnon, and the different ways they couple to light.

The discussion will be presented within the framework of a semi-classical

approximation where spins are treated as vectors with a fixed length - also known as Heisenberg spins. This follows the way that the subject has been presented in the literature [26; 37; 76].

2.1 Magnons

In this thesis the approach to describing spin dynamics follows three steps. Firstly, a spin Hamiltonian is written down that captures the key interactions in the system. Using this Hamiltonian, an “effective field” is calculated to encompass all interactions felt by a single spin. Finally, the Landau-Lifshitz-Gilbert (LLG) equation is solved to find a dispersion relation for the system.

The starting point for this exposition is the Landau-Lifshitz equation describing the motion of the spin angular momentum, \mathbf{S} , in the presence of an effective field, \mathbf{H}_{eff} [77].

$$\frac{\partial \mathbf{S}}{\partial t} = \gamma \mathbf{H}_{\text{eff}} \times \mathbf{S} \quad (2.1)$$

This equation of motion is simply an expression of Newton’s second law: a change in spin angular momentum is caused by the torque applied by the effective field. The proportionality constant, $\gamma = g|e|/2m$, is known as the gyromagnetic ratio. The spins are driven to align along the effective field, which causes precession about the equilibrium direction. Gilbert added an improved damping term to account for dissipation in the system [78], leading to the well known Landau-Lifshitz-Gilbert equation, expressed for the j th spin:

$$\frac{\partial \mathbf{S}_j}{\partial t} = \gamma \mathbf{H}_{\text{eff}} \times \mathbf{S}_j - \frac{\lambda \mathbf{S}_j \times (\mathbf{H}_{\text{eff},j} \times \mathbf{S}_j)}{\hbar S^2} \quad (2.2)$$

The damping parameter is typically small ($\lambda \ll 1$). While the LLG equation

is widely used in modelling of magnetic excitations, for clarity I will drop the damping term now and proceed as if $\lambda = 0$.

In order to make use of the LLG model it is necessary to express the effective field in terms of the Hamiltonian. One can express the effective field as the partial derivative of the Helmholtz free energy with respect to the spin: $\mathbf{H}_{\text{eff}} = (\partial F / \partial(\gamma \hbar \mathbf{S}))$. At temperatures well below the ordering temperature the free energy F approaches the internal energy expressed by the semi-classical Hamiltonian \mathcal{H} . In this limit the effective field can be expressed as follows:

$$\mathbf{H}_{\text{eff},j} = \frac{1}{\gamma \hbar} \frac{\partial \mathcal{H}}{\partial \mathbf{S}_j} \quad (2.3)$$

Now it is possible to solve the LLG equation for $\mathbf{S}_j(\omega, \mathbf{q}, H_\omega)$. Typically it is the magnon dispersion relation and pattern of spin movement that is of interest.

2.1.1 1-D Heisenberg ferromagnet

Possibly the simplest form of magnetic ordering is the isotropic one-dimensional Heisenberg ferromagnet with nearest-neighbour exchange. This can be expressed by the following Hamiltonian:

$$\mathcal{H} = -J \sum_j \mathbf{S}_j \cdot \mathbf{S}_{j+1} \quad (2.4)$$

In the ground state all of the spins are aligned along some direction $\mathbf{S}_j = \mathbf{S}_0$. Here, the spin wave dispersion will be calculated for this system using the method outlined above, before proceeding to investigate the effects of extra terms in the

Hamiltonian. First the effective field is calculated using Eqn. 2.3:

$$\mathbf{H}_{\text{eff},j} = \frac{-J}{\gamma\hbar}(\mathbf{S}_{j-1} + \mathbf{S}_{j+1}) \quad (2.5)$$

The effective field is then substituted into Eqn. 2.2 and the damping parameter set equal to zero, giving

$$\frac{\partial \mathbf{S}_j}{\partial t} = \frac{J}{\hbar} \mathbf{S}_j \times (\mathbf{S}_{j-1} + \mathbf{S}_{j+1}) \quad (2.6)$$

A plane wave solution is sought for the equation of motion for \mathbf{S}_j , of the form

$$\mathbf{S}_j = \mathbf{S}_0 + \mathbf{A}e^{i(qaj-\omega t)} \quad (2.7)$$

By assuming that $|\mathbf{A}| \ll |\mathbf{S}_0|$ and that the length of each spin is constant, one can assert that $\mathbf{A} \cdot \mathbf{S}_0 = 0$ to first order. If \mathbf{S}_0 is taken to be along the z -axis then the following coupled equations result from the substitution of Eqn. 2.7 into 2.6:

$$\begin{aligned} -i\omega A_x &= \frac{2J}{\hbar}(1 - \cos qa)(-S_0 A_y) \\ -i\omega A_y &= \frac{2J}{\hbar}(1 - \cos qa)(S_0 A_x) \end{aligned} \quad (2.8)$$

The dispersion relation can now be deduced:

$$\omega = \frac{2JS}{\hbar}(1 - \cos qa) \quad (2.9)$$

Spin waves in a simple 1-D Heisenberg ferromagnet are gapless and have a quadratic dispersion at low \mathbf{q} , as plotted in Fig. 2.1. Substituting back into Eqn. 2.8 shows that $A_x = iA_y$, meaning that the x and y components are $\pi/2$

out of phase. That is, the spins will rotate about \mathbf{S}_0 as depicted in Fig. 2.2.

2.1.2 Turning on the interactions

Magneto-electric multiferroics typically exhibit a large number of complex and competing interactions. Before continuing to investigate magnons in the more complicated incommensurate spin-spiral structures of the induced multiferroics it is useful to note the effects of various interactions important in these materials on the simpler background of the 1-D Heisenberg ferromagnet. Single-ion anisotropy is a phenomenological way to express the preferred spin orientation determined by the environment of the atom or crystal field. Biquadratic exchange can be related to the fourth order expansion of the hopping matrix element that gives rise to linear Heisenberg exchange [16]. The Hamiltonians considered are as follows:

$$\text{Heisenberg} \quad \mathcal{H}_0 = -J \sum_j \mathbf{S}_j \cdot \mathbf{S}_{j+1} \quad (2.10)$$

$$\text{Constant external magnetic field} \quad \mathcal{H}_{\text{ext}} = \mathcal{H}_0 + \gamma \hbar \sum_j \mathbf{H} \cdot \mathbf{S}_j \quad (2.11)$$

$$\text{Single-ion anisotropy} \quad \mathcal{H}_{\text{sia}} = \mathcal{H}_0 - K \sum_j (\hat{\mathbf{n}}_z \cdot \mathbf{S}_j)^2 \quad (2.12)$$

$$\text{Biquadratic exchange} \quad \mathcal{H}_{\text{biq}} = \mathcal{H}_0 + -B \sum_j (\mathbf{S}_j \cdot \mathbf{S}_{j+1})^2 \quad (2.13)$$

$$\text{Next-nearest neighbour exchange} \quad \mathcal{H}_{\text{nnn}} = \mathcal{H}_0 + J_{\text{nnn}} \sum_j \mathbf{S}_j \cdot \mathbf{S}_{j+2} \quad (2.14)$$

The dispersion relations stated below show that both application of an external magnetic field and single-ion anisotropy can cause a gap to appear in the spectrum at $\mathbf{q} = 0$. Biquadratic exchange re-scales the energy of the interaction whilst introduction of next-nearest exchange alters the functional form reducing the maximum energy to lower wavevectors [80]. A splitting of the energy levels

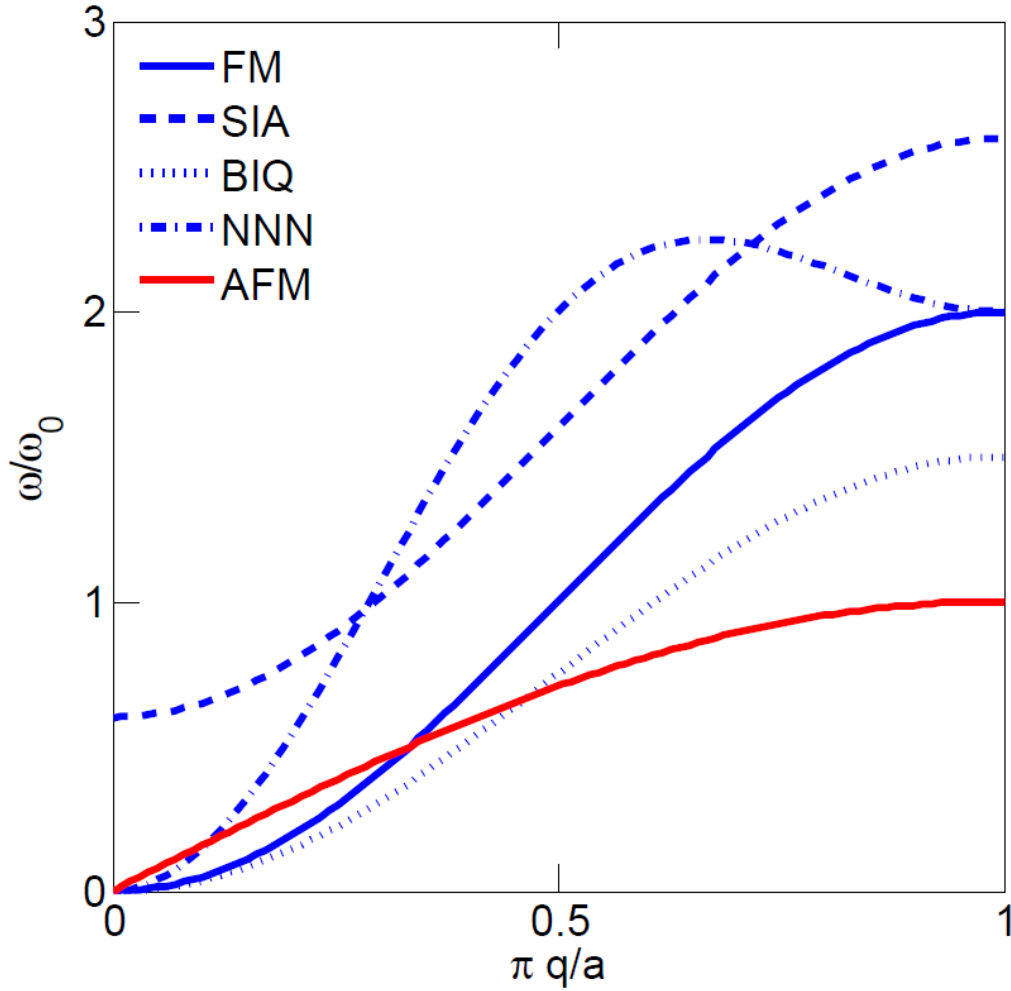


Figure 2.1: **Dispersion relations for 1-D Heisenberg magnets.** Note that the dispersion relation for the antiferromagnet is plotted over the reduced Brillouin zone where $a' = 2a$ for ease of comparison after doubling of the antiferromagnetic unit cell.

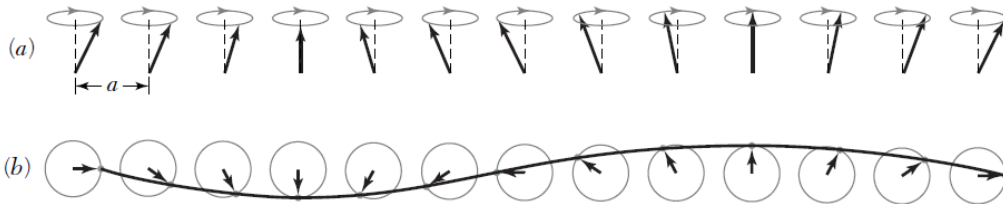


Figure 2.2: **Visualisation of a spin wave on a line of spins.** (a) Perspective view. (b) View down the z -axis. Reproduced from Ref. [79].

occurs when there are non-equivalent spins present in the system.

$$\text{Heisenberg} \quad \omega_0 = \frac{2JS}{\hbar}(1 - \cos qa) \quad (2.15)$$

$$\text{Constant external field} \quad \omega_{\text{ext}} = \omega_0 + \gamma H \quad (2.16)$$

$$\text{Single-ion anisotropy} \quad \omega_{\text{sia}} = \omega_0 + \frac{2KS}{\hbar} \quad (2.17)$$

$$\text{Biquadratic exchange} \quad \omega_{\text{biq}} = \omega_0 \left(\frac{J + 2BS(S-1)}{J} \right) \quad (2.18)$$

$$\text{Next-nearest neighbour exchange} \quad \omega_{\text{nnn}} = \omega_0 + \frac{2S}{\hbar} J_{\text{nnn}}(1 - \cos 2qa) \quad (2.19)$$

The dispersion relations for each of these cases are summarised visually in Fig. 2.1.

2.1.3 Frequency-dependent permeability tensor

In order to probe the nature of the interaction between spin systems and magnetic fields, both static and time-varying such as in an electromagnetic wave, it is instructive to add constant and oscillatory magnetic fields to the effective field of a 1-D Heisenberg ferromagnet as previously calculated in Eqn. 2.5. We consider the case where $q = 0$ for the incident field since the wavevector of far-infrared light is about six orders of magnitude less than the wavevector at the Brillouin zone boundary.

$$\mathbf{H}_{\text{eff},j} = \frac{-J}{\gamma\hbar}(\mathbf{S}_{j-1} + \mathbf{S}_{j+1}) + \mathbf{H} + \mathbf{H}_\omega e^{-i\omega t} \quad (2.20)$$

Using the full LLG equation (Eqn. 2.2) including damping characterised by λ the expression simplifies to the following if we assume that $|\mathbf{A}| \sim |\mathbf{H}_\omega| \ll |\mathbf{S}_0|$. This allows us to neglect any terms second order in either \mathbf{A} or \mathbf{H} . Furthermore we assume that the incident oscillating field is polarised perpendicular to the initial

direction of spins, as are the resulting spin oscillations.

$$\left. \frac{\partial \mathbf{S}_j}{\partial t} \right|_{\mathbf{q} \rightarrow \mathbf{0}} = -\gamma \mathbf{A} \times \mathbf{H} - \gamma \mathbf{S}_0 \times \mathbf{H}_\omega + \frac{\lambda H}{\hbar S} \mathbf{A} - \frac{\lambda}{\hbar} \mathbf{H}_\omega \quad (2.21)$$

Looking for plane wave solutions we find an expression for the spin oscillation amplitude \mathbf{A} in terms of the driving magnetic field \mathbf{H}_ω :

$$\mathbf{A} = \frac{\gamma S}{(\omega_0^2 + \Gamma^2/4) - \omega^2 - i\omega\Gamma} \begin{pmatrix} -\omega_0(1 + \Gamma^2/4\omega_0^2) + i\Gamma\omega/4\omega_0 & -i\omega \\ i\omega & -\omega_0(1 + \Gamma^2/4\omega_0^2) + i\Gamma\omega/4\omega_0 \end{pmatrix} \mathbf{H}_\omega$$

The first term on the RHS is a Lorentzian oscillator where we have made the following substitutions in order to simplify the expression: $\omega_0 = \gamma H$ and $\Gamma = 2\lambda H/\hbar S$. As may be expected, the zone-centre magnon is gapped with a frequency proportional to the constant external field (see Eqn. 2.16), although this could also be caused by a single-ion-anisotropy term in the Hamiltonian. The damping term Γ is proportional to the dimensionless damping parameter from the LLG equation.

Using this relation between the dynamic magnetisation and driving field we can express the result in terms of a susceptibility or alternatively a permeability: $\mathbf{M}_\omega = \hat{\chi} \mathbf{H}_\omega = (\hat{\mu}_r - \hat{\mathbf{I}}) \mathbf{H}_\omega = -n\gamma\hbar \mathbf{A}$ where n is the volume density of spins. Permeability and refractive index $\tilde{n} = \sqrt{\epsilon\mu}$ are the language used by optical spectroscopists so we present the permeability in the case where the damping is small, and we can therefore ignore terms containing Γ^2 .

$$\hat{\mu}_r - \hat{\mathbf{I}} = \frac{\Delta\mu\omega_0^2}{\omega_0^2 - \omega^2 - i\omega\Gamma} \begin{pmatrix} 1 - i\omega\Gamma/2\omega_0^2 & -i\omega/\omega_0 \\ i\omega/\omega_0 & 1 - i\omega\Gamma/2\omega_0^2 \end{pmatrix} \quad (2.22)$$

We have made a final simplification by setting $\Delta\mu = n\gamma\hbar S/H = M_s/H$ which we

can also express in terms of a saturation magnetisation.

2.1.4 Simple collinear antiferromagnet

In contrast to the relative simplicity of ferromagnetic structures, there are many different ways of ordering spins antiferromagnetically on a 3-D lattice. This complexity is increased further by the prospect of incommensurate order such as spin spirals and helices. Electromagnons in induced multiferroics have been modelled phenomenologically using a method known as the “co-rotating frame formalism”. A treatment of the simplest 1-D Heisenberg antiferromagnet with this technique serves well to illustrate its power, giving a flavour of how it can be applied to more complicated problems. The Hamiltonian is the same as for the ferromagnetic case (Eqn. 2.23), except now J is positive.

$$\mathcal{H} = J \sum_j \mathbf{S}_j \cdot \mathbf{S}_{j+1} \quad (2.23)$$

The basic idea of the co-rotating reference frame method is to introduce a reference frame which is rotated around the axis of the chain by π at each step when moving along the chain of spins. Therefore the j th spin always points in the same direction in the rotated frame. The effect is that an antiferromagnetic order in real space is transformed into ferromagnetic order in the co-rotating frame. This means that a unit cell of only one spin is needed to describe the system, rather than two antiparallel spins in the unit cell of an antiferromagnet treated solely in real space. The co-rotating frame treatment is also beneficial for incommensurate spin spiral structures. The rotation applies only to the spins - the crystal lattice is unaffected. If the spin chain is along the x -axis then the rotation matrix for

angle α around the axis is:

$$\hat{\mathbf{R}}_\alpha = \begin{pmatrix} 1 & 0 & 0 \\ 0 & \cos \alpha & \sin \alpha \\ 0 & -\sin \alpha & \cos \alpha \end{pmatrix} \quad (2.24)$$

Using the standard procedure above with the LLG equation (not considering damping this time) we now look for solutions of the form:

$$\mathbf{S}_j = \hat{\mathbf{R}}_\pi^j (\mathbf{S}_0 + \mathbf{A} e^{i(qaj - \omega t)}) = \begin{pmatrix} 0 \\ 0 \\ (-1)^j S \end{pmatrix} + \begin{pmatrix} A_x \\ (-1)^j A_y \\ 0 \end{pmatrix} e^{i(qaj - \omega t)} \quad (2.25)$$

Where the first term indicates we now have an antiferromagnetic ground state, with spins either parallel or antiparallel to z . The solution is now straightforward and provides the well known result for a 1-D Heisenberg nearest-neighbour antiferromagnet:

$$\omega = \frac{2JS}{\hbar} \sin qa \quad (2.26)$$

Note that the parameter a here is still the distance between adjacent spins. In order to compare results over the first Brillouin zone it is necessary to make the substitution $a_{\text{mag}} = 2a$.

2.1.5 Incommensurate spin cycloid

In this section a Hamiltonian used to describe the incommensurate spin-cycloid systems is presented, along with a modification to the co-rotating frame scheme used in the previous section in order to deal with the cycloid structure. This

Hamiltonian will be used in Sec. 2.2 to describe electromagnons, which were first discovered in incommensurate rare-earth manganites [32]. GdMnO₃, TbMnO₃ and DyMnO₃ have all been described by the following Hamiltonian proposed by Kida *et al.* [15].

$$\begin{aligned} \mathcal{H}_0 = \sum_j \sum_k \sum_l [& -J(\mathbf{S}_{j,k,l} \cdot \mathbf{S}_{j-1,k+1,l}) - J(\mathbf{S}_{j,k,l} \cdot \mathbf{S}_{j+1,k+1,l}) \\ & + J_{\text{nnn}}(\mathbf{S}_{j,k,l} \cdot \mathbf{S}_{j,k+2,l}) + J_c(\mathbf{S}_{j,k,l} \cdot \mathbf{S}_{j,k,l+1}) + K(\hat{\mathbf{n}}_x \cdot \mathbf{S}_{j,k,l})^2] \end{aligned} \quad (2.27)$$

The three summations over indices j, k , and l cover the x, y , and z directions respectively. The first two terms in the Hamiltonian are ferromagnetic exchanges along orthogonal directions in the xy -plane. Microscopically these relate to superexchange between nearest neighbour Mn spins via oxygen orbitals. The third term is antiferromagnetic next-nearest neighbour exchange along an intermediate direction also in the xy -plane. The fourth term is also antiferromagnetic, this time along the z -axis. The final term associates an energy cost with spins pointing in the x -direction, therefore setting the yz -plane as the easy-plane. This fixes the direction of the cycloid caused by frustration between the other competing interactions.

As in Sec. 2.1.4, the rotation operator is then applied to the fixed spins to get the ground state and magnons.

$$\mathbf{S}_{j,k,l} = \hat{\mathbf{R}}_{k\alpha+l\pi}(\mathbf{S}_0 + \mathbf{A}e^{i(q_a a j + q_b b k + q_c c l - \omega t)}) \quad (2.28)$$

Here $\hat{\mathbf{R}}_{k\alpha}$ rotates the spins around the x -axis as one moves along the y -direction creating the yz cycloid while $\hat{\mathbf{R}}_{l\pi}$ creates the antiferromagnetic order in the z -direction. These more complex dispersion relations can still be solved analytically

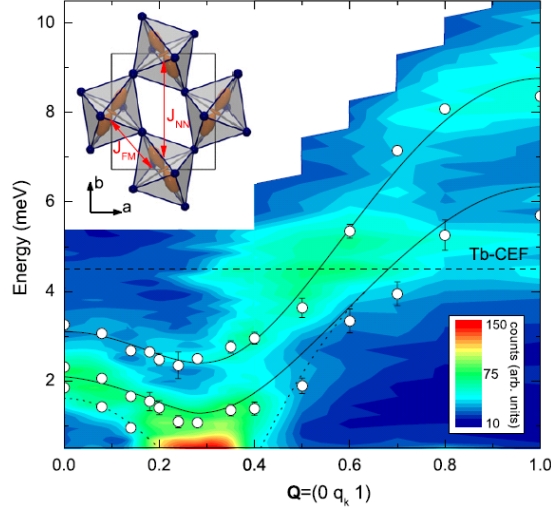


Figure 2.3: **Inelastic neutron scattering in TbMnO_3 at 17 K.** Data taken as \mathbf{q} increases along the b -direction. Colours map the inelastic scattering intensity, open circles are the estimated magnon frequencies and the solid lines are calculated dispersion relations. (Inset) View of the structure down the z -axis. Note that the J_{NN} in the figure corresponds to J_{nmn} in Eqn. 2.27 and J_{FM} to our J in the first term of the Hamiltonian. Reproduced from Ref. [35].

and have been successfully used to describe experimental data in cycloidal magnets, as illustrated by the inelastic neutron scattering data shown in Fig. 2.3.

Optical spectroscopy techniques such as FTIR, Raman and THz-TDS as used in this thesis are generally less able to distinguish between models than inelastic neutron scattering data, being limited by the momentum of the incident photons to probe only the region where $q \sim 0$. ESR measurements are also used to probe the GHz energy region of the spectrum. However, even these probes of the zone-centre magnetic excitations are useful for distinguishing between various models with careful measurement of energies and selection rules. As will be seen in the next section on electromagnons there are also instances where light can couple to magnons with non-zero wavevector either through bi-magnon processes or indirectly via the electric field of light.

2.2 Electromagnons

Until now all the discussion has been concerned with purely magnetic excitations, visible in optical spectroscopy due to the magnetic field of electromagnetic radiation. Now we turn our attention to magnetic excitations that are electrically active: electromagnons. Clearly in order to have an electromagnon there must be spin-phonon coupling in the material. This can occur in many ways. However, two distinct explanations have been proposed for the electromagnons seen so far in the manganites and other materials. The first involves a direct coupling of the electric field of incident light to a polarisation induced by the spin cycloid itself; the Dzyaloshinskii-Moriya electromagnon. Secondly a polar lattice vibration can dynamically modulate the magnetic exchange along a spin structure inducing a magnetic excitation; the Heisenberg model.

2.2.1 Dzyaloshinskii-Moriya model

The Dzyaloshinskii-Moriya model has been successfully applied to describe the static electric polarisation in incommensurate cycloidal antiferromagnets [81; 82]. The DM term was introduced phenomenologically [8] to the Hamiltonian in order to account for a modification of the superexchange by the spin-orbit coupling [83]. The most general form is as follows:

$$\mathcal{H}_{\text{DM}} = \sum_{\alpha} \mathbf{d}_{\alpha}(\mathbf{r}_{j+\frac{1}{2}}) \cdot (\mathbf{S}_j \times \mathbf{S}_{j+1}) \quad (2.29)$$

Where the DM vectors \mathbf{d}_{α} are parameterised by the strength of the interaction γ , the vector connecting two adjacent spins in the cycloid $\boldsymbol{\delta}$, and the displacement of the superexchange-mediating oxygen from the line connecting the spins \mathbf{r} , as

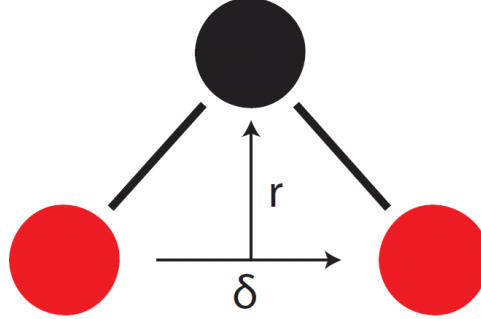


Figure 2.4: **Dzyaloshinskii-Moriya parameters.** Magnetic ions (red) interact through superexchange via an oxygen ion (black). The DM parameter δ connects neighbouring spins and \mathbf{r} indicates the vector displacement of the oxygen from the line connecting adjacent spins.

illustrated in Fig. 2.4, and according to

$$\mathbf{d}_\alpha = \gamma(\boldsymbol{\delta}_{j \rightarrow j+1} \times \mathbf{r}_{j+\frac{1}{2}}) \quad (2.30)$$

With a vector identity the expression can be re-written:

$$\mathcal{H}_{\text{DM}} = \gamma \sum_j \mathbf{r}_{j+\frac{1}{2}} \cdot ((\mathbf{S}_j \times \mathbf{S}_{j+1}) \times \boldsymbol{\delta}_{j \rightarrow j+1}) \quad (2.31)$$

It is the oxygen displacements, \mathbf{r} , that lead to the induced polarisation, \mathbf{P} . To treat this fully it is necessary to consider lattice vibrations in the Hamiltonian. However, if the interaction strength is small then it is possible to treat it as a perturbation to the ground state and the magnon dispersion can be calculated for the incommensurate cycloid using Eqn. 2.27. The extra DM energy is now linear in oxygen displacement and so can lead to an adjustment of equilibrium positions to minimise the total energy of the system. Using the methods outlined previously the total static and dynamic polarisations can be calculated, giving good agreement with experiment in the case of the static polarisation for a number of

materials (not just restricted to the rare-earth manganites). The space-dependent polarisation $\mathbf{P}_{j,k,l}$, up to terms linear in wave amplitude, \mathbf{A} can be shown to be:

$$\begin{aligned} \mathbf{P}_{j,k,l}(\mathbf{q}) = & 2bS^2 \sin(\alpha) \begin{pmatrix} 0 \\ 0 \\ 1 \end{pmatrix} + 2bSA_y e^{i\mathbf{q}\cdot\mathbf{r}} \cos(\alpha) (\cos(q_a a) e^{iq_b b} - 1) \begin{pmatrix} 0 \\ 0 \\ 1 \end{pmatrix} \\ & + 2SA_x e^{i(\mathbf{q}+\mathbf{Q})\cdot\mathbf{r}} \begin{pmatrix} ib(\cos(q_a a) e^{iq_b b} - e^{i\alpha}) \\ a \sin(q_a a) e^{iq_b b} \\ ia \sin(q_a a) e^{iq_b b} \end{pmatrix} \\ & + 2SA_x e^{i(\mathbf{q}-\mathbf{Q})\cdot\mathbf{r}} \begin{pmatrix} -ib(\cos(q_a a) e^{iq_b b} - e^{i\alpha}) \\ -a \sin(q_a a) e^{iq_b b} \\ ia \sin(q_a a) e^{iq_b b} \end{pmatrix} \end{aligned} \quad (2.32)$$

where $\cos(\alpha) = J/2J_{\text{nn}}$ is the angle between adjacent spins, \mathbf{Q} is the modulation vector of the static cycloid, and \mathbf{q} is the wavevector in the co-rotating frame. The first term of Eqn. 2.32 gives the static part of the polarisation, which lies along the z -axis for DyMnO₃ with a b - c (or equivalently y - z) cycloid. The three terms linear in \mathbf{A} form the dynamic part of the polarisation. These terms must have a harmonic spatial dependence or they will cancel out after summing over the whole lattice. This constraint means the only non-zero total polarisation occurs for $\mathbf{q} = \pm\mathbf{Q}$. Substituting $\mathbf{Q} = (0, \frac{\alpha}{b}, \frac{\pi}{c})$ for DyMnO₃ gives the much simplified expression: $\mathbf{P}_{j,k,l} = P_{j,k,l}^{(x)}(+\mathbf{Q}) = P_{j,k,l}^{(x)}(-\mathbf{Q}) = 2bSA_x \sin(\alpha)$. Therefore both the magnons at $\pm\mathbf{Q}$ are electrically active and so a symmetric excitation of both magnons will be present as an electromagnon active for $E_\omega \parallel x$ for a y - z cycloid. The simultaneously present magnetic moment in the y -direction means that this eigenmode of the cycloid is also excited for $H_\omega \parallel y$.

These features serve to distinguish the DM and Heisenberg electromagnons from the point of view of the spectroscopist: The DM electromagnon selection rules are tied to the magnetic cycloid, and the mode is both electrically and magnetically active along different crystal axes. One test of this rule is to induce a spin-flop transition by applying a magnetic field to the sample such that the plane of the cycloid rotates by $\pi/2$ about the wave vector: if the selection rules also rotate by the same degree then this is consistent with a DM electromagnon. The same does not hold for a Heisenberg electromagnon, as we shall see in the next section.

The strength of the coupling to light is determined by γ which tends to be small. Although it was the DM electromagnon that was first proposed to explain the experimental data on TbMnO_3 [41], this was subsequently shown not to be the case for the strongest electromagnons by applying the spin-flop test to the selection rules. A recent study of a less intense electromagnon in DyMnO_3 , summarised in Fig. 2.5, suggests that it could be the sought-after DM electromagnon [26].

2.2.2 Heisenberg model

On realising that the DM electromagnon was not sufficient to describe all of the electrically active spin waves in the rare earth manganites, theorists looked for novel explanations. The exchange striction model of spin-phonon coupling, based on symmetric Heisenberg exchange, provided a source of inspiration. The nearest-neighbour exchange J depends upon positions \mathbf{r} of oxygen atoms in Mn–O–Mn bonds and can be expanded as a Taylor series as follows:

$$J(\mathbf{r}) = J(0) + \frac{\partial J}{\partial \mathbf{r}} \cdot \mathbf{r} = J(0) + \frac{\partial J}{\partial \phi} \frac{\partial \phi}{\partial \mathbf{r}} \cdot \mathbf{r} \quad (2.33)$$

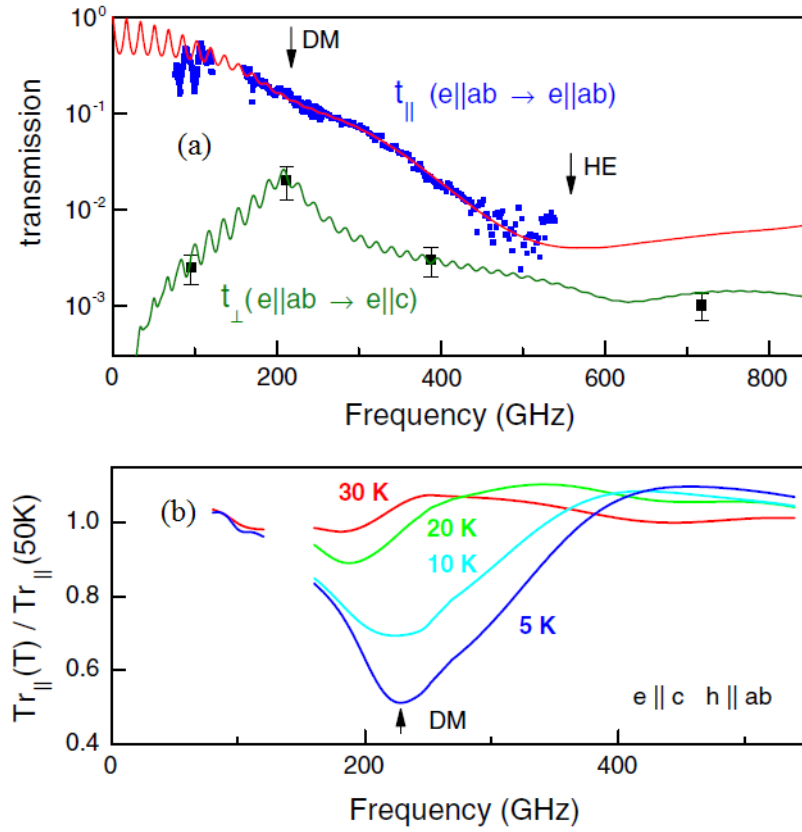


Figure 2.5: **Dzyaloshinskii-Moriya electromagnon in DyMnO_3 .** (a) Transmission spectra of DyMnO_3 in parallel (blue squares) and crossed (black squares) polarisers. The transmission is dominated by the Heisenberg electromagnon at 550 GHz (HE) while the much weaker DM electromagnon is visible at 210 GHz, excited by $E_{\omega} \parallel a$; $H_{\omega} \parallel c$ in this geometry. (b) Relative transmission for $E_{\omega} \parallel c$; $H_{\omega} \parallel b$ showing the DM electromagnon excited by the magnetic field of the light. The Heisenberg electromagnon is not active in this geometry. Reproduced from Ref. [26].

where ϕ is the Mn–O–Mn bond angle. Whilst in the DM mechanism, changes in \mathbf{r} directly contribute to the polarisation, in the framework of this mechanism it is the change in ϕ that is key. Antiferromagnetic exchange is maximised when $\phi = \pi$ and decreases according to the Goodenough-Kanamori-Anderson rules as the angle decreases. The equilibrium angle differs from π in all of the cycloidal multiferroic rare earth manganites such that $\frac{\partial J}{\partial \phi} > 0$ and is the same for all Mn–O–Mn bonds. The tilting Jahn-Teller distortions, schematically shown in Fig. 2.6(a), lead to the alternating derivative $\frac{\partial \phi}{\partial \mathbf{r}}$ such that $\frac{\partial \phi}{\partial x} \hat{\mathbf{k}} \sim (-1)^k$. By assuming that oxygen displacements are caused by the applied electric field \mathbf{E} , one can then write $\mathbf{r} \sim \mathbf{E}$ and therefore $r_x \sim E_x$. Substituting into Eqn. 2.33 and subsequently Eqn. 2.23 produces the leading term as for the simple Heisenberg antiferromagnet and the first order correction:

$$\mathcal{H} = -gE_x \sum_j \sum_k \sum_l (-1)^k [(\mathbf{S}_{j,k,l} \cdot \mathbf{S}_{j-1,k+1,l}) - J(\mathbf{S}_{j,k,l} \cdot \mathbf{S}_{j+1,k+1,l})] \quad (2.34)$$

The magnitude of the resulting polarisation is calculated straightforwardly using the thermodynamic relation $\mathbf{P} = \partial \mathcal{H} / \partial \mathbf{E}$. After substituting the details of the model for DyMnO₃ a simple expression for the dynamic polarisation is recovered: $\mathbf{P}_{j,k,l} = P_A^{(x)} \sim N S A_y \sin(\alpha)$, where N is the total number of spins.

Alternating rotations of MnO₆ octahedra allow a uniform electric field in the x -direction to induce an alternation of the nearest-neighbour exchange along the spiral propagation vector. This interaction couples the electric field to the acoustic magnon with \mathbf{k}_0 at the magnetic Brillouin-zone boundary, as illustrated by the blue circle in Fig. 2.6(b).

Although spin interactions with $E_\omega \parallel y$ and $E_\omega \parallel z$ are also symmetry-allowed, they give rise to an alternation of the exchange in a direction perpendicular to the

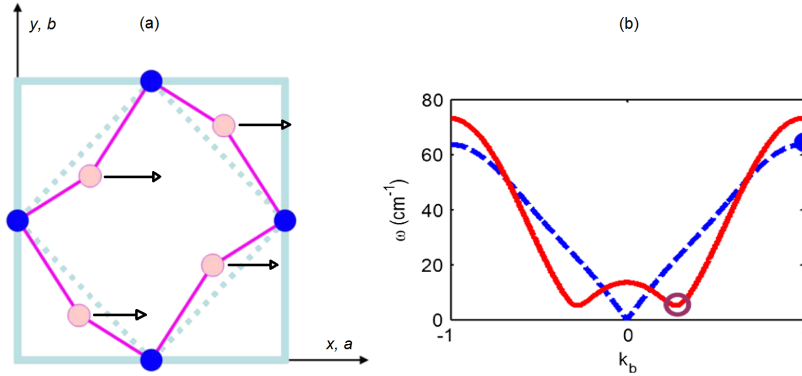


Figure 2.6: **Heisenberg electromagnon.** (a) One ab layer in the orthorhombic unit cell of a rare earth manganite showing four Mn ions (blue circles) and four oxygen ions (pink circles). A uniform displacement of oxygen ions along the x -direction induces a modulation of the nearest neighbour exchange along the y -direction. (b) Dispersion relation along the $(0\zeta 0)$ direction showing the position of the Heisenberg electromagnon (blue circle) at the Brillouin-zone boundary and DM electromagnon (open circle). Reproduced from Ref. [37].

spin-spiral propagation vector \mathbf{Q} , and do not lead to single-magnon excitations by the electric field, as neighbouring spins in these directions are collinear.

This explains why the polarisation of the electromagnon in rare earth manganites is parallel to the a -axis, and independent of the orientation of the plane of the cycloid.

Finally, in order to fully capture the electromagnon spectrum across the range of the rare-earth manganite perovskites, Mochizuki *et al.* used a model based on the Heisenberg electromagnon to produce a single excitation and add in two single-ion anisotropy terms, a DM interaction, and a biquadratic exchange term in order to fully reproduce experimental results in the systems TbMnO_3 , DyMnO_3 and $\text{Eu}_{1-x}\text{Y}_x\text{MnO}_3$ [84]. See Fig. 2.7, which shows how adding in successive interactions to the Hamiltonian can reproduce the experimentally observed optical spectrum.

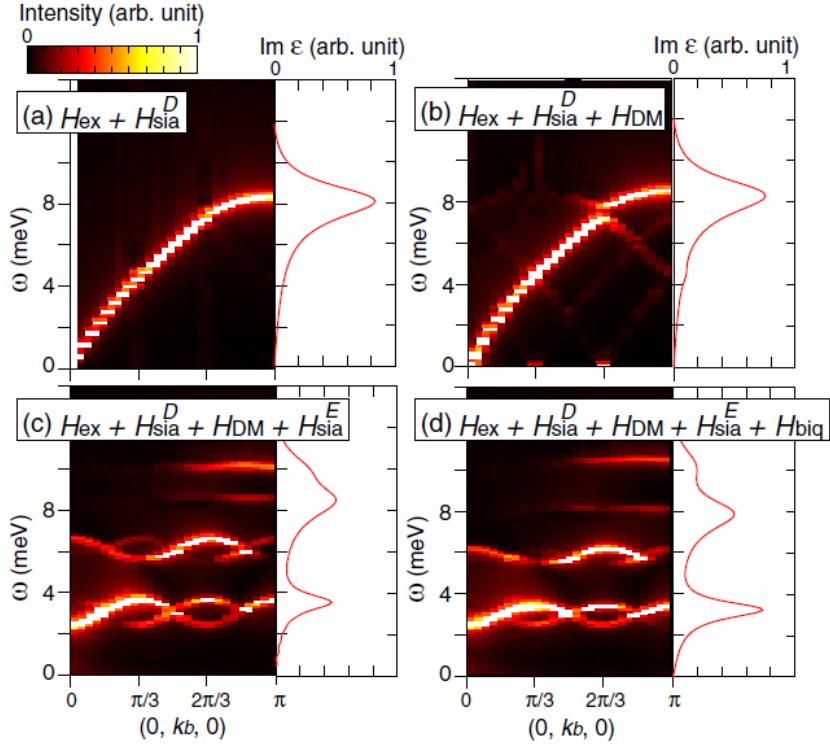


Figure 2.7: **Calculated intensity map of magnon (left panel) and electromagnon optical spectra (right panel) for each Hamiltonian successively adding the interactions.** (a) $\mathcal{H}_0 + \mathcal{H}_{\text{sia}}^{(z)}$ give a spin-spiral with uniform rotation angle. (b) Adding \mathcal{H}_{DM} induces negligibly small changes. (c) Incorporation of $\mathcal{H}_{\text{sia}}^{(xy)}$ allows for higher harmonics of the spin-spiral resulting in magnon folding and evolution of the lower-energy peak in the optical spectra. (d) The full Hamiltonian includes \mathcal{H}_{biq} and the lower-energy peak further enhanced. Reproduced from Ref. [84].

2.3 Summary

This chapter has served to provide a theoretical framework within which to understand the magnon and electromagnon dynamics in CuO; the high-temperature multiferroic investigated in Chapters 4 and 5 of this thesis. The experimental results presented in those chapters do not provide an unambiguous determination of the nature of the electromagnons in CuO. The key experimental test of the magnetic field induced spin cycloid rotation and concomitant polarisation flop is not accessible in CuO (at least not for $B < 14$ T). However symmetry arguments suggest that there is no straightforward mechanism by which a uniform displacement of oxygen ions in the Cu–O–Cu bonds can cause a modulation of the spins along the magnetic propagation vector \mathbf{Q} . Combined with the fact that the magnon in the low-temperature collinear AFM phase is about the same energy as the electromagnon in the multiferroic phase suggests that the electromagnon may well be of DM origin.

Chapter 3

Experimental Methods

In this thesis on dynamic magneto-electric effects in the complex oxide systems $\text{Cu}_{1-x}\text{Zn}_x\text{O}$ and $\text{La}_{0.7}\text{Sr}_{0.3}\text{MnO}_3:\text{ZnO}$ the key experiments were performed using the techniques of terahertz time-domain spectroscopy (THz-TDS), supported by Fourier transform infrared spectroscopy (FTIR) and Raman spectroscopy. In the following chapter I introduce THz spectroscopy, an experimental technique that has only recently come to maturity, in Sec. 3.1. Detailed descriptions of the experimental systems I used to make the measurements reported in later chapters are provided in Sec. 3.1.1. A guide to analysing THz-TDS data is supplied in Sec. 3.1.2, before further discussion of optical-pump THz-probe measurements in Sec. 3.1.3. A brief summary of FTIR spectroscopy is given in Sec. 3.2, and of Raman spectroscopy in Sec. 3.3.

Any physicist working with multiple spectroscopic techniques covering slightly different energy ranges will sooner or later encounter the question of choosing the units with which to best present their data. FTIR and Raman spectroscopists tend to use cm^{-1} , while most terahertz spectroscopists prefer THz and neutron scientists often choose meV. In this thesis I have used meV through-

out the text, occasionally presenting multiple units on graphs, as meV are more broadly favoured among physicists investigating correlated electron systems in general. Below is a rough guide to how the various energy units compare:

$$1 \text{ THz} \sim 4 \text{ meV} \sim 300 \mu\text{m} \sim 33 \text{ cm}^{-1} \sim 50 \text{ K}$$

3.1 Terahertz Time-Domain Spectroscopy

Terahertz time-domain spectroscopy (THz-TDS) has evolved into a mature technology and a powerful tool for investigating the properties of matter in the energy range 0.1–10 THz (0.4–40 meV). THz-TDS provides a direct, non-contact probe of the full complex refractive index $\tilde{n} = \sqrt{\epsilon\mu}$ of the material under investigation without recourse to Kramers-Kronig relations [85].

Historically there has been a lack of high-power, broadband, coherent sources in the THz region of the electromagnetic spectrum. The ‘THz gap’ was a consequence of the low energy limit of available optical sources and the high energy side of electronic sources [86]. Optical sources are usually quantum systems such as atoms and molecules. Radiation is emitted as the system relaxes from one quantum state to another, in quanta of energy equal to the difference between the two states. Electronic sources typically emit radiation due to acceleration of electrons under an applied voltage. Various approaches have been taken to develop spectroscopic tools capable of bridging this gap, including developments of traditional electronic approaches such as backward wave oscillators [87], high-power broadband free-electron lasers [86] and more recently narrowband quantum cascade lasers [88] which all have their own benefits and disadvantages and will not be discussed further here.

THz-TDS developed out of efforts to detect ultrashort electrical transients

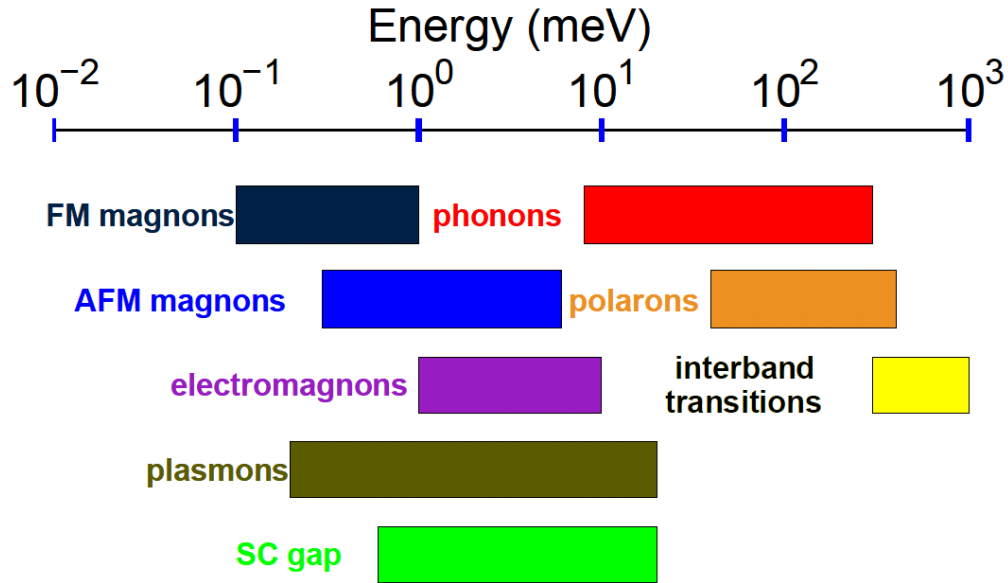


Figure 3.1: **Energy scales of selected processes in correlated electron systems**

propagating down transmission lines [89]. In the decades since the first THz-TDS experiments towards the end of the 1980's when a pulse of THz radiation was first generated and propagated through free space to a detector [90; 91], considerable development in the science and technology of both detectors and generators has occurred. The number of available techniques has multiplied and these have been applied with considerable success in a wide variety of scientific endeavours [92]. 'Black-box' table-top THz spectroscopy systems have been developed for those who want quick results with a limited range of capabilities [93]. However, for a physicist desiring state of the art bandwidth, pulse power, and sensitivity THz-TDS is still very much a self-built affair with many and various developments still occurring at a fast pace.

Diverse physical systems have unique signatures in the THz region which has led to a high impact in a multitude of scientific endeavours such as communications, plasma physics, detectors for space missions, biological physics, art history,

archaeology, medical diagnostics, and condensed matter physics, as examined by Ref. [94] and references therein.

Excitations and collective phenomena seen in correlated electron systems often have energies in the THz regime, as illustrated in Fig. 3.1. Plasmons, phonons, polarons, magnons, bi-magnons, electromagnons, Cooper pair binding energies and various thermally activated hopping processes all have unique signatures in this region of the electromagnetic spectrum [75]. Conductivity can be most fruitfully investigated using THz spectra. Various models for the complex conductivity of materials, including classical Drude-Lorentz, Drude-Smith and plasmon models; quantum descriptions such as Boltzmann models, Fermi Liquid Theory (Extended-Drude); and effective conductivity models for inhomogeneous media such as effective medium theory and thermally activated hopping models all have distinct spectral features in the THz region of the electromagnetic spectrum, as discussed in the comprehensive review article Ref. [85], and references therein.

3.1.1 Performing a THz-TDS experiment

In this section I will sketch out a generic THz-TDS experiment using Fig. 3.2 as a point of reference. Then, having seen how the amplitude of the electric field of the THz pulse can be recorded in the time domain, the next section will show how the complex refractive index of a sample can be extracted from this.

Ultrafast optical pulses

The THz-TDS experiment begins with an ultrafast pulsed infrared (IR) laser, Fig. 3.2(a). Typically 800 nm centre wavelength (1.55 eV) mode-locked Ti:Sapphire lasers are used. A semiconductor laser array is used to pump a Nd:YAG laser, which is then doubled in frequency to 532 nm (2.33 eV) and this,

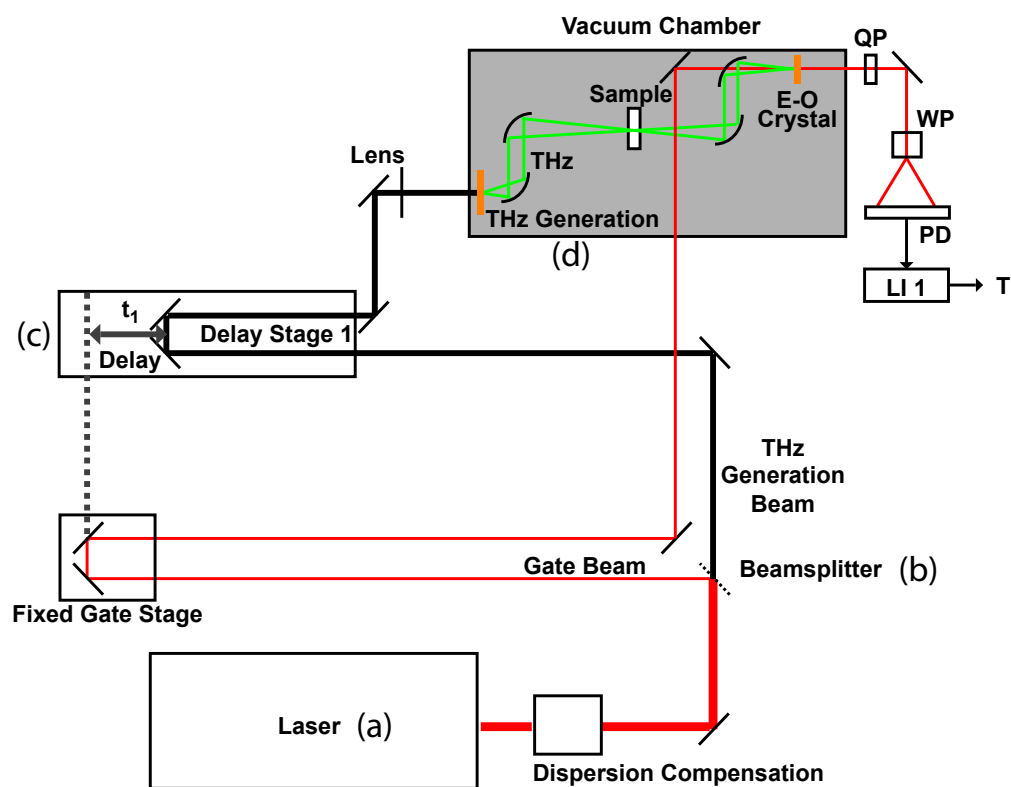


Figure 3.2: **Schematic of a THz-time domain spectroscopy experiment** Thick red lines indicate the beampath of the infrared pulse emitted from the laser. After the beamsplitter this is split into the gate beam (thin red line) and THz generation beam (black line). THz radiation is denoted by the thin green lines.

Table 3.1: **THz-TDS systems used in this thesis.** Symbols used in the table are defined here. Laser parameters: pulse centre energy, ω_p ; pulse bandwidth, $\Delta\omega_p$; pulse duration, τ_p ; repetition rate, r ; average output power, P_{average} ; and energy per pulse, E_p . Emitter parameters: photoconductive switch (PCS) bias voltage, V_{bias} ; and PCS modulation frequency, f_{mod} .

	System 1	System 2	System 3
Laser	Femtosource Scientific Pro Ti:Sapphire oscillator	Mai-Tai Ti:Sapphire oscillator	Spitfire Pro Ti:Sapphire regenerative amplifier
ω_p	1.57 eV	1.55 eV	1.55 eV
$\Delta\omega_p$	0.25 eV	0.25 eV	0.45 eV
τ_p	10 fs	100 fs	35 fs
r	74 MHz	80 MHz	5 kHz
P_{average}	0.5 W	0.7 W	3 W
E_p	7 nJ	4 nJ	0.6 mJ
Emitter	SI-GaAs PCS 3 mm thick with 4 μm gap between electrodes	SI-GaAs PCS 3 mm thick with 4 μm gap between electrodes	2 mm thick GaP crystal cut normal to $\langle 001 \rangle$
V_{bias}	$\sim 150 \text{ V}_{p-p}$	$\sim 150 \text{ V}_{p-p}$	–
f_{mod}	1.6 kHz	1.6 kHz	–
Detector	200 μm $\langle 110 \rangle$ crystal bonded onto a 6 mm thick $\langle 001 \rangle$ substrate (either ZnTe or GaP)	200 μm $\langle 110 \rangle$ crystal bonded onto a 6 mm thick $\langle 001 \rangle$ substrate (either ZnTe or GaP)	200 μm $\langle 110 \rangle$ crystal bonded onto a 6 mm thick $\langle 001 \rangle$ substrate (GaP)
Geometry	transmission or reflection	transmission	transmission
Temperature	190–300 K four-stage thermoelectric cooler	1.2–300 K liquid helium	190–300 K four-stage thermoelectric cooler
B-field	–	0–8 T superconducting magnet ($B \parallel k_\omega$)	–
Pump	–	–	1.55 eV, as THz generation pulse

in turn, pumps a Ti:sapphire crystal. Electrons in localised electronic states of the Ti^{3+} ion are excited above the lasing transition. Stimulated emission can occur into one of many vibrational states in the low energy band producing the characteristic broad spectrum of these lasers (FWHM \sim 700–900 nm). Pulses as short as 6 fs can be produced if the laser is self mode-locked by a non-linear Kerr effect [95].

Splitting the pulse

After leaving the laser, the femtosecond IR pulse passes through a beamsplitter, Fig. 3.2(b), where a small fraction ($\sim 10\%$) of the pulse is split off in order to form the ‘gate beam’ used in the electro-optic detection. As the gate beam pulse has a constant phase relationship with the remainder of the pulse (the THz generation beam) a delay stage, Fig. 3.2(c), can be used to vary the arrival time of the two pulses at the detection crystal enabling the amplitude of the THz pulse (duration a few picoseconds) to be recorded as a function of delay time from the IR pulse (duration a few tens of femtoseconds) as explained below.

THz generation

Two methods were used for generating THz radiation in the work presented in this thesis. Photoconductive switches were used with laser oscillator systems. Optical rectification was used in the higher power regenerative amplifier system for pump-probe studies.

Photoconductive switches In a photoconductive switch (PCS) the incident laser pulse is focussed onto the surface of a semiconducting wafer to excite carriers into the conduction band. A bias voltage is applied to the semiconductor via

surface contacts which accelerates the newly formed electrons and holes towards the oppositely charged electrodes. This in turn manifests as a transient electric dipole which radiates an electromagnetic pulse. The size of the signal is increased for thicker wafers as more carriers are excited, however there is a trade-off as the bandwidth decreases due to self-absorption [96]. It is desirable for the switch material to have fast photocurrent rise and decay times and high carrier drift velocities for maximum bandwidth [97].

We use semi-insulating (SI) GaAs with a band gap $E_g = 1.42$ eV at 300 K. On the surface of the wafer, two gold contacts were evaporated $400 \mu\text{m}$ apart with parallel straight edges leaving a strip of exposed semiconductor in between. A voltage between 100 and 200 V peak-to-peak was applied. Switch thicknesses varied between $6 \mu\text{m}$ and 2 mm of SI-GaAs.

Optical rectification Optical rectification occurs in non-linear media with non-zero second order dielectric susceptibilities: $\chi^{(2)} \neq 0$. Here a polarisation is induced in the material proportional to the electric field of the incident laser pulse: $P^{(2)} \propto \chi^{(2)} E_0^2 \cos^2(\omega t) = \chi^{(2)} E_0^2 [1 - \cos(2\omega t)]/2$. The ‘zero-frequency’ component gives a d.c. polarisation in the case of incident monochromatic light with frequency ω . However, in the case of a broadband pulse, the d.c. polarisation will be modulated by the pulse envelope function. This time-dependent polarisation in turn produces a THz pulse with $E_{\text{THz}} \propto \ddot{P}_0$ [98]. Two important properties influencing the choice of detection crystal are the electro-optic coefficient and the energy of the lowest TO phonon mode. Absorption due to a phonon imposes an upper limit on the bandwidth achievable with the two detection crystal. I used, ZnTe and GaP. The lowest energy optical phonon at the gamma point in ZnTe is at 5.3 THz (22 meV) [99]. In GaP the phonon energy is 11.1 THz (46 meV)

[100]. The electro-optic coefficient r_{41} is a constant of proportionality between the electric field amplitude and induced birefringence in these cubic materials. $r_{41}(\text{ZnTe}) = 4r_{41}(\text{GaP})$, so the detection crystal is chosen for each experiment based on a compromise between desired bandwidth and signal size [101; 102].

Propagation of the THz pulse

The PCS or electro-optic crystal is placed at the focus of an off-axis parabolic mirror (OAP) which collects and collimates the emitted THz light. OAPs are used to manipulate the THz pulse in order to eliminate the need for dispersive optics, which would reduce the quality of the pulse. The THz radiation is contained within a vacuum box so that the strong water vapour absorption lines present between 2 meV and 20 meV can be removed from the spectrum, greatly enhancing the signal to noise ratio of the experiment [103].

THz detection

Electro-optic sampling was used to detect THz radiation in all experiments reported in this thesis. Electro-optic sampling makes use of the Pockels effect whereby an applied voltage induces a change in birefringence in a detector crystal. ZnTe and GaP were both used, cut parallel to the $\langle 110 \rangle$ plane [104]. The IR gate pulse and the THz pulse travel co-linearly through the crystal and if the pulses overlap in time then the instantaneous THz electric field induces a change in the birefringence of the crystal which rotates the plane of polarisation of the gate pulse. After the detector crystal the pulse travels through a quarter-wave plate which is rotated to balance the horizontal and vertical components of the gate beam in the absence of the THz pulse. The gate pulse then travels through a Wollstone prism which separates the horizontal and vertical polarisation com-

ponents spatially. Each polarisation component then hits a separate photodiode. The balanced photodiode circuit measures the change in birefringence that is linearly dependent on the THz electric field amplitude for small changes. By scanning the delay stage the electric field of the THz pulse can be mapped out as a function of time. The photodiode circuit is connected to a lock-in amplifier that is phase locked either to the square-wave modulation voltage applied to the photoconductive switch or an optical chopper if optical rectification is used to generate the THz. It is this full recovery of both amplitude and phase information that makes THz-TDS such a powerful technique for measuring the complex refractive index \tilde{n} .

Properties of the THz pulse

Fig. 3.3(a) shows a reference THz pulse in the time domain (blue) and at a later time, a pulse after travelling through the sample (red). The time delay of the pulse peak is due to the real part of the refractive index of the sample. Fig. 3.3(b) shows the sample and reference spectra. Any additional peaks in the time domain introduce Fabry-Perot oscillations in the frequency response (red), which can be removed by truncating the time domain signal either after the ‘pre-pulse’ (an artifact of the experiment) or before the first internal reflection producing a much cleaner signal.

Three main metrics are used to describe the properties of the THz pulse; resolution, bandwidth and signal-to-noise ratio. The resolution is inversely proportional to the time domain window meaning that it is desirable to measure over the largest range possible. With an optically thick sample, it is usually practical only to measure to the first internal reflection so this normally sets the limit on resolution. This applies even for the thin-film samples measured in this thesis as

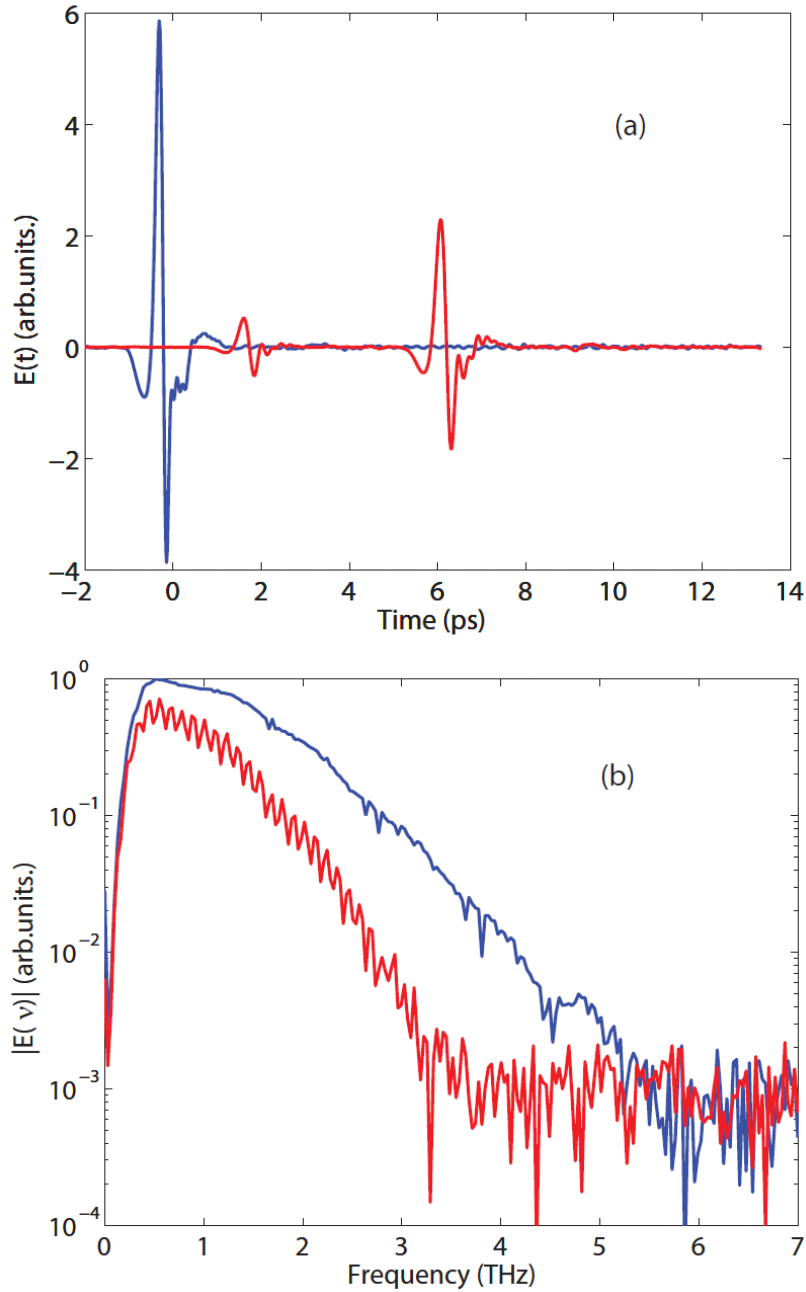


Figure 3.3: **Typical THz-TDS data obtained on an optically thick sample.** (CuO, 1.3 mm thick). (a) The time-domain electric field reflected from the sample E_s (red) is delayed by 6.4 ps with respect to the reference electric field E_r (blue) owing to the refractive index of the medium. The Fresnel transmission coefficients and absorption within the sample account for the reduction in the amplitude of E_s . A small ‘pre-pulse’ is visible in the sample, at 1.6 ps. (b) Fourier transform spectra of time-domain data in (a) for E_s (red) and E_r (blue). The pre-pulse produces the oscillatory shape of E_s , in the same way an internal reflection would, and can be removed by restricting the time domain data to begin at say 4 ps.

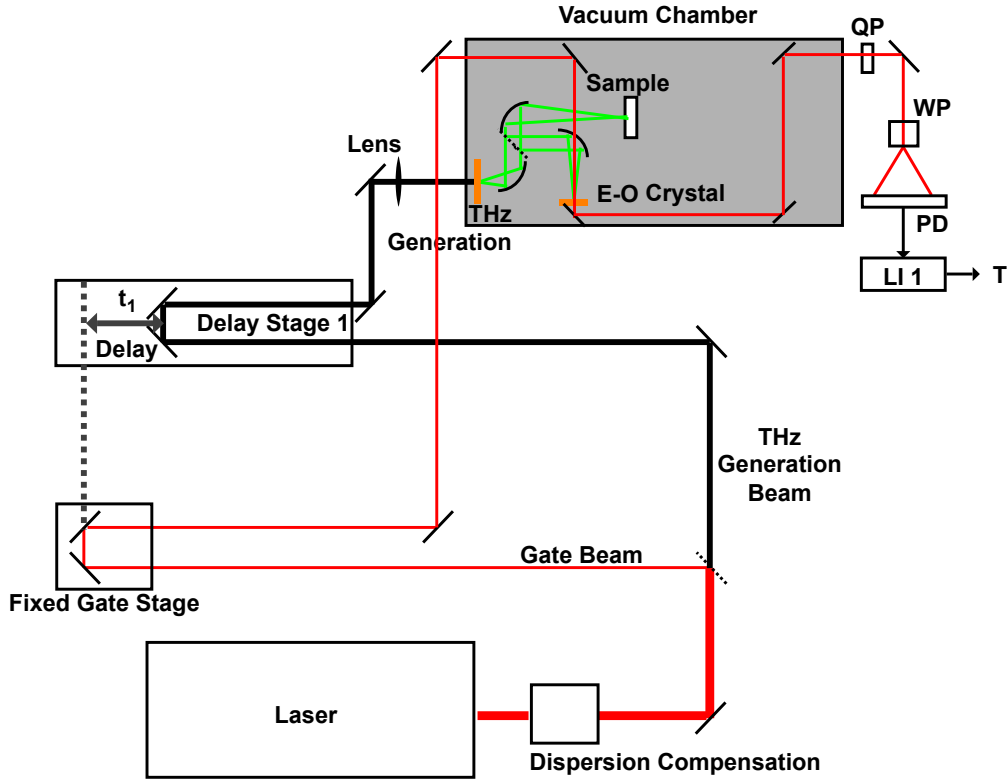


Figure 3.4: **Schematic of a THz-time domain spectroscopy experiment: normal reflection geometry** Beam paths before the sample are as in Fig. 3.2 except now the reflected THz radiation is collected, via a silicon beamsplitter inserted between the first and second off-axis parabolic mirrors (OAPs). A hole drilled in the third OAP allows the gate beam to hit the detection crystal co-linear with the THz pulse.

they are grown on an optically thick substrate. We typically achieve a resolution of 50 GHz although by careful measurement of oscillations in the time domain a 10 GHz resolution was achieved (see for example Fig. 4.9).

Details of all three THz-TDS systems used for the experiments presented in this thesis are given in Table 3.1.

3.1.2 Extracting the complex refractive index

Having measured the electric field of the THz pulse we now see how to extract sample properties. To determine the effect of interaction with the sample, we measure two spectra; one where the THz pulse has travelled through the sample and another, the reference, where it has not. We can express the vacuum reference electric field as the product of E_i , the electric field before the (empty) sample position and the phase associated with travelling through the vacuum (complex refractive index, $\tilde{n} = 1$) for a distance d equal to the thickness of the sample, as follows:

$$E_r(\omega) = E_i \exp \left[i \frac{\omega d}{c} \right] \quad (3.1)$$

When the sample is placed in the path of the THz beam we must include Fresnel transmission terms from the vacuum to the sample and then out of the sample into the vacuum which take the form $\tilde{t}_{ij} = 2\tilde{n}_i/(\tilde{n}_i + \tilde{n}_j)$, for light travelling from medium i to medium j . This holds true for a plane parallel plate sample at normal incidence. The phase change across the sample now contains information about the complex refractive index of the sample and we have a final Fabry-Perot (FP) term which accounts for all the internal reflections.

$$E_s(\omega) = \tilde{t}_{vs}\tilde{t}_{sv}E_i \exp \left[i \frac{\omega d}{c} \tilde{n}_s \right] \text{FP}_{vsv}(\omega) \quad (3.2)$$

The subscripts s and v indicate sample and vacuum, respectively. Explicitly, the Fabry-Perot term is a sum over P internal reflections, where the reflected amplitude at each interface is given by the Fresnel reflection coefficients $\tilde{r}_{ij} =$

$$(\tilde{n}_i - \tilde{n}_j)/(\tilde{n}_i + \tilde{n}_j)$$

$$\text{FP}_{ijk}(\omega) = \sum_{p=0}^P \tilde{r}_{jk} \tilde{r}_{ji} \exp \left[i \frac{\omega 2d}{c} \tilde{n}_j \right]^p \quad (3.3)$$

By dividing the electric fields with and without samples we can express the complex transmission, $\tilde{T}(\omega) = E_s/E_r$ in terms of the complex refractive index of the sample without making any assumptions about the nature of the sample.

$$\tilde{T}(\omega) = |\tilde{T}| \exp^{i\phi(\omega)} = \tilde{t}_{vs} \tilde{t}_{sv} \exp \left[i \frac{\omega d}{c} (\tilde{n} - 1) \right] \text{FP}_{vsv}(\omega) \quad (3.4)$$

Now we have an expression for the experimentally determined complex transmission which can always be solved numerically to extract the refractive index of the sample. Moreover, in two special cases we can make further progress and solve for \tilde{n} analytically.

Thick film limit

In the thick-film limit, which applies when consecutive reflections are well separated in time, one can collect data only before the first internal reflection meaning that $P = 0$ in Eqn. 3.3, and therefore $\text{FP} = 1$. With the further approximation that the frequency dependence of the refractive index is weak and so $\tilde{t}_{ij}(\tilde{n}) = t_{ij}(\tilde{n}(\omega = 0))$ permits us to express the complex refractive index, $\tilde{n} = n + i\kappa$ in terms of the real part of the refractive index, n , and the absorption coefficient, $\alpha = 2\omega\kappa/c$:

$$n(\omega) = 1 + \frac{c}{\omega d} \phi(\omega) \quad (3.5)$$

$$\alpha(\omega) = -\frac{2}{d} \ln \frac{|\tilde{T}(\omega)|}{\tilde{t}_{vs} \tilde{t}_{sv}} \quad (3.6)$$

This simplifies the analysis greatly and, where applicable, the thick-film approach is used. Large single crystal samples can be deliberately cut to a thickness such that this approximation is valid. As always, there is a trade-off between delay of the internal reflections and increased absorption as the thickness increases.

Differential measurement

Occasionally, unwanted information such as oscillations in refractive index due to sample birefringence or the tails of high lying phonon modes can obscure changes to the THz transmission that are under investigation. This can be alleviated by using a differential measurement technique. This is particularly useful for temperature or magnetic field dependence studies where, for example, \tilde{T} becomes $E(B)/E(B=0)$ and allows one to isolate small changes on a complicated background. Now we have a slightly different situation where both sample and reference have complex refractive indices as below:

$$\frac{E_s(\omega)}{E_i} = \tilde{t}_{vs}\tilde{t}_{sv} \exp\left[i\frac{\omega d}{c}\tilde{n}_s\right] \quad (3.7)$$

$$\frac{E_r(\omega)}{E_i} = \tilde{t}_{vr}\tilde{t}_{rv} \exp\left[i\frac{\omega d}{c}\tilde{n}_r\right] \quad (3.8)$$

By making the following approximations, we can still find an analytical solution for \tilde{n} in terms of \tilde{T} . We assume that the change in refractive index is small (i.e. $\Delta\tilde{n}_{rs} \ll \tilde{n}_r$) and therefore write the refractive index of the ‘sample’ as:

$$\tilde{n}_s = \tilde{n}_r + \Delta\tilde{n}_{rs} \quad (3.9)$$

$$\tilde{n}_s = (n + i\kappa) + (\delta n + i\delta\kappa) \quad (3.10)$$

Ignoring higher powers of $\Delta\tilde{n}$, this leads to very similar expressions for the change in refractive index and absorption coefficients.

$$\Delta n_{rs}(\omega) = \frac{c}{\omega d} \phi(\omega) \quad (3.11)$$

$$\Delta \alpha_{rs}(\omega) = -\frac{2}{d} \ln |\tilde{T}(\omega)| \quad (3.12)$$

The complex relative permittivity is related to the complex refractive index as follows, $\tilde{n} = \sqrt{\tilde{\varepsilon}}$, where $\tilde{\varepsilon} = \varepsilon_1 + i\varepsilon_2$, which yields the following expression for the real and imaginary parts of the permittivity:

$$\delta\varepsilon_1 = 2n\delta n - 2\kappa\delta\kappa \quad (3.13)$$

$$\delta\varepsilon_2 = 2n\kappa + 2\kappa\delta n \quad (3.14)$$

Note that in order to calculate the change in permittivity we require knowledge of the absolute refractive index of the reference sample.

3.1.3 Optical pump - THz probe spectroscopy

Pump probe spectroscopy refers generally to the detection of excited state properties of a system using synchronous short laser pulses. Hereafter I will use pump-probe to mean specifically 800 nm pump-THz probe spectroscopy. This is an ideal way to study the non-equilibrium dynamics of many systems, providing a time-resolved measurement of the response to photoexcitation. Time resolution is limited by the pulse duration, and total time range by the delay stage (usually far shorter than the laser repetition time which is the more fundamental limit for this experiment).

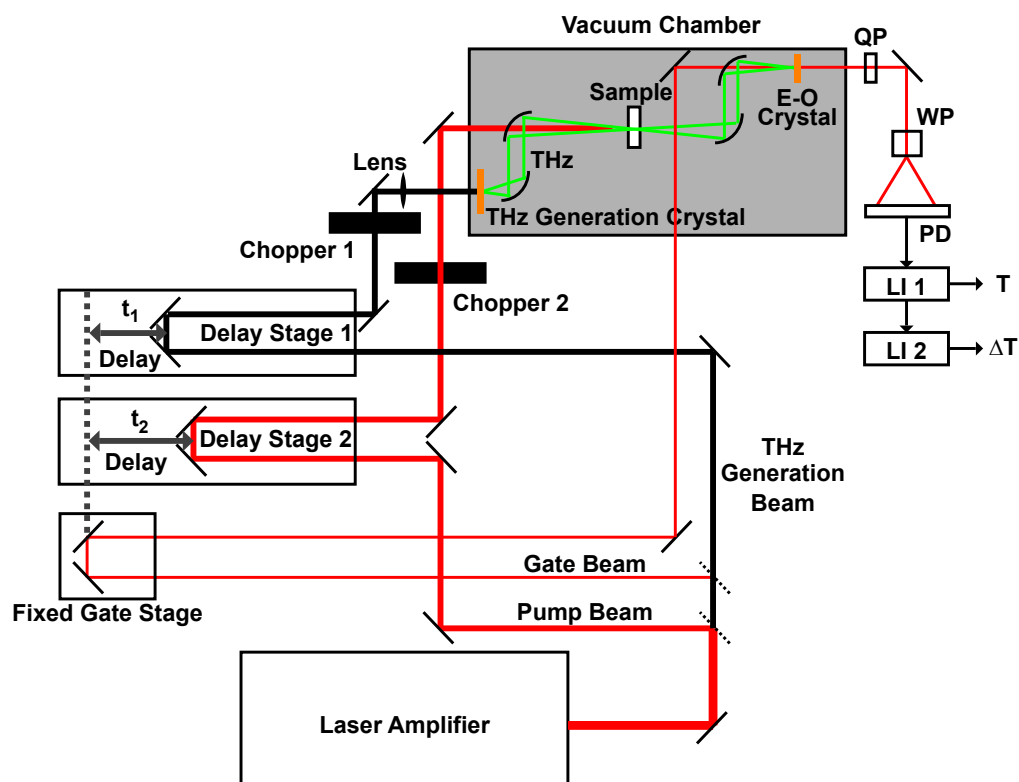


Figure 3.5: **Schematic of a THz-time domain spectroscopy experiment: 800 nm pump, THz probe** In order to perform OPTP measurements an extra beam splitter is used to draw off part of the IR laser beam to photoexcite the sample. A second delay stage is added so that spectral scans can now be taken at various times before and after the arrival of the pump pulse at the sample by moving Delay Stage 2.

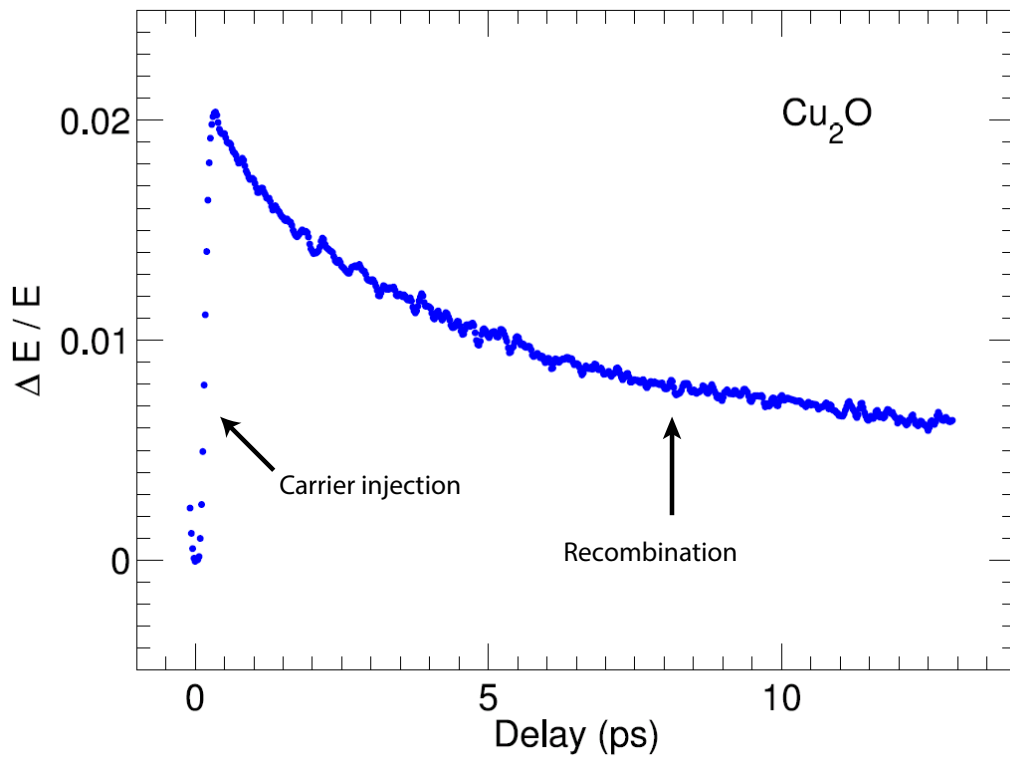


Figure 3.6: **An example of optical-pump, THz-probe spectroscopy** Pump probe signal on a sample of Cu_2O , a well-studied semiconductor with a band-gap of 2.14 eV.

In this experiment, THz transmission through the sample is measured as a function of arrival time relative to the optical pump pulse. This is either represented as a two-dimensional plot of transmission-frequency-pump delay or more commonly as the peak THz transmission vs pump-delay, typically producing data as shown in Fig. 3.6. Double lock-in detection is used to measure both \tilde{T} and $\Delta\tilde{T}$. An optical chopper (Chopper 1 in Fig. 3.5) is used to modulate the THz generation beam before it is incident on the electro-optic crystal, playing the same role as the electronic modulation of the PCS in the other THz systems. Chopper 1 typically runs at half the laser repetition rate in order to incorporate two full pulses into each on/off cycle. A second chopper is placed in the pump beam and runs at a lower rate with care taken to not use a frequency that is a factor of the first chopper. The output from lock-in 1 is proportional to the THz electric field amplitude and the output of the lock-in 2 is proportional to the pump induced change in transmission, $\Delta E = E_{\text{on}} - E_{\text{off}}$.

Typically the complex conductivity is defined as

$$\tilde{\epsilon}(\omega) = \tilde{\epsilon}_{\text{L}}(\omega) + \frac{i\tilde{\sigma}(\omega)}{\omega\epsilon_0} \quad (3.15)$$

in order to separate out the contribution to the permittivity from bound modes such as lattice vibrations and core electrons (ϵ_{L}) and mobile charges (σ) as can be derived from Maxwell's equations. Following a similar procedure to that in Section 3.1.2 results in the following equation for the photoconductivity of a thin film on a substrate:

$$\Delta\tilde{\sigma} = \left(\frac{1}{\tilde{T}} - 1\right) \left(\frac{1 + \tilde{n}_{\text{sub}}}{Z_0 d}\right) \quad (3.16)$$

Here, Z_0 is the impedance of free space, d is the thickness of the film and \tilde{n}_{sub} is the refractive index of the substrate. The equation is valid in the thin film limit,

where $n\omega d/c \ll 1$, provided that the free charge contribution to the conductivity dominates the bound charge. When using a double lock-in technique, one generally measures E and ΔE . This requires the substitution: $\tilde{T} = \tilde{E}_s/\tilde{E}_r = \Delta\tilde{E}/\tilde{E} + 1$

3.2 Fourier Transform Infrared Spectroscopy

A commercial Fourier transform infrared (FTIR) spectrometer (Bruker 80v) was used to extend the region of the electromagnetic spectrum investigated from the THz out to 1000 meV. Reflectivity spectra were collected at near-normal incidence ($\theta_i = 11^\circ$) over the temperature range 80–300 K using a cryostat insert (Oxford Instruments Microstat).

A broadband global light source was used in conjunction with two separate beamsplitter/detector combinations:

- MIR: KBr beamsplitter and DLaTGS detector (40–1000 meV)
- FIR: Si beamsplitter and DTGS detector (10–90 meV)

Cryostat windows made of KRS-5 were used for the temperature dependent study along with the MIR configuration to give a limited bandwidth but high transmission in order to focus on a particular region of the spectrum.

Infrared reflectivity data analysis was performed using the RefFit software package, by constructing an expression for the relative permittivity of the sample, calculating the reflectivity and then fitting to the experimental reflectivity using a least-squares Levenberg-Marquardt algorithm [105].

3.3 Raman Spectroscopy

Raman spectroscopy is a well established experimental technique and excellent commercial spectrometers are available. The principle is based on inelastic (Raman) scattering whereby light incident on a material interacts with molecular or lattice vibrations as it is scattered. The change in energy of the scattered light (the Raman shift) is equal to the energy of the vibrational mode. For a particular vibrational mode to be Raman-active it must change the polarisability of the molecule. The polarisability and therefore the selection rules for vibrational modes can be determined from the symmetry of the scattering substance. The development of Raman spectroscopy and the physics behind the experiments and selection rules are well covered in various textbooks, for example Refs. [106; 107].

Raman spectroscopy was performed on a commercial Raman microscope (Renishaw inVia Reflex). A HeNe laser ($\lambda = 633 \text{ nm}$) was focussed onto the sample surface through a wide-angle 50x objective lens in order to measure the Raman signal in the energy range 25–400 meV in a backscattering geometry. A liquid-N₂-cooled temperature-control sample stage (Linkham THM S600) was used in order to access the temperature range 90–300 K.

Phonon energies, linewidths, and intensities were extracted by fitting Lorentzian oscillators to the Raman intensity after removing the photoluminescence background [108].

Chapter 4

Cupric Oxide: electromagnons in a high temperature induced multiferroic

Terahertz time-domain spectroscopy reveals that intersublattice exchange in the improper multiferroic cupric oxide (CuO) creates electromagnons at substantially elevated temperatures (213 K–230 K). Dynamic magnetoelectric coupling can therefore be achieved in materials, such as CuO, that exhibit minimal static cross-coupling. The electromagnon strength and energy track the static polarisation, highlighting the importance of the underlying cycloidal spin structure. Polarised neutron scattering and terahertz spectroscopy identify a magnon in the antiferromagnetic ground state, with a temperature dependence that suggests a significant role for biquadratic exchange. Previously, electromagnons had been discovered at low temperature (<70 K) and predominantly in rare-earth compounds such as $RMnO_3$ and RMn_2O_5 , as reported in Chapter 1.

In this chapter, I introduce CuO in Section 4.1 before describing sample

preparation in Section 4.2. The experimental results begin with a room temperature characterisation of the samples in Section 4.3, followed by the temperature dependence of the absorption coefficient in Section 4.4. Analysis of the electromagnon (Section 4.5) and magnon (Section 4.6) excitations precedes a discussion of an optical pump THz probe experiment in Section 4.7. Finally, the chapter is summarised in Section 4.8.

All of the experimental results presented in this chapter are my own, except for the inelastic neutron scattering data shown in Fig. 4.9(b), which was taken by Stephen Gaw, Eliza Hétroy-Wheeler and Andrew Boothroyd.

4.1 An introduction to CuO

Exceptionally among the $3d$ -transition metal monoxides, cupric oxide (CuO) is a multiferroic with magnetically-induced ferroelectricity [109]. Neutron diffraction studies have clarified the magnetic phases of CuO [110; 111]. At low temperatures there is a commensurate, collinear antiferromagnetic phase (AF1) with two Cu^{2+} sub-lattices, on which spins are oriented parallel or anti-parallel to $[010]$, as pictured in Fig. 4.1. The nearest-neighbour exchange interactions responsible for the AF1 ground state are as follows (in the numbering convention of Ref. [112]). The strongest exchange, J_1 , is antiferromagnetic (AFM) and occurs along spin chains in the $[10\bar{1}]$ direction (Fig. 4.1). Weaker ferromagnetic (FM) coupling exists between chains on the same sublattice in the $[101]$ and $[010]$ directions, given by J_2 and J_7 respectively [113].

Between 213 K and 230 K (AF2 phase) the spins on one sub-lattice rotate into the ac plane [110; 111; 114], as pictured in Fig. 4.1(b), and an in-

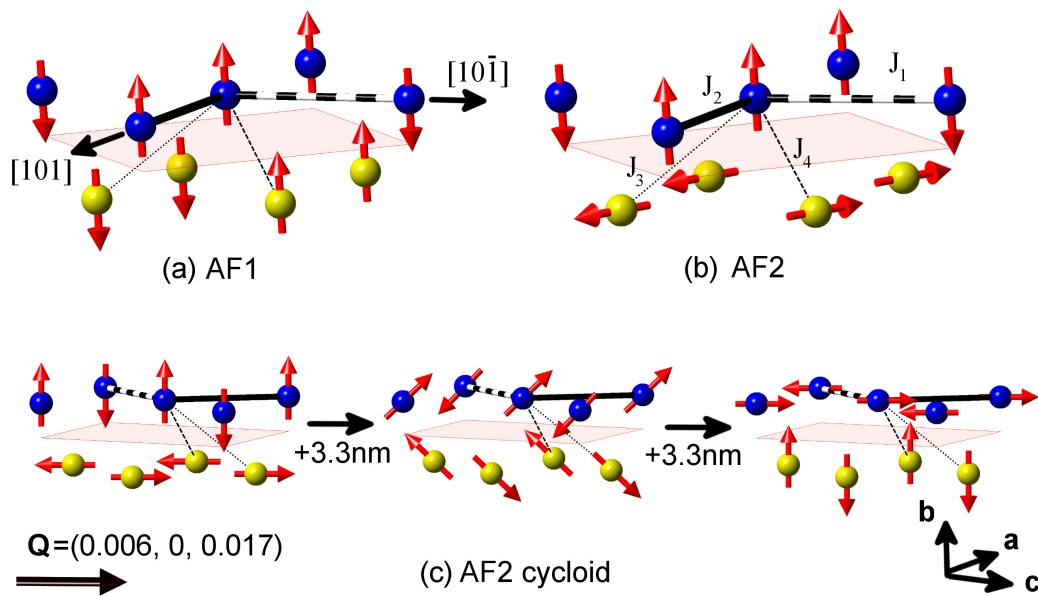


Figure 4.1: **Local spin structure in CuO** (a) In the AF1 phase, below 213 K, spins lay in the $\pm b$ -direction. (b) In the AF2 phase (213 K–230 K) spins on one Cu sublattice re-orient into the ac plane. The two different Cu sublattices are shown in blue and yellow, while the shaded area indicates the ac -plane. The exchange constant J_1 in the $[10\bar{1}]$ direction creates antiferromagnetic order, while in the $[101]$ direction J_2 is ferromagnetic. J_3 and J_4 describe the exchange interaction between sublattices. (c) Incommensurate AF2 spin structure for three unit cells along the magnetic modulation vector $\mathbf{Q} = (0.006, 0, 0.017)$. Spins rotate in the plane containing \mathbf{b} and $v = 0.506\mathbf{a}^* + 1.517\mathbf{c}^*$. [110; 111]

commensurate spin spiral structure is formed with magnetic modulation vector $\mathbf{Q}=(0.006,0,0.017)$. The incommensurate structure is essentially a cycloid, with a small proper screw component, and is visualised along \mathbf{Q} in Fig. 4.1(c). This phase exhibits a static electric polarisation $P_b \sim 100 \mu\text{Cm}^{-2}$ along b [1; 109; 115], the origin of which has been discussed in the context of weakly-frustrated intersub-lattice spin interactions [112], magnetic degeneracy and the spin-orbit interaction [116], and cross-coupled AFM order parameters [117]. While CuO exhibits ferroelectric hysteresis loops [109] and chiral magnetic domains that can be switched electrically [1], no substantial uniform static magnetoelectric coupling has been found in polycrystalline CuO up to 7 T [115], and the AF2 phase appears to be stable to at least 16 T [118].

Magnetic susceptibility and low-frequency dielectric constant data measured by Kimura *et al.* are presented in Fig. 4.2. Step changes in the magnetic susceptibility can be seen for all crystal axes at T_{N1} and more subtle changes in the slope at T_{N2} . The divergence in the permittivity at the onset of static polarisation, P_S , is a characteristic of ferroelectric materials [7]. This occurs along ϵ_b in CuO as this is the direction of P_S . A much smaller step-like change is seen at T_{N1} when P_S disappears at the onset of collinear antiferromagnetic ordering (inset of Fig. 4.2(b)). From the THz measurements, I report changes to ϵ_{101} and $\epsilon_{10\bar{1}}$ in Fig. 4.8. The small step-like change in ϵ_{101} is accounted for by the spectral weight transferred to the electromagnon.

The properties of CuO have been examined by additional techniques. Second harmonic generation spectroscopy experiments have shown that multiferroic domains are isotropically distributed throughout CuO with a lateral size of around $10 \mu\text{m}$ [119]. Intriguingly, hydrostatic pressure has been suggested to broaden the temperature width of the multiferroic phase past room temperature via den-

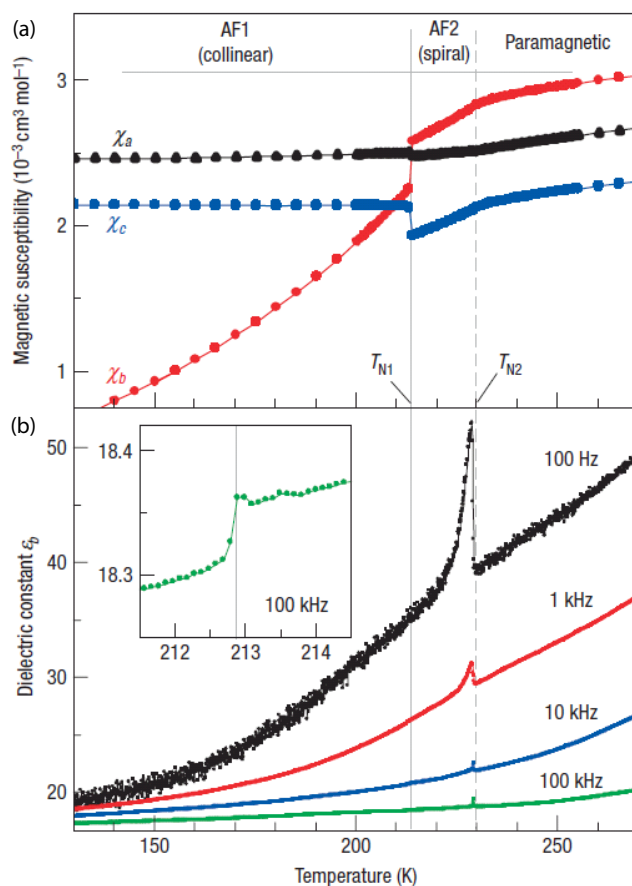


Figure 4.2: **Dielectric anomalies at magnetic phase transitions in CuO**
 (a) Magnetic susceptibility measured along the reciprocal lattice directions as a function of temperature. (b) Low frequency dielectric constant measured along the b -axis at selected frequencies. The inset shows a magnified view of ϵ_b at 100 kHz close to T_{N1} . Reproduced from Ref. [109].

sity functional theory calculations [120]. Ultrasonic velocity experiments have revealed a third magnetically ordered phase, stable between 229.3 K and 230 K, in which spins in one Cu sublattice order collinearly whereas those on the other sublattice remain disordered [118].

In this chapter I report that cupric oxide exhibits a sizeable dynamic magnetoelectric response. Terahertz time-domain spectroscopy (THz-TDS) uncovered an electromagnon excitation linked to the multiferroic phase, at the highest temperature reported to date for a magnetically-induced ferroelectric. Insights into the relevant microscopic interactions are gained by examining THz spectra in both the non-polar antiferromagnetic state and the polar multiferroic phase, and emphasise the importance of biquadratic exchange and intersublattice spin interactions in CuO.

4.2 Sample preparation

Single crystals of cupric oxide (monoclinic, space group $C2/c$ [121]) were grown by Dharmalingam Prabhakaran in Oxford using the optical float zone method [122]. The room temperature unit cell parameters were measured as: $a = 4.68 \text{ \AA}$, $b = 3.43 \text{ \AA}$, $c = 5.13 \text{ \AA}$, $\alpha = 90^\circ$, $\beta = 99.48^\circ$, and $\gamma = 90^\circ$ by powder X-ray diffraction. Details of the measurement are given in Section 5.2. The results are in good agreement with the literature [121]. The boule was oriented by X-ray Laue diffraction using the software package QLaue [123] to match experimental and calculated diffraction patterns. Flat, plate-like samples were cut and polished with the following in-plane crystallographic directions: (101) and (010) ; (101) and $(10\bar{1})$; (101) and $(11\bar{1})$. A diamond cutting wheel was used with ethanol as a cutting fluid. The samples were polished to $6 \mu\text{m}$ surface roughness using Pad-K

polishing pads and alumina powder. High resolution $\omega - 2\theta$ X-ray scans confirmed that samples were single crystals. SQUID measurements of the magnetic susceptibility were in agreement with results in the literature [1; 109].

4.3 Room temperature characterisation

Monoclinic CuO is a biaxially birefringent material, with a dielectric tensor ϵ_{ij} that consists of a scalar term $\epsilon_y = \epsilon_b$ along [010] and a matrix term $\epsilon_{ac} = \begin{pmatrix} \epsilon_{xx} & \epsilon_{xz} \\ \epsilon_{zx} & \epsilon_{zz} \end{pmatrix}$ in the ac -plane when expressed in a Cartesian co-ordinate system [124] with $x \parallel a$, $y \parallel b$, $z \parallel c^*$. A combination of transmission and reflection geometry THz-TDS was used to determine the complex refractive index $\tilde{n}_{ij} = \sqrt{\epsilon_{ij}\mu_{ij}}$ at room temperature in the paramagnetic insulating phase ($\mu_{ij} = 1$) over the energy range 0.8-23 meV (0.2-5.5 THz), as reported in Fig. 4.3. A variety of crystal orientations were examined. The birefringence of CuO is largest between [010] and the ac -plane, and can be witnessed directly in the time-domain in Fig. 4.3(a) at various sample azimuthal angles ϕ , where $\phi = 0$ corresponds to [101]. The real part of the refractive index is reported in Fig. 4.3(b) and the absorption in Fig. 4.3(c). The data on the left (right) were taken in transmission (reflection), allowing us to characterise the lowest transverse optical phonon modes for $E_{[101]}$ and $E_{[010]}$. The A_u^1 mode is at 21.1 meV (5.1 THz), and is driven by $E_{[010]}$, while an electric field in the ac plane excites the B_u^1 mode at 19.0 meV (4.6 THz) [124; 125]. Here the superscripts label the normal modes.

The [101], $[10\bar{1}]$ and [010] directions are optical axes [124], and at intermediate ϕ time-domain components are visible for each axis [Fig. 4.3(a)]. A misorientation of the sample of $\phi \sim 10^\circ$ can create spectral artefacts in the absorption coefficient α when calculated using a vacuum reference. In the subsequent anal-

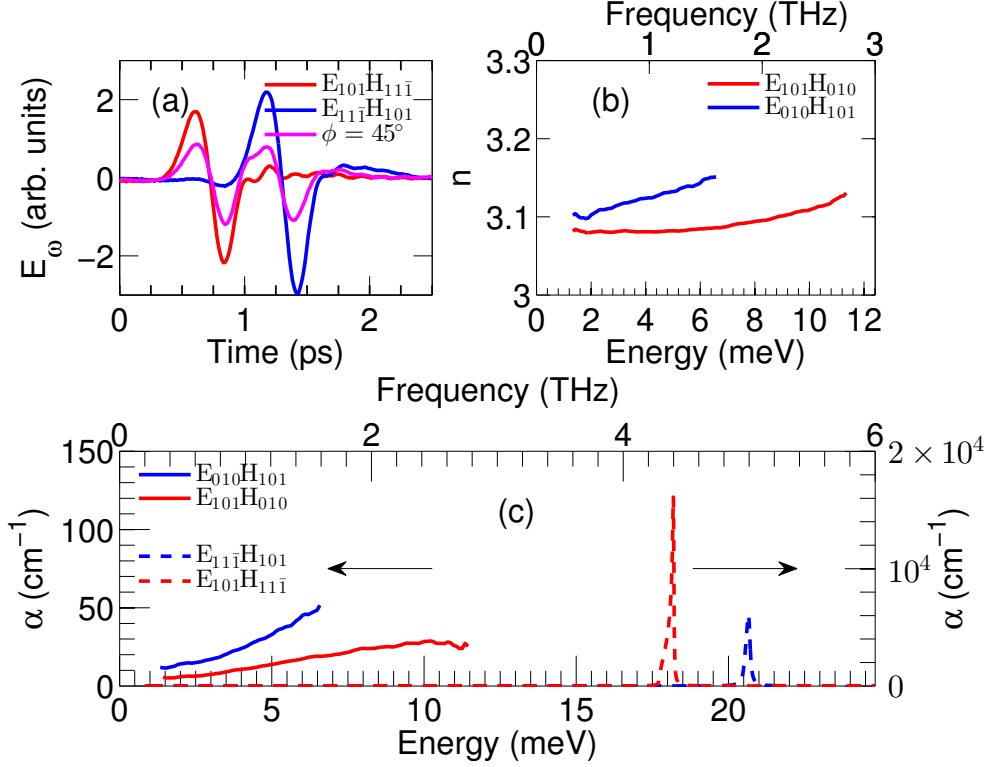


Figure 4.3: **THz dielectric response of CuO at room temperature** (a) The transmitted THz electric field in the time-domain shows the sample's birefringence: when E_ω is aligned with one of the optical axes a single cycle pulse is visible, whereas two pulses arise when E_ω has equal components along each of fast and slow axes ($\phi = 45^\circ$). (b) Real part of the refractive index shown for E_ω in the ac plane (red) and along the b -axis (blue). (c) Complementary absorption data from transmission (left) and reflection (right) measurements.

ysis we therefore report the absorption change $\Delta\alpha$ relative to the AF1 phase or the paramagnetic phase. This also alleviates the influence of absorption created by the A_u^3 mode at 51.3 meV (12.4 THz) [124], which dominates the absorption below 12 meV for $E_{[010]}$ owing to its substantial linewidth (maximum 7.7 meV or 1.9 THz), as demonstrated in Fig. 4.4.

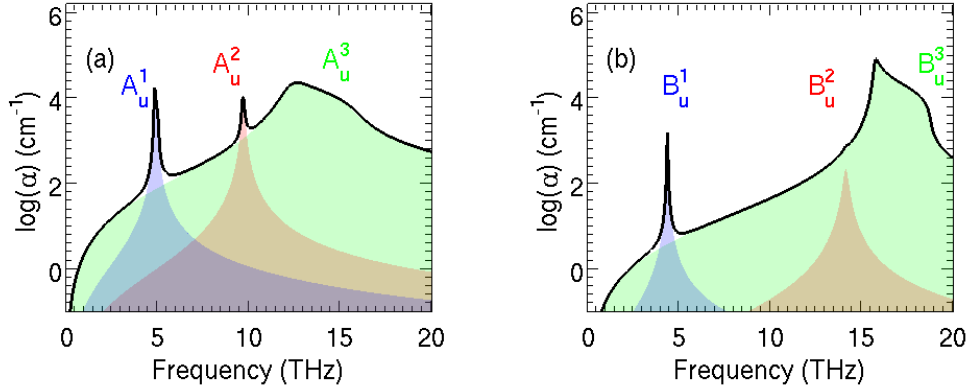


Figure 4.4: **Phonon mode contributions to absorption of CuO at room temperature** (a) The contribution from the A_u^1 , A_u^2 , and A_u^3 modes are shaded in blue, red and green, while the total absorption coefficient is given by the black line. These modes are active when the electric field E_ω is along [010]. (b) Similarly for $E_\omega \parallel [101]$, the contribution from the B_u^1 , B_u^2 , and B_u^3 modes are shaded in blue, red and green, while the total absorption coefficient is given by the black line. Graphs are calculated from the model and parameters given in Ref. [124].

4.3.1 Contribution of phonons to absorption coefficient

In order to identify the dominant contribution to the absorption in the THz frequency range (<3 THz or <12 meV) we show in Fig. 4.4 the absorption coefficient calculated for each mode independently. Here, room temperature parameters taken from a Fourier-transform infrared spectroscopy study [124] were used. The blue, red and green shaded areas show the contribution from the 1st, 2nd and 3rd IR-active phonon modes, while the total absorption coefficient α is shown by the black line. Note the logarithmic y -axis scale. Fig. 4.4(a) shows the case with the electric field E_ω along the b -direction, while Fig. 4.4(b) illustrates absorption for E_ω parallel to [101]. For both polarisations of E_ω the dominant absorption in the THz range arises from the highest IR-active mode, either A_u^3 or B_u^3 .

4.4 Dynamic magneto-electric response

To examine the THz response of CuO in the non-polar AF1 and polar AF2 phases the relative absorption $\Delta\alpha(T) = \alpha(T) - \alpha(T_0)$ is shown for a variety of E_ω and H_ω orientations in Fig. 4.5. The absorption relative to $T_0 = 200$ K is shown in Fig. 4.5(a) for $E_{[101]}$ with either $H_{[010]}$ or $H_{[10\bar{1}]}$. Representative temperatures T chosen were 212 K (AF1 phase), 216 K (AF2 phase) and 246 K, in the paramagnetic (PM) phase. A significant absorption for $E_{[101]}$ ($\Delta\alpha = 4 - 10 \text{ cm}^{-1}$) is present in the multiferroic AF2 phase, centered at 2.9 meV (0.7 THz), with linewidth ~ 2 meV (0.5 THz), and which is not present in the AF1 and PM phases. This mode is present irrespective of the direction of the magnetic field of the THz radiation, $H_{[010]}$ or $H_{[10\bar{1}]}$. In contrast, no such resonance is observed when the electric field is oriented along $[010]$ or $[10\bar{1}]$ [Fig. 4.5(b)]. Therefore this mode is an electric-dipole active magnon – an electromagnon – driven by $E_{[101]}$. The maximum value of $\Delta\alpha$ varies somewhat between samples, suggesting a possible influence of crystal alignment or of sampling multiple domains. For reference, the absolute absorption coefficient α is reported in Supplementary Fig. 2(a).

The relative absorption coefficient for $H_{[101]}$ (with $E_{[010]}$ and $E_{[10\bar{1}]}$) are presented in Fig. 4.5(b), where a reference at $T_0 = 246$ K was used for all data. This highlights a weak, narrow absorption feature in the AF1 phase more clearly. At $T = 200$ K an enhanced absorption at 5.0 meV (1.2 THz) is clearly visible for $E_{[10\bar{1}]}$, while for $E_{[010]}$ this resonance appears as a shoulder superimposed upon a decrease in $\Delta\alpha$ created by the broad A_g^3 phonon mode [124]. The resonance loses oscillator strength rapidly at the AF1/AF2 phase boundary, where spins on one sub-lattice rotate to lie in the ac -plane, and is weakly visible at 4 meV (0.97 THz) at 216 K (green, solid line). It can be identified as a pure spin-wave resonance (a

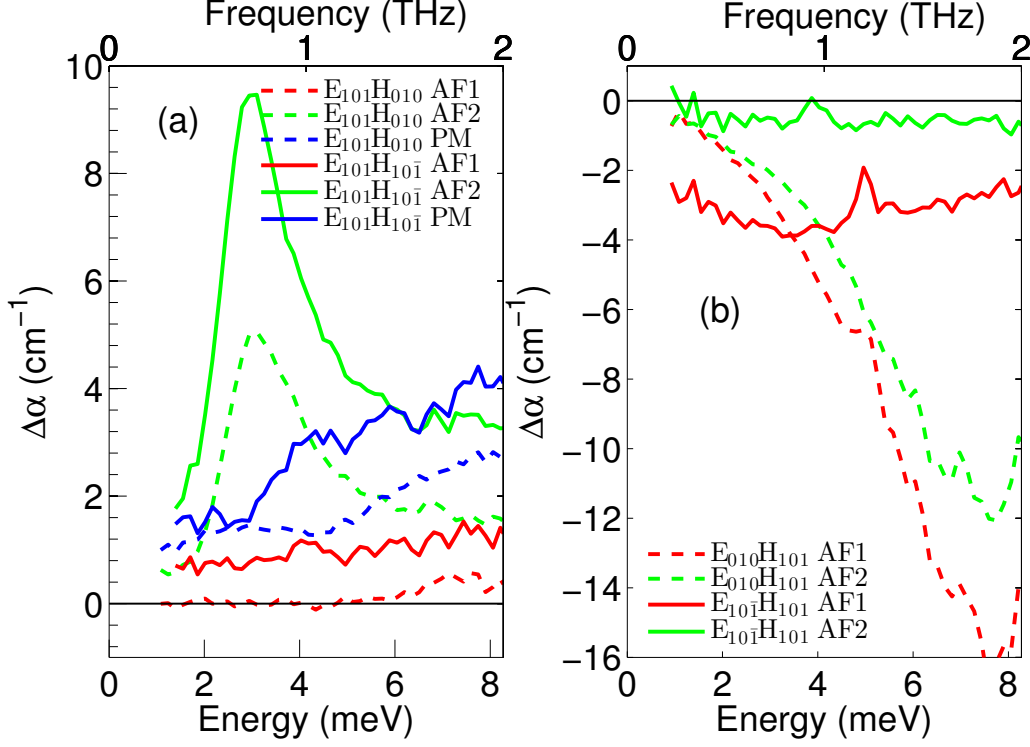


Figure 4.5: **Relative THz absorption spectra of CuO in the AF1, AF2 and PM phases** (a) Spectra for $E_w \parallel (101)$ with H_w along $(10\bar{1})$ (solid lines) and (010) (dashed lines) show a strong absorption at 2.9 meV (0.7 THz) in the AF2 phase (216 K) only. (b) Complementary spectra with $H_w \parallel (101)$ and E_w along $(10\bar{1})$ (solid lines) and (010) (dashed lines) show a weaker absorption at 5.0 meV (1.2 THz) in the AF1 phase (200 K) and at 4 meV (0.97 THz) in the AF2 phase.

magnon) with minimal spin-lattice coupling because: (i) it is present in the AF1 phase, (ii) it is present for $H_{[101]}$ regardless of the direction of E , and (iii) it has weaker spectral weight and sharper linewidth (< 0.08 meV at 10 K, ~ 0.4 meV at 216 K) in comparison to the electromagnon (~ 1.2 meV at 213 K). Magnon resonances are typically observed at THz frequencies in oxides and fluorides with AFM nearest neighbour coupling, while for materials with FM coupling they lie in the GHz range [126; 127]. CuO exhibits both AFM (J_1 along $[10\bar{1}]$) and FM (J_2 along $[101]$ and J_7 along $[010]$) nearest-neighbour coupling in its low-temperature phase.

4.5 Electromagnon

In order to elucidate the nature of the electromagnon excitation ($E_{[101]}$) we present in Fig. 4.6(a) $\Delta\alpha$ up to 10.3 meV (2.5 THz) in the temperature range 210–235 K. The electromagnon appears rapidly (within 0.3 K) at the AF1/AF2 phase transition, and consists of a strong peak at 3 meV and a weaker shoulder from 4–6 meV. The static polarisation $P_{[010]}$ was obtained from pyroelectric current measurements in the [010] direction (sample with [101] and $[10\bar{1}]$ crystal axes in the plane) [1], and is shown in Fig. 4.6(b). The excitation energy [Fig. 4.6(c)] and absorption strength [Fig. 4.6(d)] of the electromagnon closely track $P_{[010]}$, confirming this mode's assignment as an electromagnon, and suggesting that it is intimately linked to the cycloidal spin-structure of the AF2 phase.

In Fig. 4.7(b) a Drude-Lorentz oscillator fit to the electromagnon absorption is reported. The strength $\Delta\epsilon = 0.075$ of this electromagnon is weaker than the $E_\omega \parallel a$ electromagnons reported in TbMnO_3 ($\Delta\epsilon = 2$), thought to arise from the Heisenberg exchange mechanism,[37] and comparable to that assigned to an eigenmode of the spin cycloid ($\Delta\epsilon = 0.05$) [128]. Previously, the application of an optical sum rule has shown that electromagnons in RMn_2O_5 account for step-like changes in the static dielectric constant.[48] In Fig. 4.8 the change in dielectric constant is reported at 0.2 THz as obtained directly from THz-TDS, along with that obtained from a sum rule analysis. A significant step-like increase in dielectric constant along [101] at 213 K can be observed to result from electromagnons.

The *static* polarisation of rare earth perovskite manganites (e.g. RMnO_3 , where $R=\text{Tb, Dy}$) can be explained by the iDM interaction [15; 129], in which a spin cycloid breaks inversion symmetry. In contrast, the *dynamic* polarisation at THz frequencies is dominated by electromagnons [15; 37; 57; 58] created by

spin-lattice coupling, with the following term in the Hamiltonian:

$$\mathcal{H}_{\text{spin-phonon}} = - \sum_{i,j \in J_n} \sum_k \frac{\partial J_n}{\partial u_k} u_k \mathbf{S}_i \cdot \mathbf{S}_j. \quad (4.1)$$

As CuO is an improper multiferroic analogous to $RMnO_3$ and RMn_2O_5 , with comparable static polarisation and cycloidal spin structure [109], electromagnon models [84; 130] developed for these compounds may be expected to apply. An electric-field displaces ions a distance u_k along direction k , altering the bond angles along Cu–O–Cu superexchange pathways and thus J_n . The local magnetic field $\mathbf{H}_i^{\text{eff}}$ experienced by each spin \mathbf{S}_i is $\mathbf{H}_i^{\text{eff}} = -\partial\mathcal{H}/\partial\mathbf{S}_i$. The dynamical motion of spins can then be derived from the Landau-Lifshitz-Gilbert equation [84; 130], yielding

$$\frac{\partial\mathbf{S}_i}{\partial t} \propto \mathbf{S}_i \times \mathbf{S}_j \quad (4.2)$$

if damping is ignored. Electric fields can thus drive spin oscillations only if \mathbf{S}_i and \mathbf{S}_j are not parallel. For CuO, only the intersublattice superexchange terms J_3 and J_4 couple non-parallel spins, as depicted in Fig. 4.1(b). The electromagnon is only excited by $E_{[101]}$, i.e. along the ferromagnetic Cu-O chains, altering both intersublattice exchange pathways.

The contribution of additional interactions to the spin Hamiltonian can be understood by examining electromagnon spectra. Two or more absorption peaks are witnessed for $RMnO_3$ [15; 58]. The peak at higher energy can be understood by models including only Equation 4.1 [15; 37], while the addition of single-ion anisotropy (SIA) and biquadratic exchange (BE) terms is necessary to model the lower energy electromagnon [84]. In comparison, the electromagnon spectra in Figs. 4.5(a) and 4.6(a) exhibit more significant spectral weight at lower frequencies, suggesting that SIA or BE play significant roles in the multiferroic phase

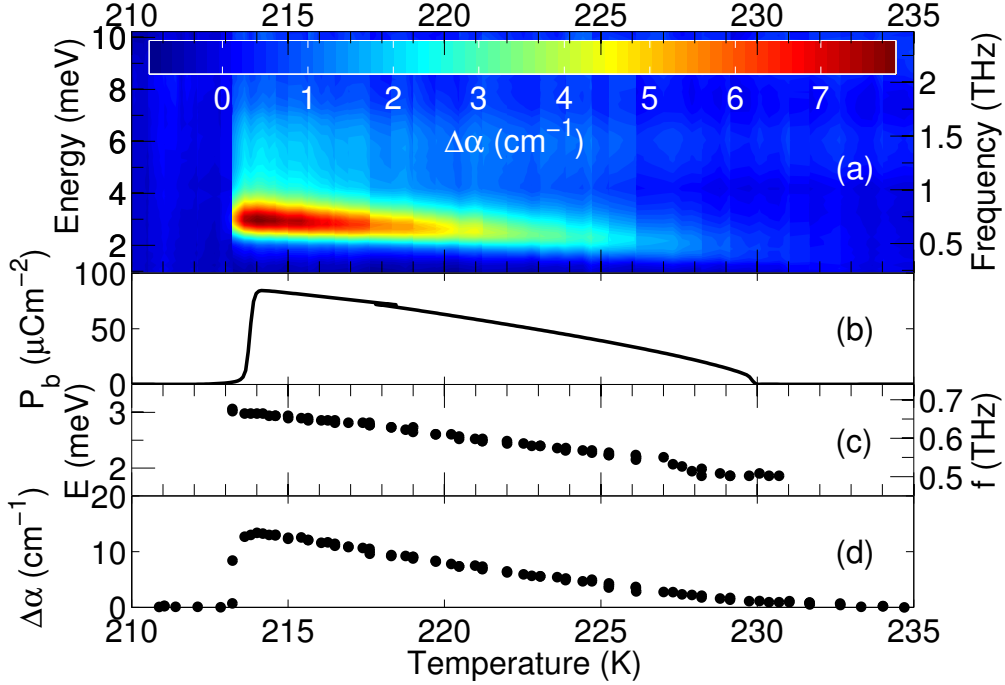


Figure 4.6: **Temperature dependence of THz absorption and static polarisation** (a) The evolution of the terahertz absorption coefficient $\Delta\alpha$ with temperature. The sharp onset of the electromagnon mode at the AF1/AF2 phase boundary is followed by a gradual decrease in mode frequency and strength to the AF2/PM boundary. (b) The static electric polarisation P_b (obtained from the pyroelectric current), (c) electromagnon energy and (d) absorption strength exhibit the same temperature dependence. The data in (b) is reproduced with permission from Ref. [1].

of CuO. The experimental $\Delta\alpha(T = 216\text{ K})$ can be fit using two Drude-Lorentz oscillators, as described in Fig. 4.7(b).

4.5.1 Electromagnon spectra and oscillator strength

The absolute absorption coefficient α for $E_\omega \parallel [101]$, $H_\omega \parallel [10\bar{1}]$, is reported in Fig. 4.7(a) at 200 K (AF1 phase) and 216 K (multiferroic AF2 phase). To allow a comparison of the electromagnon absorption reported here for CuO with those in other materials we report in Fig. 4.7(b) a fit to the change in absorption coefficient

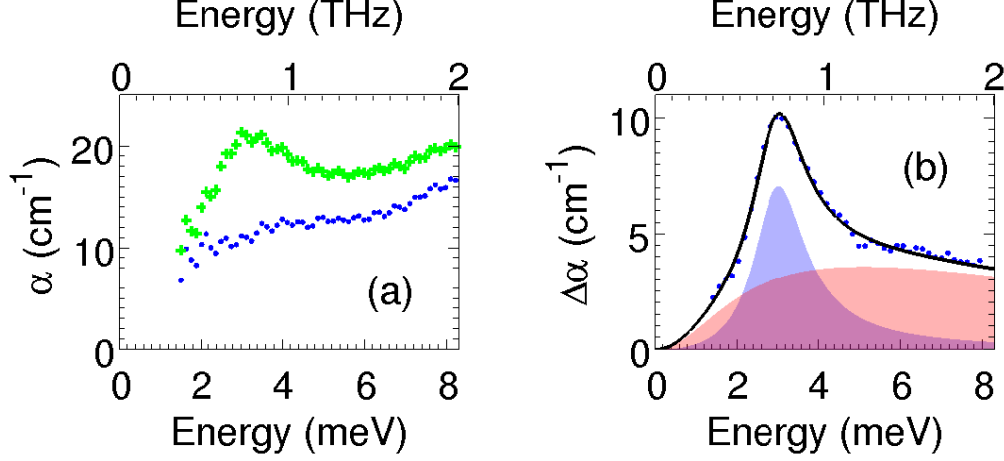


Figure 4.7: **Electromagnon absorption spectrum for CuO** (a) Absolute absorption $\alpha(T)$ at 200 K (blue points) and 216 K (green crosses). (b) A fit (black line) to electromagnon absorption spectra $\Delta\alpha$ (blue points) consisting of two oscillators (shaded blue and red areas), as described in 4.5.1.

$\Delta\alpha$. A Drude-Lorentz oscillator was used for this model, with a temperature-induced change in dielectric function $\Delta\epsilon(\omega)$ between temperatures T_2 and T_1 given by:

$$\Delta\epsilon(\omega) = \epsilon(\omega, T_2) - \epsilon(\omega, T_1) = \frac{\Delta\epsilon_a \cdot \omega_a^2}{\omega_a^2 - \omega^2 - i\omega\gamma_a} + \frac{\Delta\epsilon_b \cdot \omega_b^2}{\omega_b^2 - \omega^2 - i\omega\gamma_b} \quad (4.3)$$

The change in absorption coefficient was then calculated from $\Delta\epsilon(\omega)$. Two oscillators, centred at $\omega_a/2\pi = 0.73$ THz and $\omega_b/2\pi = 1.23$ THz provide a good fit to the experimental data, with $\gamma_{1,2} = 2.4$ THz, 22 THz and oscillator strength $\Delta\epsilon_{a,b} = 0.075, 0.12$. In comparison, $\Delta\epsilon \sim 2$ for the electromagnons in TbMnO_3 ($E_\omega \parallel a$, which are thought to arise from the Heisenberg exchange mechanism [37]. A weaker electric-dipole active electromagnon ($\Delta\epsilon \sim 0.05$) at 21 cm^{-1} , thought to be an eigenmode of the spin cycloid structure, has also been identified[128] in TbMnO_3 with a different selection rule.

4.5.2 Static dielectric constant and spectral weight transfer

Previous studies of electromagnons in other improper ferroelectric multiferroics have highlighted the important link between the dynamic response and the static permittivity, often using sum rules similar to:

$$\epsilon_1(\omega = 0) = 1 + \frac{2}{\pi} \int_0^\infty \frac{\epsilon_2(\omega)}{\omega} d\omega \quad (4.4)$$

For instance, in $R\text{Mn}_2\text{O}_5$ (improper polarisation $P \parallel b$) electromagnon modes (selection rule $E_\omega \parallel b$) are thought to account for step-like changes in the static dielectric constant ϵ_b [48]. Restricting the spectral range of the integral in Equation 4.4 to a region of interest (e.g. across a particular phonon mode) allows the transfer of spectral weight between electromagnons and other modes to be studied.

Both temperature and external magnetic fields can destroy incommensurate magnetic states, creating non-polar AFM phases. For GdMnO_3 and DyMnO_3 spectral weight was found to shift from electromagnons to optical phonons on entering the AFM phase [44; 131]. In contrast, for TbMnO_3 the electromagnon spectral weight transferred to magnon modes when a magnetic field drove the system from the multiferroic state into the A-type AFM phase [132], although spectral weight transfer with low-frequency optical phonons has also been reported [133].

Motivated by these considerations we report in Fig. 4.8 the change in the real part of $\epsilon(\omega)$ at 0.2 THz, the low-frequency limit of our experiment. Terahertz time-domain spectroscopy directly measures the complex refractive index (and therefore $\epsilon(\omega)$ assuming a purely electric response), without resort to the

Kramers-Kronig relations. A step-like increase in dielectric constant $\Delta\epsilon_s \sim 0.07$ can be observed at 213 K when $E_\omega \parallel [101]$ [blue circles in Fig. 4.8], but no change can be seen when $E_\omega \parallel [10\bar{1}]$ [red squares in Fig. 4.8]. In comparison, $\Delta\epsilon_s \sim 2$ for the electromagnons in TbMnO_3 ($E_\omega \parallel a$), which are thought to arise from the Heisenberg exchange mechanism [37]. A weaker electromagnon ($\Delta\epsilon_s \sim 0.05$) at 2.6 meV, thought to be an eigenmode of the spin cycloid structure, has also been identified in TbMnO_3 with a different selection rule [128].

The sum rule in Equation 4.4 allows the change in static dielectric constant with temperature, $\Delta\epsilon_s(T)$, to be written as:

$$\begin{aligned} \Delta\epsilon_s(T) = \epsilon_1(\omega = 0, T) - \epsilon_1(\omega = 0, T_0) &= \frac{2}{\pi} \int_0^\infty \frac{\epsilon_2(\omega', T) - \epsilon_2(\omega', T_0)}{\omega'} d\omega' \\ &= \frac{2}{\pi} \int_0^\infty \frac{\Delta\epsilon_2(\omega')}{\omega'} d\omega' \end{aligned} \quad (4.5)$$

The measured data for $\Delta\epsilon_2(\omega)$ was integrated over the experimental bandwidth (0.2 THz-2.5 THz), and are plotted as green crosses in Fig. 4.8. The sum rule prediction corresponds to a large percentage of the measured change in dielectric constant. Therefore the increased absorption associated with electromagnons accounts for a significant fraction of the change in dielectric constant. Since changes to the dielectric constant are linked to changes in ϵ_2 at all higher frequencies, the excess not accounted for by electromagnons may arise from modifications to the phonon modes.

4.6 Magnon

To examine the AF1 ground state of CuO we investigated the temperature dependence of the magnon ($H_{[101]}$) resonance, which redshifts with increasing tempera-

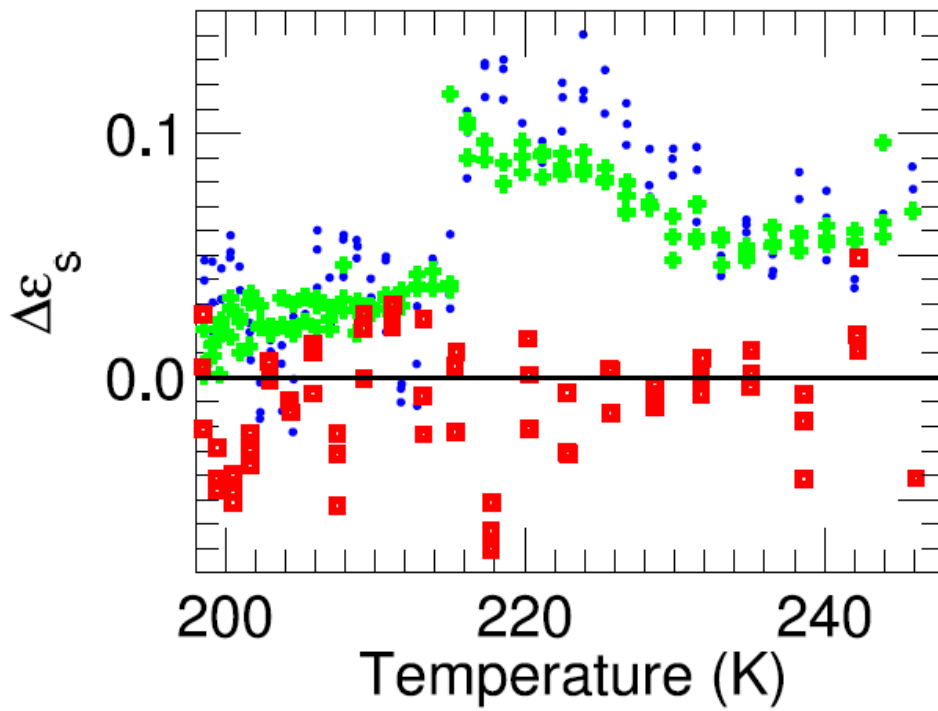


Figure 4.8: **Temperature dependence of the ‘static’ dielectric constant for CuO in the *ac*-plane from THz-TDS.** The measured real part of the dielectric function at 0.2 THz is shown relative to its value at 200 K [$\epsilon_1(0.2 \text{ THz}) = 9.2$]. Data are shown for $E_\omega \parallel [101]$ (blue circles), where the electromagnon is observed, and for $E_\omega \parallel [10\bar{1}]$ (red squares), where it is not. Green crosses show the predicted change in static dielectric constant for $E_\omega \parallel [101]$ from the sum rule in Equation 4.5.

ture, as indicated by the crosses in Fig. 4.9(a). Also shown is the electromagnon frequency (squares), which is reduced for a mixed spin-lattice mode with respect to the pure magnon frequency [50]. We constructed a phenomenological spin model for the magnon using a linear and biquadratic superexchange model [134] that was utilised recently to model the temperature dependence of the THz antiferromagnetic resonance in MnO [135].

Here we present a short summary of the derivation of Equation 4.7, which links the sublattice magnetisation σ to the ratio of temperature T to the Néel temperature, T/T_N . The reduced magnetisation σ is linked to the magnetisation M by $\sigma(T) = M/M(T=0)$. In this model the spin Hamiltonian is assumed to be of the form $J\mathbf{S}_a \cdot \mathbf{S}_b - j(\mathbf{S}_a \cdot \mathbf{S}_b)^2$ [37], and the exchange energy U per spin is taken to be $U = -\frac{1}{2} [2J(\sigma S)^2 + 2j(\sigma S)^4]$ [48]. Here we assume that the Cu^{2+} ions have spin $S=1/2$. The temperature T can be obtained from the following relation:

$$T = \frac{(\partial U / \partial \sigma)_T}{(\partial S^* / \partial \sigma)_T} \quad (4.6)$$

which can be derived from $F = U - TS^*$, where S^* is the entropy, and the condition $(\partial F / \partial \sigma)_T = 0$. Writing the partition function for a spin-1/2 particle in a magnetic field allows F, M, S^* and thus $(\partial S^* / \partial \sigma)_T$ to be determined. Using the result that $\sigma \rightarrow 0$ as $T \rightarrow T_N$ permits the reduced temperature to be written

$$\frac{T}{T_N} = \frac{\sigma}{\tanh^{-1} \sigma} \left[1 + \frac{\sigma^2 j}{2J} \right]. \quad (4.7)$$

The temperature dependence of the magnon frequency, assumed to be proportional to the sublattice magnetization [126], could therefore be calculated and compared with experiment. A ratio $j/J = 0.3$ produced an excellent accord with experiment, as evidenced by the solid line in Fig. 4.9(a). The cases with

zero ($j = 0$, dashed line) and stronger biquadratic exchange ($j/J = 0.6$, dash-dotted line) resulted in poorer agreement. Previous studies have suggested that biquadratic exchange may play an important role in determining the spin structure of CuO. By constructing a mean-field theory for weakly coupled AFM spin chains, Yablonskii showed that the inclusion of biquadratic exchange can stabilise the commensurate state at low temperature, and the incommensurate phase at elevated temperature [114; 136]. Recent variational calculations combined with Monte Carlo simulations [137] have also highlighted biquadratic exchange interactions as important in stabilising incommensurate magnetic states at finite temperature, as in CuO. The temperature dependence of the magnon frequency therefore provides experimental evidence consistent with biquadratic exchange, although alternative microscopic mechanisms may result in the same phenomenology. Note that the fit to the reduced temperature depends on j/J rather than J . Neutron scattering has determined J_1 to be between -75 meV and -80 meV, with $J_2 = 5$ meV and $J_7 = 3$ meV [113; 138]. Other measurements include $|J_1| = 77$ meV from susceptibility [139], and $|J_1| = 100 - 108$ meV from mid-infrared conductivity [140] and Raman spectra [141]. Recent DFT calculations have yielded values for J_1 ranging from -51 meV to -127 meV [112; 116].

The magnetic field dependence of the magnon resonance was investigated by applying a static field parallel to the b -axis of an ac -plane oriented sample, and probing $H_{[101]}$ with THz-TDS. As illustrated in Fig. 4.9 the magnon frequency increases quadratically with field in the range 0-7 T. This is consistent with high-frequency ESR measurements in fields up to 40 T [142]. The ESR data shows additional modes around 300 GHz associated with the collinear phase and the spin-flop transition at 10.2 T [142; 143].

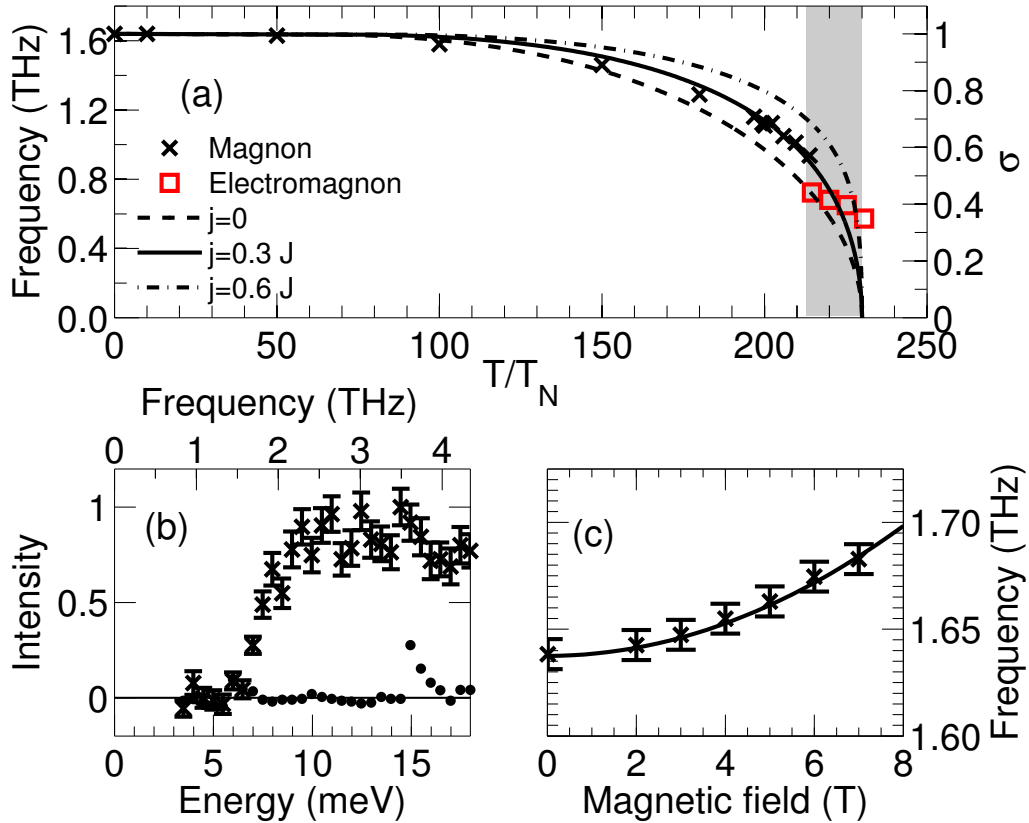


Figure 4.9: **Temperature and magnetic-field dependence of the magnon resonance** (a) The temperature dependence of the $H_{[101]}$ magnon mode (crosses) tracks the sub-lattice magnetization σ (lines) calculated from a phenomenological model described in the text. Good agreement is found for a biquadratic exchange ratio of $j/J = 0.3$ (solid line), rather than with $j = 0$ (dashed) or $j/J = 0.6$ (dash-dotted line). (b) Polarised inelastic neutron scattering spectra at 10 K show the separated transverse magnetic (crosses) and nuclear (points) scattering signal at $\mathbf{Q}=(-0.5,0,-1.5)$. A gap in the magnon spectrum at 7.75 meV correlates with the magnon resonance frequency in subplot (a). (c) The magnon frequency at 10 K (points) increases quadratically (line) with a static magnetic field along [010].

4.6.1 Polarised inelastic neutron scattering

Polarised neutron scattering was utilised to probe further the AF1 phase. The polarised neutron scattering experiments were performed by Stephen Gaw on the IN20 spectrometer, at the Institut Laue-Langevin in Grenoble, France. A single crystal, of mass 6.7 g and a crystal mosaic $< 2^\circ$ was aligned with $(h, 0, l)$ as the scattering plane. The monochromator and analyser used were both polarising Heusler (111) crystals and the measurements were taken at a fixed final wavevector of $k_f = 2.662 \text{ \AA}^{-1}$.

Polarisation analysis [144] was used to separate the magnetic and nuclear scattering contributions. In Fig. 4.9(b) magnetic (crosses) and nuclear (points) scattering spectra are reported for the AFM wavevector $\mathbf{Q} = (-0.5, 0, -1.5)$ at $T = 10 \text{ K}$. The magnetic scattering corresponds to spin fluctuations perpendicular to \mathbf{Q} in the ac -plane. A sharp gap for in-plane magnetic fluctuations at 7 meV correlates well with the magnon resonance observed with THz-TDS at 6.8 meV [1.64 THz , Fig. 4.9(a)], demonstrating that the magnon is linked to ac -plane spin fluctuations. There is no nuclear scattering until a low energy phonon mode at 15.5 meV , which derives from an acoustic branch [145].

4.7 Optical-pump THz-probe spectroscopy

January 2012 saw the publication of a report claiming that the AF2 phase of CuO could be stabilised relative to the AF1 phase by optical excitation at 1.55 eV [136]. The AF1-AF2 phase transition is driven by increasing spin disorder as the temperature rises. Alternatively, one can control spin disorder by above-band-gap optical excitation. CuO has a band-gap at 1.4 eV [146] allowing direct control of non-thermal spin-disorder by exciting electron transfer across the band gap. The

paper details a femtosecond time-resolved resonant X-ray scattering probe study of the effects of a 1.55 eV optical pump. Due to the first order nature of the AF1-AF2 phase transition in CuO, regions of both phases are present at temperatures close to the transition. The experiment was performed at 207 K, where diffraction peaks due to both AF1 and AF2 phases were present. A decrease in intensity of both peaks was observed on arrival of the pump pulse, with a greater relative decrease seen for the commensurate peak. This leads the authors to claim that the incommensurate state is stabilised by spin disorder.

To further test this claim a 1.55 eV pump, THz-probe experiment was performed at 207 K using a pump fluence of 50 mJcm^{-2} . This is comparable to the largest fluence used in the X-ray probe study (40 mJcm^{-2}). No step-like change was seen in the transmitted THz electric field at the arrival of the pump beam at $t = 0$ although a small offset is present in the data, shown in Fig. 4.10. This is consistent with a pump-induced heating of the sample, with a timescale $\tau_{\text{heating}} > \tau_{\text{THz}} \simeq 200 \mu\text{s}$ and $\tau_{\text{heating}} < \tau_{\text{pump}} \simeq 8 \text{ ms}$. See Fig. 3.5 for further details on τ_{pump} and τ_{THz} . If the AF2 phase were stabilised over the AF1 phase by the pump pulse then one might expect to see a strong change in the THz transmission due to activation of the electromagnon. That no step is seen implies that there is no long range stabilisation of the AF2 phase (at least not on scale larger than 52.8 nm , i.e. one cycloid wavelength).

4.8 Summary

In summary, the dynamic magnetoelectric response of the multiferroic CuO was investigated. An electromagnon excitation was discovered in the multiferroic phase (213–230 K), and was attributed to spin-lattice coupling between differ-

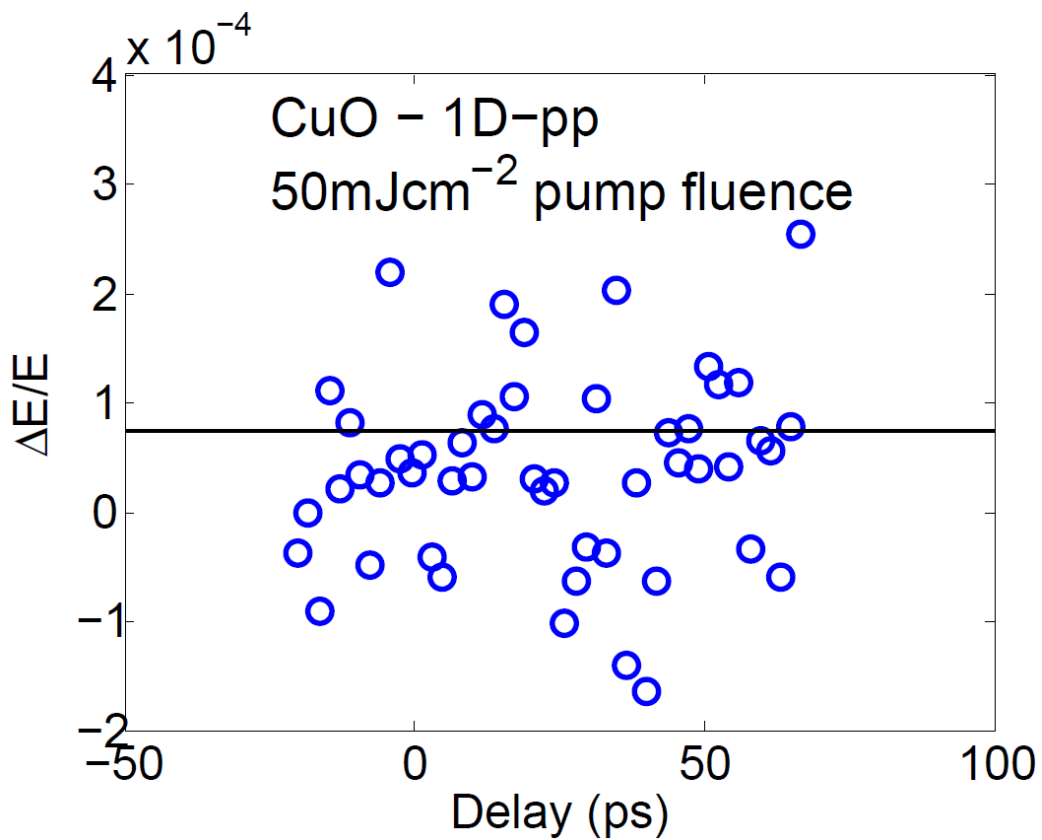


Figure 4.10: **Pump-induced change in the THz electric field** No signal was observed in CuO at 207 K under a pump fluence of 50 mJcm^{-2} , other than a small constant offset consistent with a change in α caused by the transient heating of the sample by the pump beam. For comparison the pump probe signal on Cu_2O in Fig. 3.6 has no offset and a clear time dependent photoconductivity.

ent Cu spin sublattices. The electromagnon spectrum, and temperature dependence of the magnon frequency, indicate that CuO exhibits a sizable magnetic anisotropy. The observation of electromagnons in an improper multiferroic at close to room temperature may create exciting new prospects for magnonic devices operating at THz frequencies. In the commensurate magnetic phase a magnon resonance observed via terahertz spectroscopy correlates with a gap in the in-plane magnetic scattering component from inelastic neutron scattering.

Chapter 5

Manipulating the multiferroic phase of CuO via Zn alloying

Terahertz time-domain spectroscopy was used to examine electromagnons in $\text{Cu}_{1-x}\text{Zn}_x\text{O}$ ($0 < x < 0.05$), a signature of dynamic magnetoelectric coupling. Zinc alloying was found to reduce the antiferromagnetic ordering temperature and widen the multiferroic phase, under the dual influences of spin dilution and a reduction in unit cell volume. The influence of Zn-substitution on lattice dynamics was elucidated by Raman and Fourier-transform spectroscopy. A pronounced softening and broadening of the A_u^3 phonon, active along the direction of ferroelectric polarisation, occurs at the collinear/non-collinear phase boundary in $\text{Cu}_{1-x}\text{Zn}_x\text{O}$, and indicates strong spin-phonon coupling in the multiferroic state. The commensurate antiferromagnetic phase also exhibits spin-phonon coupling, evidenced by a Raman-active mode associated with a magnetic modulation of a zone-folded acoustic phonon. While the phonon and magnon modes broaden and shift as a result of substitution-induced disorder, the electromagnon is relatively insensitive to disorder, increasing in energy without widening.

In this chapter I report an investigation into the multiferroic state of cupric oxide upon alloying with non-magnetic zinc ions. Terahertz time-domain spectroscopy revealed that the energy of the electromagnon excitations in $\text{Cu}_{1-x}\text{Zn}_x\text{O}$ increased upon alloying for $x \leq 0.05$. The presence of electromagnons in single crystal and polycrystalline samples indicated that the multiferroic phase was preserved. A greater reduction of $T_{\text{N}1}$ than $T_{\text{N}2}$ broadened the multiferroic state, which I discuss in the context of spin-dilution and substitution-induced lattice distortions. We further investigated spin-lattice coupling in $\text{Cu}_{1-x}\text{Zn}_x\text{O}$ by examining the principal phonon modes using a combination of Fourier transform infrared (FTIR) and Raman spectroscopy.

Growth details and a structural characterization are reported in Sec. 5.2. The magnon and electromagnon excitations of $\text{Cu}_{1-x}\text{Zn}_x\text{O}$ are discussed in Sec. 5.3, and the dynamic lattice response is detailed in Sec. 5.4. A discussion of the role of spin dilution in quasi-1D spin chains is provided in Sec. 5.5, before conclusions are drawn in Sec. 5.6.

5.1 Background: the influence of pressure or alloying

Electromagnons may permit novel THz optical components, such as chromatic filters, waveplates, or directionally dichroic filters [55]. Room temperature, tunable electromagnons (under readily accessible electric or magnetic fields) are therefore strongly desired. Increasing the ferroelectric ordering temperature $T_{\text{N}2}$ of CuO may provide a route to electromagnons at room temperature. While hydrostatic pressures may broaden the width of the multiferroic phase of CuO past room temperature [120], chemical pressure via substitution is a more attractive route

technologically. Moreover, it has been suggested that alloying with non-magnetic ions could itself cause a stabilisation of the multiferroic phase at higher temperatures [116].

Numerous studies have been made on polycrystalline samples of CuO alloyed with various ions, including heterovalent ions Li^+ [147; 148], Fe^{3+} [149] and Ga^{3+} [148] and homovalent ions Mn^{2+} [150], Fe^{2+} [151], Co^{2+} [152], Ni^{2+} [148; 149], and Zn^{2+} [148]. However none of these studies were made after the discovery in 2008 that the AF2 magnetic phase drives improper ferroelectricity [109]. In the studies that report changes in T_N as a function of alloy concentration, it is usually from magnetic susceptibility ($\chi(T)$) data on polycrystalline samples, where the changes at T_{N1} and T_{N2} are considerably broadened compared to single crystal samples.

5.2 Growth and characterisation

Single crystals of CuO and $\text{Cu}_{0.95}\text{Zn}_{0.05}\text{O}$ were prepared from high purity (> 99.999%) powders of CuO and ZnO. Cylindrical rods were sintered at 950 °C for three days under oxygen in an optical float-zone furnace [122]. Samples were cut from the boule and oriented by Laue diffraction, resulting in 1.3 mm thick single crystal samples with the following in-plane orientations and diameters ϕ : CuO with $\phi=1.8$ mm, (101) and (10 $\bar{1}$); CuO with $\phi=6$ mm, (101) and (010); $\text{Cu}_{0.95}\text{Zn}_{0.05}\text{O}$ with $\phi=2$ mm, (101) and (10 $\bar{1}$); $\text{Cu}_{0.95}\text{Zn}_{0.05}\text{O}$ with $\phi=3$ mm, (101) and (010). Polycrystalline samples were prepared with larger diameters ($\phi=8$ mm), and thickness 2 mm.

High resolution X-ray powder diffraction was used to examine the crystal structure at room temperature. Pieces of single crystal were ground to a fine

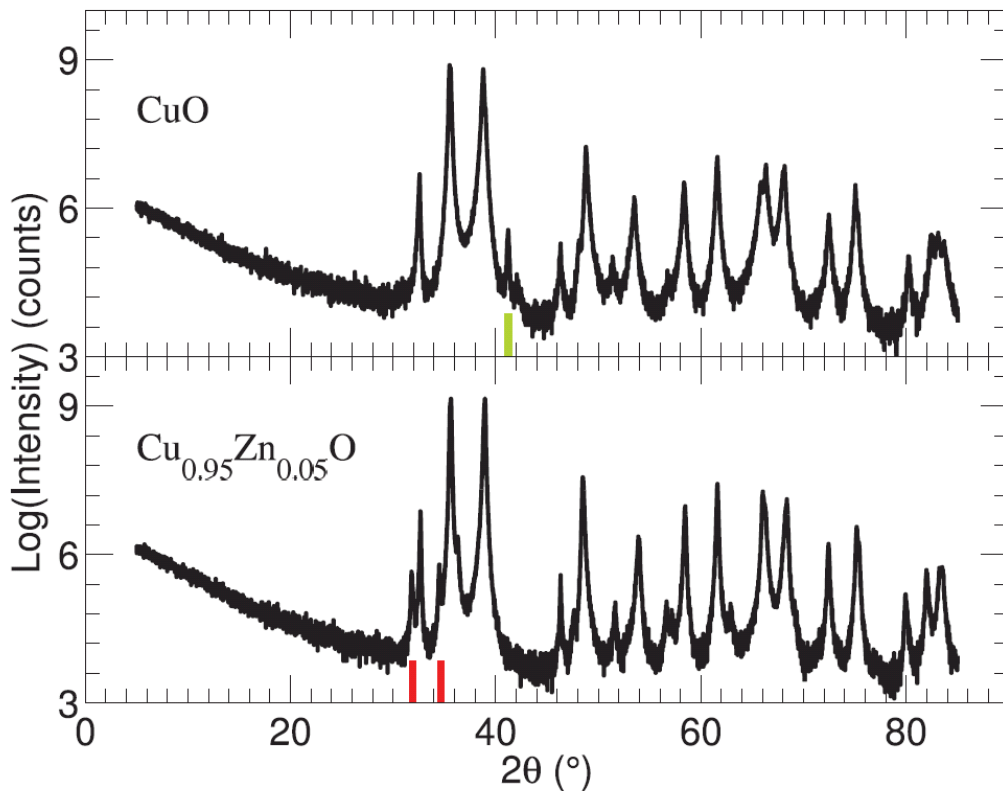


Figure 5.1: X-ray diffraction data on both CuO and Cu_{0.95}Zn_{0.05}O. Peaks not indexed by comparison to known diffraction peaks for CuO and extraneous peaks are shown by coloured lines. The two extra peaks in Cu_{0.95}Zn_{0.05}O are identified as ZnO peaks and show the presence of small unreacted amounts of this compound which is used in the growth of Cu_{1-x}Zn_xO. The green line identifies a single anomalous peak in CuO that is not due to any of the copper-oxide compounds (CuO, Cu₂O, Cu₄O₃ etc.) The peak is consistent with a small contamination of FeO.

Table 5.1: Summary of the Rietveld analysis of powder XRD on CuO and $\text{Cu}_{0.95}\text{Zn}_{0.05}\text{O}$, compared with data from Åsbrink and Norrby (first column of data) [121]. Experiments performed at 300 K.

	CuO 121	CuO	$\text{Cu}_{0.95}\text{Zn}_{0.05}\text{O}$	% Change on doping
a (Å)	4.6837	4.6835	4.71156	+ 0.68
b (Å)	3.4226	3.42766	3.40267	- 0.73
c (Å)	5.1288	5.13129	5.13081	- 0.01
β (°)	99.54	99.48	99.90	+ 0.42
V (Å ³)	81.08	81.25	81.03	- 0.27

powder and pressed into pellets before characterization using a powder X-ray diffractometer (PANalytical X'pert Pro) with a Cu $K\alpha$ source and monochromator. X-ray powder diffraction raw data are presented in Fig. 5.1 A Rietveld refinement was performed using the TOPAS software package. The space group of CuO (C2/c) was assumed to be unchanged on substituting up to 5% Zn, resulting in the unit cell parameters presented in Table 5.1. No new diffraction peaks associated with the single-phase doped material were seen, supporting this assumption. Weak peaks indicating the presence of small amounts of unreacted ZnO were detected. A clear increase in a , decrease in b , a very small change in c and an increase in β , are all in good agreement with the trend reported by Arbuzova et al. [148] for up to 3% Zn substitution as illustrated in Fig. 5.2.

It is interesting to note that the overall effect of replacing 5% of Cu with Zn is a decrease in the unit cell volume V , having a similar influence to pressure,[120] although doping does not introduce an isotropic change in a , b and c . The change in V is now discussed in the context of the ionic radii of Cu^{2+} and Zn^{2+} . Ionic radii are commonly quoted based on tabulated values for ions with a coordination number $N = 6$ (octahedral coordination). However, in cupric oxide the Cu^{2+} ions are coordinated with four coplanar oxygen ions situated at the corners of

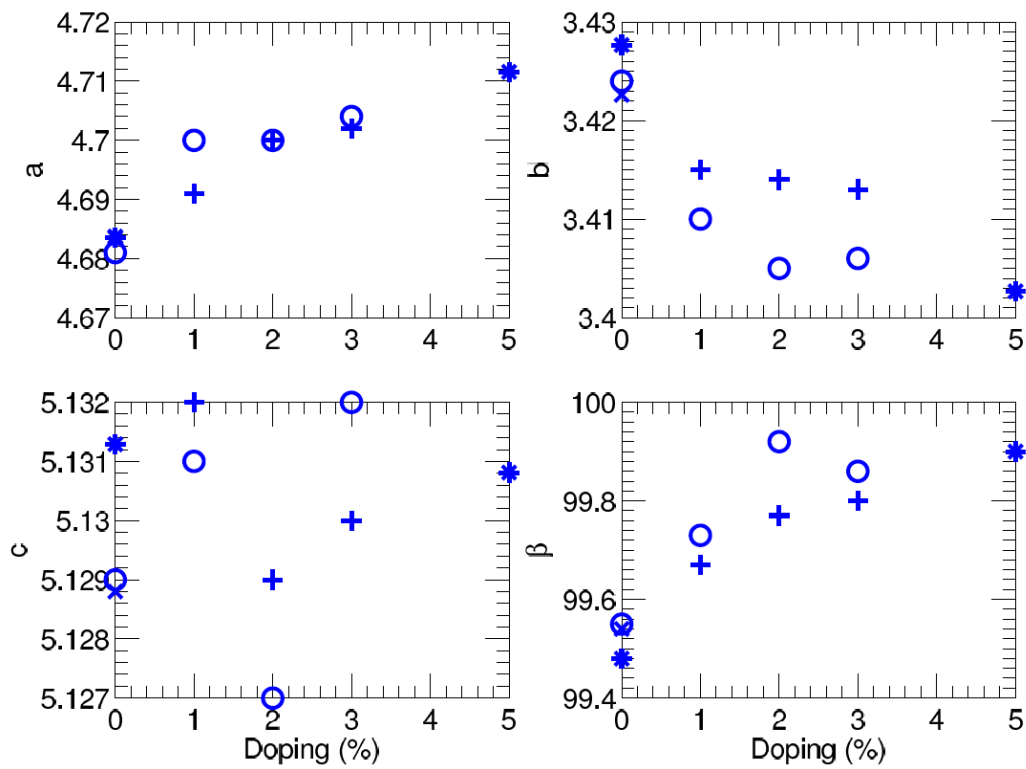


Figure 5.2: Comparison of unit cell parameters, a , b , c , and β , for $\text{Cu}_{1-x}\text{Zn}_x\text{O}$ from three different sources. The marks are the same for each data source across the four panels: \times denotes data from Åsbrink and Norrby [121], \circ are slow cooled samples grown by Abruzova et al [148], $+$, also grown by Abruzova et al [148], are annealed at 800 K under oxygen flow for 20 hours, and finally, $*$ are the samples used in this thesis.

an almost regular parallelogram, due to a strong Jahn-Teller distortion. The oxygens are coordinated by four Cu^{2+} ions situated at the corners of a distorted tetrahedron [121]. The ‘crystal radii’ from Shannon and Prewitt [153; 154] are therefore appropriate for tetrahedrally coordinated O^{2-} ions, and square-planar Cu^{2+} ions in CuO, rather than the ‘effective ionic radii’, which are calculated based on an octahedrally coordinated ions. While Cu^{2+} and Zn^{2+} radii for $N = 6$ are 0.87 Å and 0.89 Å respectively, square-planar coordinated Cu^{2+} with $N = 4$ has a crystal radius of 0.76 Å. There is no value for square-planar coordinated Zn^{2+} as there is no Jahn-Teller effect in this ion, which has a full 3d orbital. For a tetrahedrally coordinated Zn^{2+} ion ($N = 4$) the crystal radius is 0.74 Å suggesting that it would be perfectly reasonable for the effective radius to decrease when Zn^{2+} replaces Cu^{2+} in the CuO lattice, as shown by the X-ray diffraction data reported in Table 5.1. The decrease in unit cell volume corresponds to a positive hydrostatic pressure. Using the DFT predictions of Rocquefelte *et al.* [120], 5% zinc substitution changes the unit cell volume by the same fraction as a calculated hydrostatic pressure of roughly 150 MPa. The partially covalent nature of bonding in CuO will also produce a deviation from the behaviour expected from considering ionic bonding alone.

5.3 Dynamic magneto-electric response

5.3.1 Terahertz-time domain spectroscopy

The low-energy spin excitations of $\text{Cu}_{1-x}\text{Zn}_x\text{O}$ were probed by terahertz time-domain spectroscopy (THz-TDS) [85] in the energy range 0.8–12.4 meV, for sample temperatures from 2 K to 300 K. A wide-area GaAs photoconductive switch and a ZnTe electro-optic crystal were used to generate and detect single-cycle

pulses of THz radiation transmitted through the samples. THz-TDS directly determines the amplitude of the electric field E_ω after interaction with the sample, providing knowledge of the complex refractive index $\tilde{n} = n + i\kappa$. Using linearly polarised THz radiation and a variety of single crystals with different orientations the contributions to \tilde{n} from each optical axis were determined independently, and modes were identified as electric-dipole active (electromagnons) or magnetic-dipole active (magnons) [36], as discussed in the following sections.

5.3.2 Results: electromagnon

The THz absorption coefficient $\alpha = 2\omega\kappa/c$ for a single crystal with $x = 5\%$ (oriented with $E_\omega \parallel (101)$ and $H_\omega \parallel (010)$) is reported in Fig. 5.3(a) for different temperatures. A monotonic increase in α with energy is observed for temperatures below 159.5 K and above 190 K, as evidenced by the dash-dotted curve for $T = 159.0$ K. This increase in α results from the IR-active phonons for $E_\omega \parallel (101)$ (B_u^1 , B_u^2 and B_u^3 , Sec. 5.4). Zinc substitution modifies the IR-active phonon modes of CuO, as discussed in Sec. 5.4, and produces an enhanced absorption of THz radiation above 4 meV for $x = 5\%$ in comparison to $x = 0$.

At $T = 159.5$ K (dashed line) a clear resonant absorption feature emerges around 3 meV, which redshifts and strengthens at $T = 170.0$ K (solid line). The change in absorption coefficient $\Delta\alpha(T) = \alpha(T) - \alpha(T_0)$ is shown in Fig. 5.3(a) to elucidate the changes in α with respect to $T_0 = 159.0$ K, for $T = 159.5$ K (dashed line) and $T = 170.0$ K (solid line). This absorption mode was assigned as an electromagnon as no such feature was present for $E_\omega \parallel (010)$ or $E_\omega \parallel (10\bar{1})$ and regardless of the direction of H_ω , as found for the pure material [155]. Therefore the $E_\omega \parallel (101)$ electromagnon selection rule is preserved on substitution, and the change in \tilde{n} can be ascribed to a change in the dielectric function.

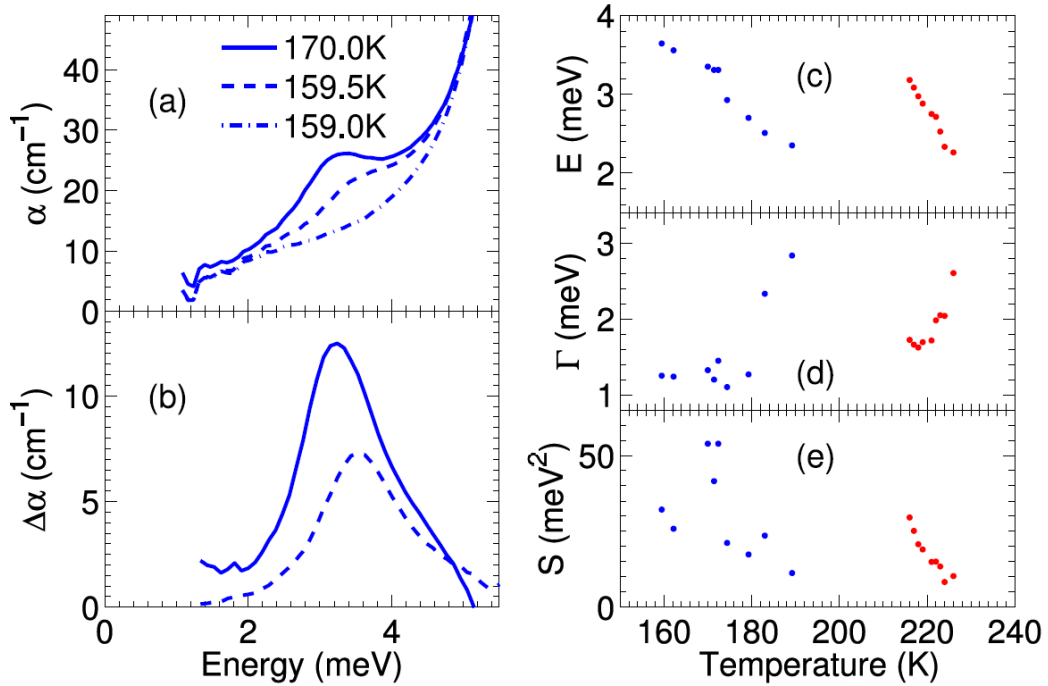


Figure 5.3: (a) THz absorption coefficient α measured for $\text{Cu}_{0.95}\text{Zn}_{0.05}\text{O}$ with $E_\omega \parallel (101)$ and $H_\omega \parallel (010)$ for temperatures 159.0 K (dash-dotted line), 159.5 K (dashed line) and 170.0 K (solid line). The onset of the electromagnon absorption resonance around 3 meV is clear at $T = 159.5$ K. (b) Relative absorption $\Delta\alpha(T) = \alpha(T) - \alpha(T_0)$ with $T_0 = 159.0$ K and $T = 159.5$ K (dashed line) and $T = 170.0$ K (solid line). (c) Energy E , (d) linewidth Γ and (e) oscillator strength S of the electromagnon for $x = 5\%$ (blue points, left) and $x = 0$ (red points, right). E lowers, Γ diverges and S decreases as the temperature rises towards $T_{N2} = 190$ K ($x = 5\%$) or $T_{N2} = 230$ K ($x = 0\%$).

To extract the temperature dependence of the electromagnon resonance the change in absorption coefficient was modelled by a single Lorentzian oscillator with an added linear term (which accounts for the low frequency tail of the broad higher lying phonon modes), as discussed in detail in Ref. 155. The extracted electromagnon energies are plotted in Fig. 5.3(c) for $x = 5\%$ in comparison to $x = 0\%$. The electromagnon is uniquely present in the multiferroic state of CuO, from $T_{N1}=213$ K to $T_{N2}=230$ K, and between $T_{N1}=159.5$ K and $T_{N2}=190$ K for $x = 5\%$. These temperature ranges are consistent with those extracted from anomalies in the magnetic susceptibility [122]. A significant rise in the electromagnon energy at T_{N1} from 3.1 meV in CuO to 3.7 meV in $\text{Cu}_{0.95}\text{Zn}_{0.05}\text{O}$ can be seen. The linewidth Γ of the electromagnon is only weakly affected by alloying with Zn, with comparable values for $x = 0$ and $x = 5\%$. Γ can be seen to diverge in Fig. 5.3(d) when $T \rightarrow T_{N2}$. The oscillator strength S reduces towards zero at T_{N2} , as reported in Fig. 5.3(e).

5.3.3 Results: magnon

In pure CuO a magnon excitation at 6.6 meV at 10 K, with linewidth ≤ 0.1 meV, has been previously observed by THz-TDS [155]. This magnon was active when $H_\omega \parallel (101)$, and only in the commensurate AF1 magnetic phase of CuO. In the present study an absorption feature was observed at 3 meV in the commensurate state, as pictured in Fig. 5.4(a) and (b) at 4 K (solid lines) and 20 K (dashed lines). The mode was observed at the same energy for $H_\omega \parallel (101)$, $E_\omega \parallel (010)$ and $H_\omega \parallel (101)$, $E_\omega \parallel (10\bar{1})$, as indicated by the * and \circ symbols in Fig. 5.4(c). The $H_\omega \parallel (101)$ selection rule (independent of the direction of E_ω) implies that this mode is also a magnon, obeying the same selection rule as the 6.6 meV magnon in CuO.

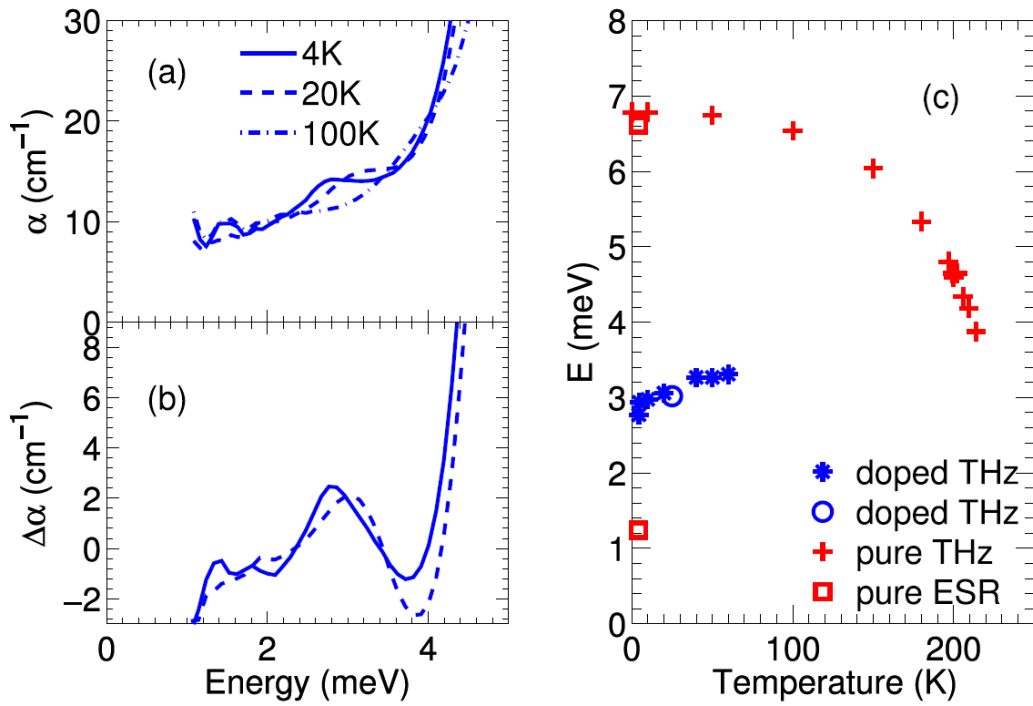


Figure 5.4: Magnon resonances in $\text{Cu}_{1-x}\text{Zn}_x\text{O}$. (a) Absorption α is shown for selected temperatures for $H_\omega \parallel (101)$, $E_\omega \parallel (010)$. (b) Relative absorption $\Delta\alpha = \alpha(T) - \alpha(T_0)$ with $T_0 = 100\text{K}$ showing the magnon mode around 3 meV. (c) Magnon energies for $\text{Cu}_{0.95}\text{Zn}_{0.05}\text{O}$ versus temperature. Data are presented for $x = 5\%$ for $H_\omega \parallel (101)$, $E_\omega \parallel (010)$ in (blue *) and $H_\omega \parallel (101)$, $E_\omega \parallel (10\bar{1})$ (blue o). Magnon energies for CuO from electron-spin resonance measurements (red squares), [142] and THz-TDS (red pluses) [156] are also shown.

The temperature dependence of the energy E of this magnon mode is reported in Fig. 5.4(c) by the * symbols, and weakly increases in E with temperature until the mode disappears at around 70 K. In comparison, the energy of the observed magnon in CuO was found to decrease as the temperature increased towards T_{N1} (+ symbols), as shown in Fig. 5.4(c), and in accordance with a simple model of the sublattice magnetisation [156]. The stronger absorption above 4 meV for $x = 5\%$ prohibited verification of whether the 6.6 meV magnon ($x = 0, 10$ K) was present in the alloyed samples. The width Γ of the 3 meV magnon for $x = 5\%$ is substantially broader than that of the magnon in pure CuO ($\Gamma \leq 0.1$ meV at 10 K). At present it is unclear whether the 3 meV mode for $x = 5\%$ is the same spin excitation as seen at 6.6 meV in CuO, or if it is in fact related to the 1.2 meV mode seen in electron spin resonance (ESR) measurements [142]. Neutron or ESR experiments on $\text{Cu}_{1-x}\text{Zn}_x\text{O}$ are needed to clarify the situation.

It is interesting to note that the 3 meV magnon in $\text{Cu}_{0.95}\text{Zn}_{0.05}\text{O}$ is not visible above $T^* \sim 70$ K, well below $T_{N1}=159.5$ K, while the higher-lying magnon in CuO persists to $T_{N1}=213$ K. This may indicate a different origin for these two modes. Interestingly, anomalies in the magnetization [115] and resistivity [157] have been reported at about 150 K in CuO, hinting at a possible lower temperature phase.

5.4 Dynamic lattice response

5.4.1 Symmetry analysis

The predicted lattice vibrations of CuO allowed by symmetry have been established in the literature. A factor group analysis assuming the centrosymmetric $C2/c$ space group, and using the tables of Rousseau *et al.* [158], gives the following

representation:

$$\Gamma_{\text{CuO}} = A_g + 2B_g + 4A_u + 5B_u \quad (5.1)$$

The primitive unit cell of CuO contains two formula units giving $3N = 12$ phonon modes. Three of the modes correspond to acoustic phonons ($A_u + 2B_u$) which have $\nu = 0$ at the Brillouin zone centre, leaving nine remaining active phonon modes. In a centrosymmetric crystal none of the principal phonon modes are both infrared and Raman active, and therefore three Raman active modes ($A_g + 2B_g$) and six infrared active modes ($3A_u + 3B_u$) are expected for CuO. The symmetry analysis is presumed to be unchanged for $\text{Cu}_{0.95}\text{Zn}_{0.05}\text{O}$, as the XRD results reported in Sec. 5.2 are consistent with space group $C2/c$. The assignment of phonon modes below is therefore based on existing literature for $x = 0$. The relative atomic displacements of the zone-centre phonon modes have been calculated previously [159].

5.4.2 FTIR and Raman spectroscopy

Fourier-transform infrared spectroscopy was performed in the energy range 10–1000 meV and between 80 K and 300 K using a Bruker 70v spectrometer with a cryostat insert (Oxford Instruments Microstat). Near-normal incidence (11°) unpolarised reflectivity spectra were recorded on all samples. A global light source was used with a KBr beamsplitter and DLaTGS detector in the mid-IR range (40–1000 meV). The far-IR measurements (10–90 meV) used a Si beamsplitter and DTGS detector. For temperature-dependent measurements, a cryostat with KRS-5 windows was used in conjunction with the MIR set-up to focus on the spectral range around the A_u^3 phonon mode, known to show strong spin-phonon

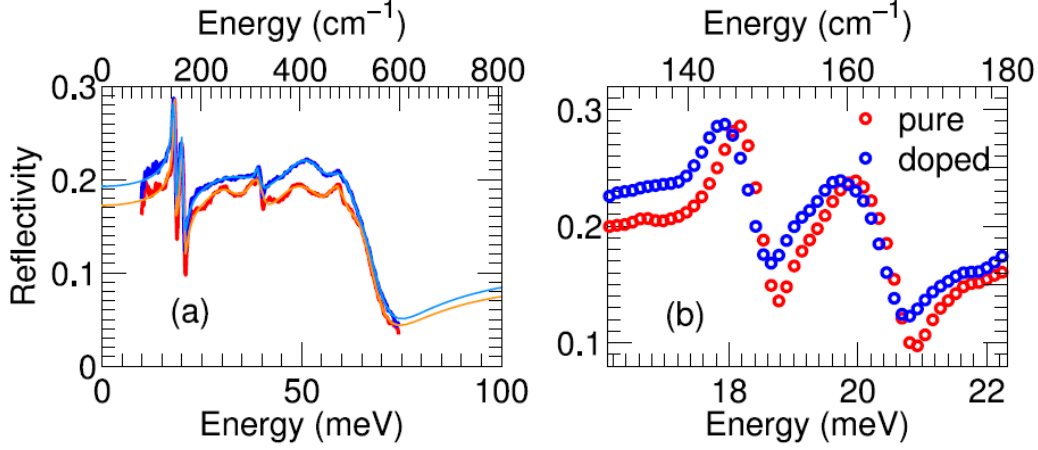


Figure 5.5: (a) Reflectivity of polycrystalline samples of CuO (red), $\text{Cu}_{0.95}\text{Zn}_{0.05}\text{O}$ (blue) modelled by a sum of six Lorentzian oscillators (orange and light blue, respectively), as described in the text. (b) Reflectivity in the frequency range of the A_u^1 and B_u^1 modes.

coupling in undoped CuO [124].

A Raman microscope (Renishaw inVia Reflex) in a backscattering geometry was used to measure the Raman shift in the energy range 25–400 meV after exciting with a $\lambda = 633$ nm HeNe laser. A wide-angle $50\times$ objective lens was used to focus and collect the light. A nitrogen-cooled temperature stage (Linkham THM S600) was used for measurements in the range 90–300 K.

5.4.3 Results: IR-active phonons

All six IR-active phonon modes of $\text{Cu}_{1-x}\text{Zn}_x\text{O}$ were characterised by FTIR reflectivity measurements on both single crystal and polycrystalline samples. Representative room-temperature reflectivity spectra are shown in Fig. 5.5(a) on polycrystalline samples with $x = 0$ and $x = 0.05$. Experimental data (thick lines) were modelled by a dielectric function containing six Lorentzians, following Ref. 124, which reported a polarized FTIR study of single crystals with various

orientations. Fitting was performed using the RefFIT software package, which uses a Levenberg-Marquardt least-squares fitting algorithm [105], producing the thin lines in Fig. 5.5(a). The obtained phonon energies are summarized in Table 5.2, and are in good agreement with the literature for $x = 0$ [124]. The error in each fit parameter was estimated as follows. The chosen parameter was increased, allowing the other parameters to relax each time, until χ^2 increased by 10% from its global minimum. This provides a useful estimate of the error in each parameter.

As evidenced in Table 5.2, substitution in general softens the phonon frequencies, and broadens their linewidth. The error in the frequencies of the A_u^2 and $B_u^{2,3}$ modes, determined by the fitting procedure outlined above, is larger, and these modes are broad even in pure CuO. Thus the focus in the following is on the lower frequency IR-active modes, Raman modes and the A_u^3 mode, which is strongly coupled to the improper ferroelectric phase transition in CuO [124].

The reduction in phonon mode frequency and broadening upon Zn substitution can be most clearly seen for the sharp, low-frequency A_u^1 and B_u^1 phonons, and the Raman modes. For instance, FTIR reflectivity spectra of the A_u^1 and B_u^1 modes of polycrystalline samples are shown in Fig. 5.5(b), and show a clear shift to lower frequency after zinc substitution. The A_u^1 mode is an out-of-plane bending mode where O^{2-} ions move in the b -direction with Cu^{2+} motion mainly in the ac -plane [159]. The A_u^1 mode softens from 20.20 ± 0.07 meV to 20.02 ± 0.07 meV, whilst simultaneously broadening from linewidth $\Gamma = 0.7 \pm 0.1$ meV to 0.8 ± 0.2 meV, upon substitution. The B_u^1 mode is complementary, with the O^{2-} motion confined to the ac -plane with Cu^{2+} ions moving mainly along the b -axis [159]. This mode lowers from 18.30 ± 0.05 meV to 18.09 ± 0.06 meV whilst simultaneously broadening from $\Gamma = 0.47 \pm 0.11$ meV to 0.71 ± 0.15 meV.

Table 5.2: Summary of the principal phonon mode energies in $\text{Cu}_{1-x}\text{Zn}_x\text{O}$ (in meV). Results on single crystal and polycrystalline $\text{Cu}_{1-x}\text{Zn}_x\text{O}$ are compared with results from the literature (polycrystalline CuO: Ref. 160; single crystals: Ref. 124 for IR-active modes, Ref. 141 for Raman-active modes). The errors indicated were calculated as described in the main text.

Mode, Activity	Polycrystalline		Single crystal	
	CuO (Ref. 160)	CuO	CuO (Refs. 124; 141)	CuO
A_u^1 IR, E b	20.15	20.20 ± 0.07	19.90	20.26 ± 0.09
A_u^2 IR, E b	39.80	39.30 ± 0.62	39.86	39.68 ± 0.37
A_u^3 IR, E b	50.8	52.1 ± 1.9	50.7	49.7 ± 1.4
B_u^1 IR, E⊥b	18.23	18.30 ± 0.05	17.97	18.35 ± 0.07
B_u^2 IR, E⊥b	59.45	59.0 ± 0.9	58.22	59.6 ± 0.6
B_u^3 IR, E⊥b	66.3	64.2 ± 1.7	64.8	69.1 ± 0.6
A_g Raman			37.19	36.91 ± 0.03
B_g^1 Raman			42.90	42.89 ± 0.07
B_g^2 Raman			78.3	78.1 ± 0.7
				76.9 ± 0.5

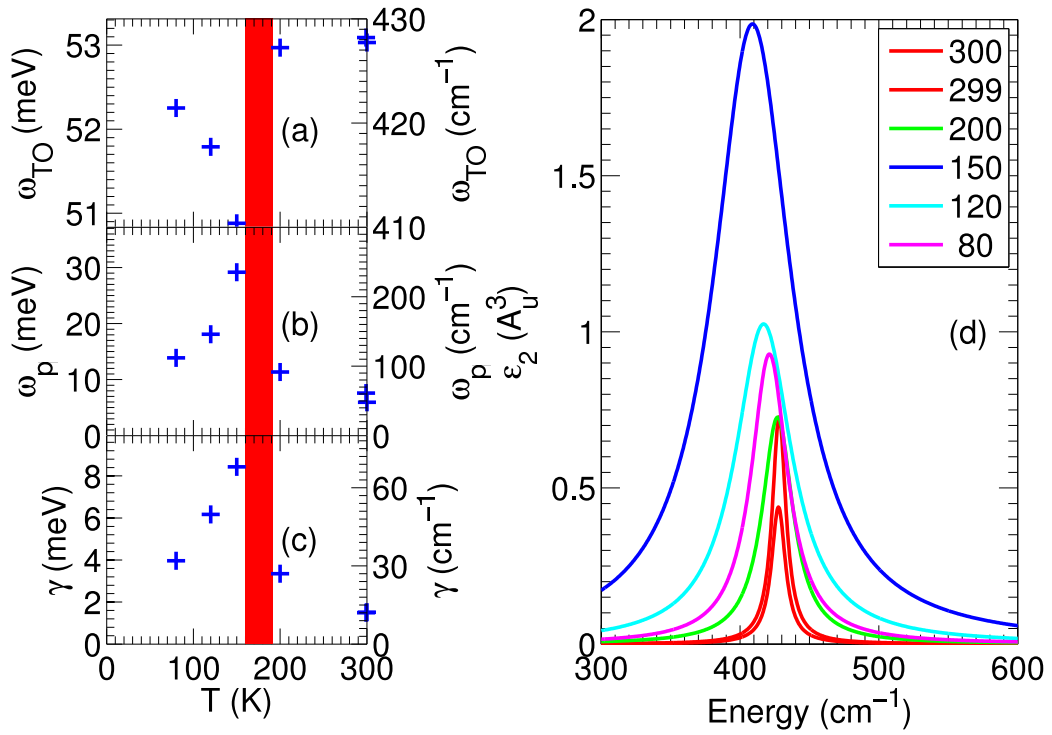


Figure 5.6: Details of the A_u^3 phonon mode in $\text{Cu}_{0.95}\text{Zn}_{0.05}\text{O}$, which is strongly coupled to the AF1–AF2 phase transition. Panels (a), (b) and (c) show the mode frequency, plasma frequency and linewidth as a function of temperature. The multiferroic AF2 phase is highlighted in red in these first three panels. (d) shows the temperature evolution of the A_u^3 phonon mode by plotting the contribution of A_u^3 to ϵ_2 as calculated from the extracted oscillator parameters shown in panels (a–c).

Unlike the other phonon modes, which are only weakly temperature dependent, the A_u^3 mode of CuO shows an unusually strong temperature dependence. As reported by Kuz'menko *et al.* [124], the oscillator strength and linewidth of the A_u^3 mode are strongly enhanced in and near the incommensurate magnetic phase of CuO. Kuz'menko *et al.* postulated that the A_u^3 mode (at about 51 meV) could couple to two Γ -point magnons each at 23 meV (5.6 THz), as observed by neutron scattering [113]. Here, a similar behaviour of the A_u^3 phonon is reported in Fig. 5.6 for $\text{Cu}_{0.95}\text{Zn}_{0.05}\text{O}$. A sharp dip in frequency in the multiferroic phase (shaded area) is accompanied by a peak in the linewidth $\Gamma(T)$, where $\Gamma(150\text{ K}) \geq 5\Gamma(300\text{ K})$. The A_u^3 phonon exhibits the largest b -axis oxygen movement of all the IR-active phonon modes [159]. This observation that the A_u^3 mode follows the same pattern after substitution of copper with zinc is further evidence that the magnetic structure of CuO is preserved, but with lower ordering temperatures, in agreement with the THz electromagnon reported in Sec. 5.3.

5.4.4 Results: Raman-active phonons

The unpolarized Raman spectra of $\text{Cu}_{1-x}\text{Zn}_x\text{O}$ single crystals (with (101) and (010) in-plane) are reported in Fig. 5.7. The principle phonons A_g (\blacklozenge symbol), B_g^1 (\blacksquare) and B_g^2 (\blacktriangle) redshift in energy E and broaden in linewidth Γ on Zn-substitution (see also Table 5.2). The principle phonon modes of $\text{Cu}_{1-x}\text{Zn}_x\text{O}$ narrow and harden on cooling, as the two upper curves in Fig. 5.7 illustrate, and are assigned based on mode assignments from polarized Raman spectroscopy [141]. Additional Raman peaks beyond the three predicted by the symmetry analysis are observed in Fig. 5.7 at 29.3 meV (\diamond), 73 meV (\triangle), 142 meV (\circ), 289 meV (\times), and 383 meV ($*$). The extra modes can be divided into two distinct groups: (i) those present at all temperatures (modes \triangle , \circ and \times) and (ii) those

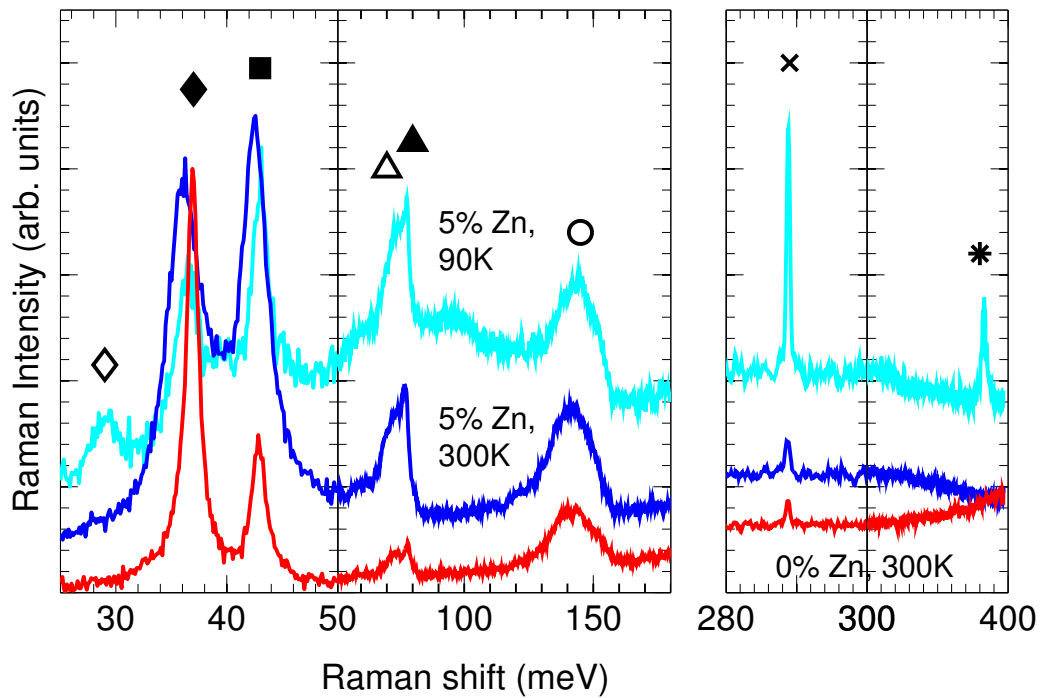


Figure 5.7: Raman spectra for CuO at 300 K (bottom line) and Cu_{0.95}Zn_{0.05}O at 300 K (middle) and 90 K (top). Note the split x -axis scale. The principal Raman active modes are A_g (◆), B_g^1 (■) and B_g^2 (▲). Extra Raman modes are labelled ◇, △, ○, × and *.

activated only at low temperature (modes \diamond and $*$). None of these extra modes can be attributed to a ZnO impurity phase as all modes are present in both pure and doped samples.

The three principal Raman modes differ from the IR-active modes as only the O^{2-} ions are displaced, and Cu^{2+} sites remain stationary. The A_g phonon is a symmetric breathing mode with motion only along the b -axis, while the B_g modes involve motion only in the ac -plane [159]. On substitution $E(A_g)$ decreases from 36.91 ± 0.02 meV to 36.27 ± 0.15 meV while $\Gamma(A_g)$ increases from 1.41 ± 0.04 meV to 3.5 ± 0.4 meV; $E(B_g^1)$ softens from 42.90 ± 0.07 meV to 42.5 ± 0.1 meV while $\Gamma(B_g^1)$ widens from 1.41 ± 0.06 meV to 3.0 ± 0.4 meV.

Two overlapping peaks (\triangle and \blacktriangle) are evident in the Raman scattering data in Fig. 5.7 around 75 meV, in both CuO and $Cu_{0.95}Zn_{0.05}O$. Here B_g^2 is assigned following Choi *et al.*[141] to the higher and broader peak at $E(B_g^2) = 78.1 \pm 0.7$ meV ($x = 0$), which shifts to 76.9 ± 0.5 meV at $x = 5\%$. The second peak (\triangle) is 5.1 meV lower, a splitting that is independent of alloy fraction and temperature. One possible origin of this peak is the IR-active B_u^3 mode at 69.1 meV, where oxygens move roughly along the Cu–O chains in the $(10\bar{1})$ direction. Mixed IR and Raman activity can only be obtained, however, in crystals without a centre of symmetry, and this would require a different space group than C2/c at all temperatures. Alternative interpretations of this split peak are: (i) that the lattice potential is anharmonic, which can give multiple Raman lines [108]; (ii) it is a Fano resonance, with an asymmetric lineshape, caused by coupling to a continuum of background states.

Raman lines at 140 meV (\circ) and 288 meV (\times) are also evident in Fig. 5.7, and are seen for $Cu_{1-x}Zn_xO$ at all temperatures. A recent polarization-resolved Raman study reported that the broad band around 140 meV is a second-order Ra-

man processes involving overtones of four relatively dispersionless phonon bands (as determined by DFT) [161]. The two highest extra Raman modes reported here for $\text{Cu}_{1-x}\text{Zn}_x\text{O}$ at 288 meV (\times , present at all temperatures) and 390 meV ($*$, appearing below T_{N1}) are too high in energy to correspond to first-order Raman scattering from single vibrational modes, and may result from defects or multi-phonon processes.

The observation of five extra Raman-active modes in the commensurate AF1 state was reported by Chen *et al.* [162], who explained the extra modes by a mechanism relying upon zone-folding. The magnetic unit cell of CuO can be written $\mathbf{a}_{\text{M}} = \mathbf{a} + \mathbf{c}$, $\mathbf{b}_{\text{M}} = \mathbf{b}$ and $\mathbf{c}_{\text{M}} = \mathbf{a} - \mathbf{c}$ [163]. The X -point of the crystallographic unit cell corresponds to the zone centre of the magnetic cell. If the displacement pattern of phonons at X modulates the superexchange interaction, then Raman active modes arise [162]. A strong mode at 29.3 meV (240 cm^{-1}) that appears below 210 K was reported by Chen *et al.*, and can also be observed for $\text{Cu}_{1-x}\text{Zn}_x\text{O}$ in Fig. 5.7. This mode was previously found to lower in energy for ^{65}CuO in comparison to ^{63}CuO , providing evidence that this mode results from an LA motion of Cu^{2+} ions [162]. The principal modes were at the same energies for ^{65}CuO and ^{63}CuO , as expected for these vibrations, which are only associated with oxygen motion. Further evidence for the magnetically-induced zone-folding of phonons was reported by Kuz'menko *et al.*, who reported additional IR-active modes that were linked to phonon modes at the X and A points [124]. However, it is interesting to note that these additional modes were present above T_{N2} , in the paramagnetic state. A doubling of the unit cell from $\{a, b, c\} \rightarrow \{a + c, b, a - c\}$ was proposed by Kuz'menko *et al.* [124], in line with the magnetic cell.

5.4.5 Discussion: Influence of alloying

The substitution of zinc on to copper sites will change the effective force constants between neighbouring oxygen ions. The addition of an extra d -orbital electron (Cu^{2+} is $3d^9$ and Zn^{2+} is $3d^{10}$) will have the effect of locally eliminating the Jahn-Teller distortion and adding an electron to the orbitals. This will reduce the bonding character of the interactions, effectively reducing the force constants and therefore the frequency of the phonon modes. The enhanced mass of Zn in comparison to Cu should also act to lower phonon mode frequencies for $\text{Cu}_{1-x}\text{Zn}_x\text{O}$. Similar effects have been seen in studies of potassium substitution in $\text{Ba}_{1-x}\text{K}_x\text{Fe}_2\text{As}_2$ [164] and more pertinently zinc substitution in $\text{YBa}_2\text{Cu}_{4-x}\text{Zn}_x\text{O}_8$ [165]. Phonon modes in the superconducting parent compound BaFe_2As_2 soften and broaden on alloying with potassium, well described by a Born–von Kármán force constant model. Superconducting $\text{YBa}_2\text{Cu}_4\text{O}_8$, which has very similar CuO_4 plaquettes to CuO , behaves comparably on alloying with zinc, as shown by phonons measured below T_C . Furthermore, in this material the substitution of zinc locally dilutes the spin dynamics leading to a suppression of T_C analogous to the suppression of T_N reported here for $\text{Cu}_{1-x}\text{Zn}_x\text{O}$.

A broadened phonon linewidth with increasing alloy fraction have been observed in both the superconducting compounds mentioned above [164; 165]. Furthermore, the effect has been particularly well studied in Mn-doped ZnO and is successfully described by a spatial correlation model [166; 167]. Essentially, the disorder introduced by random substitution onto Cu sites breaks the translational symmetry of the crystal thus relaxing the $q \approx 0$ selection rule. Now small areas (rather than single points) of the Brillouin-zone may be activated by light, allowing phonons of slightly different energies to be excited by photons, thus broadening the observed linewidth.

5.5 Discussion

Alloying with 5% Zn almost doubles the temperature width of the multiferroic phase from $\Delta T_{\text{AF2}}(\text{CuO}) = 17 \text{ K}$ to $\Delta T_{\text{AF2}}(\text{Cu}_{0.95}\text{Zn}_{0.05}\text{O}) = 30 \text{ K}$. T_{N1} falls from 213 K to 159.5 K and T_{N2} falls from 230 K to 190 K.

CuO is a quasi-one-dimensional (1-D) collinear Heisenberg antiferromagnet [138]. The ratio $J_{\text{inter-chain}}/J_{\text{intra-chain}} \sim 10^{-1}$ in CuO [113] indicates that it is only weakly 1-D in comparison to well studied materials such as TMMC [168] where $J_{\text{inter-chain}}/J_{\text{intra-chain}} \sim 10^{-4}$. However, as we see below, the effect of substitution is well described within a quasi-1-D model.

Substitution of magnetic ions with non-magnetic ions has been studied both theoretically and experimentally in a variety of systems: 1-D antiferromagnetic spin chains [169] such as TMMC: Cd [168], $(\text{CH}_3\text{NH}_3)\text{MnCl}_3 \cdot 2\text{H}_2\text{O}:\text{Cd}$ [170] and the Haldane system doped with Zn^{2+} and Mn^{2+} [171]; 2-D Heisenberg antiferromagnets [172] including $\text{La}_2\text{CuO}_4:\text{[Zn, Mg]}$ [173] and $\text{Li}_2\text{VO}_4:\text{Ti}$ [174] including a focus on frustrated systems [175]. Finally, the 3-D multiferroic antiferromagnet MnWO_4 [176] has been alloyed with Zn and Mg.

Néel temperatures are suppressed on alloying across all these systems. There are two separate but related effects in play here. Spin dilution due to replacing random spins by non-magnetic ions affects long range magnetic correlations. Disorder effects occur because the magnetic superexchange coupling is locally zero around the non-magnetic ions. These effects are particularly pronounced in quasi-1-D systems [169] such as CuO. The correlation length of a group of neighbouring spins along a chain increases as the temperature decreases, until the whole crystal is correlated below the magnetic ordering temperature. Non-magnetic impurities break communication along the chain and restrict the growth of the correlation

length to the average impurity separation. A mean-field theory predicts a dramatic decrease in ordering temperature driven by non-magnetic impurities in a 1-D system [169].

A classical Heisenberg model for a quasi-1-D system [169] predicts $\frac{T_N(x)}{T_N(0)} \simeq 1 - \frac{J}{T_N(0)}x$ for $x \ll \frac{T_N(0)}{2J} \ll 1$. For CuO with a 5% doping level and $J \simeq 80 \text{ meV}$ [113], this predicts $T_N(x = 0.05) \simeq 0.8 T_N(x = 0) = 184 \text{ K}$ close to our measured value of 190 K.

Furthermore, the widening of the AF2 phase with respect to the AF1 phase has been hinted at in the work of Henley who calculates that if disorder is introduced into the system, a non-collinear spin state will be stabilised with respect to a collinear one in a vector antiferromagnet with competing interactions [175]. Evidence supporting this exists in the form of optical-pump X-ray-probe experiments on CuO at 207 K [136]. At this temperature, just below the first-order phase transition at T_{N1} , domains of both phases co-exist within the sample. Nonthermal spin disorder is induced by femtosecond pulses of 1.55 eV light, which reduces the intensity of the X-ray diffraction peak associated with the incommensurate phase less substantially than the peak for the commensurate phase.

5.6 Summary

Terahertz time-domain spectroscopy showed that multiferroic ordering is preserved in $\text{Cu}_{1-x}\text{Zn}_x\text{O}$ for $0 < x < 0.05$. Electromagnons were observed in both pure and alloyed materials, and mode frequencies and widths were relatively insensitive to substitution. A reduction in the antiferromagnetic ordering temperature was discussed in terms of spin dilution effects. The width of the multiferroic phase increased from 17 K to 30 K on addition of 5% Zn. Infrared and

Raman active phonons weakened and widened on substitution of zinc for copper. A pronounced softening and broadening of the A_u^3 phonon mode occurred at the collinear/non-collinear phase boundary in both pure and alloyed materials, highlighting the direct influence of spin-lattice coupling on this mode.

Chapter 6

Magnetoresistance in

$\text{La}_{0.7}\text{Sr}_{0.3}\text{MnO}_3\text{:ZnO}$

nanocolumnar thin films

6.1 $\text{La}_{0.7}\text{Sr}_{0.3}\text{MnO}_3$

$\text{La}_{0.7}\text{Sr}_{0.3}\text{MnO}_3$ is one of a family of manganite materials that have been intensively studied since it was discovered in the 1950s that they exhibit novel physical phenomena including: a metal-insulator transition (unlike conventional ferromagnetic metals such as Fe, Co, Ni or Gd); colossal magneto-resistance (CMR); magnetic anisotropy; and spin glass behaviour. Rich phase diagrams exist for the alkaline-earth (A) and rare-earth (R) manganites $R_{1-x}A_x\text{MnO}_3$ [74]. In addition to the fascinating correlated-electron physics displayed by these materials, there is enormous potential for device applications, especially in making use of the CMR effect. However, in the pure materials, large magnetic fields >1 T are needed for these large effects on the magnetoresistance. In order to make useful

devices a response at much smaller magnetic fields is needed and so materials with good low-field magnetoresistance (LFMR) are sought by technologists [177]. Nanoscale phase separation in other branches of the manganite family is known to be important in determining their magnetic properties [72] and it is with this in mind that we have been motivated to investigate the effects of introducing a second phase into the $\text{La}_{0.7}\text{Sr}_{0.3}\text{MnO}_3$ films. More broadly, the THz conductivity of heterostructures is of great interest, with a number of conductivity models proposed [85]. Spin polarised tunnelling at grain boundaries is thought to be a key influence on LFMR and adding a second material, in this case the semiconductor ZnO, creates more grain boundaries, local structural disorder, chemical disorder and spin disorder at boundaries all of which have been suggested to influence the magnetoresistance [178; 179]. Pulsed laser deposition is an ideal way to create such systems as the materials can form ordered chequerboard structures of vertical phase separated nanocolumns giving considerable control and tunability over the nature of the interfaces [180].

Here we investigate 200 nm thick films of $(\text{La}_{0.7}\text{Sr}_{0.3}\text{MnO}_3)_{0.5}\text{:}(\text{ZnO})_{0.5}$ deposited on LaAlO_3 (LAO). Static and dynamic resistivity and magnetoresistance experiments, combined with photoconductivity measurements, provide insights into the nature of charge carriers in the LFMR region of this material. Relatively large effects on dynamic (1 THz) compared to d.c. properties highlight the differences between local and macroscopic conductivity in this system.

This chapter begins by introducing the LSMO:ZnO samples, detailing their growth and X-ray characterisation in Sec. 6.2. Static and dynamic conductivity are presented as a function of temperature in Sec. 6.3 and applied magnetic field in Sec. 6.4. Dynamic photoconductivity is presented in Sec. 6.5 before all results are discussed in Sec. 6.6. A brief summary and further work to complement this

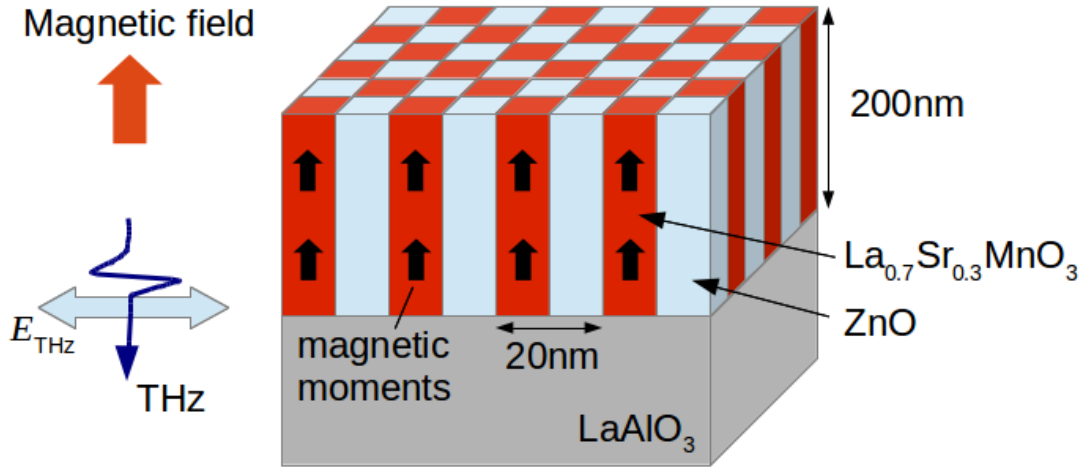


Figure 6.1: **Sample structure and experimental geometry for LSMO:ZnO nanocolumn samples.** Directions of applied d.c. magnetic field, THz pulse propagation vector and THz electric field are shown. The Mn magnetic moments are displayed as fat black arrows.

study are presented in Sec. 6.7.

The samples were grown by Aiping Chen at Los Alamos National Laboratory, USA. The X-ray experiment was performed by James Lloyd-Hughes and the data analysed by myself. Transport measurements were performed by Eun-Mi Choi in Cambridge. All other results are my own.

6.2 Sample preparation and structural characterisation

Epitaxial $\text{La}_{0.7}\text{Sr}_{0.3}\text{MnO}_3:\text{ZnO}$ [LSMO:ZnO] vertically aligned nanocomposite thin-films were grown on LaAlO_3 (001) substrates by pulsed laser deposition. Initially, a sintered powder target of correct stoichiometry is created. High-purity La_2O_3 , SrCO_3 , and MnO_2 are ground, pressed and sintered at 930 K in air for 24 h

to produce LSMO. The calcined LSMO powder is re-ground with ZnO powder in a one-to-one stoichiometric ratio before being pressed into a disk. This disk is then sintered at 1030 K for 12 h to make an LSMO:ZnO composite target.

LSMO:ZnO was then grown on a single crystal (001) LaAlO_3 (LAO) substrate by pulsed laser deposition. The chamber was evacuated to pressures $< 26.7 \mu\text{Pa}$ before deposition. A $\lambda = 248 \text{ nm}$ KrF excimer laser (Lambda Physik) was focussed onto the target with a fluence of 4.5 Jcm^{-2} and a repetition rate of 1 Hz. During deposition an oxygen pressure of 26.7 Pa was introduced to the chamber and the substrate was heated to 477 K. After deposition the sample was cooled to room temperature at a rate of 20 Kmin^{-1} under an oxygen pressure of 26.7 kPa to ensure full oxygenation. Vertically aligned nanocolumns of separate phases of LSMO and ZnO are formed in a structure as shown in Fig. 6.1, as investigated previously using X-ray diffraction and transmission electron microscope images [68; 177].

High resolution X-ray powder diffraction was used to examine the crystal structure at room temperature. Fig. 6.2 shows $\omega - 2\theta$ scans taken on a X-ray diffractometer (PANalytical X'pert Pro) with a Cu $K\alpha$ source and monochromator. Peaks are visible that correspond to out-of-plane lattice parameters for LSMO, ZnO and LAO. The LSMO peaks are indexed as the (001) and (002) peaks with $d_{(001)\text{LSMO}} = 3.927 \text{ \AA}$. This is larger than the bulk value of 3.870 \AA [68] meaning that the film is under tension in the out-of plane direction. The pseudocubic (001) LAO peak is measured to be 3.789 \AA meaning that LSMO is under compression in the plane of the film, supporting the previous assertion. The ZnO (11 $\bar{2}$ 0) lattice parameter is 3.249 \AA , which gives $5 \times d_{(001)\text{LSMO}} = 19.49 \text{ \AA}$, is slightly less than $6 \times d_{(11\bar{2}0)\text{ZnO}} = 19.63 \text{ \AA}$. Therefore, the ZnO nanocolumns actually tend to vertically compress the unit cell, suggesting that in-plane (horizontal)

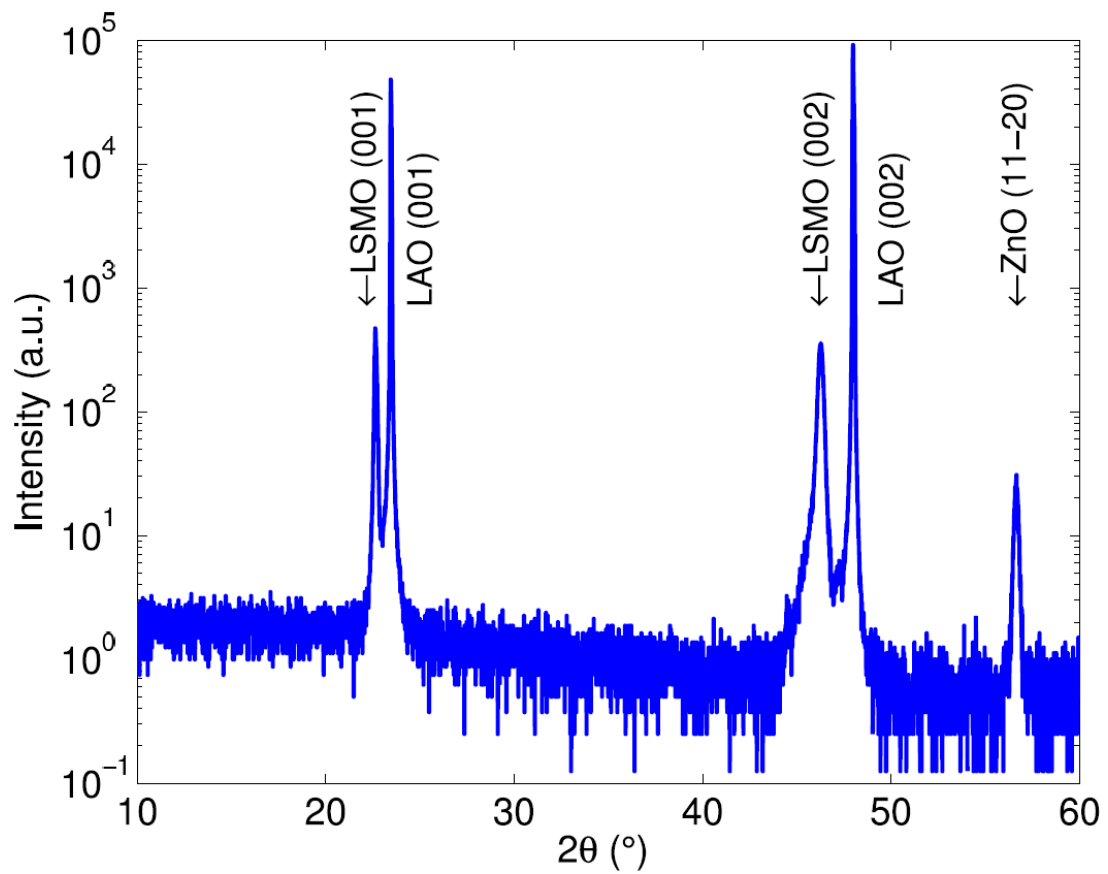


Figure 6.2: X-ray diffraction of $\text{La}_{0.7}\text{Sr}_{0.3}\text{MnO}_3\text{:ZnO}$ nanocolumns on LaAlO_3 substrate. The ratio of out-of-plane lattice parameters show that the lattice mismatch between nanocolumns is such that $6d_{\text{ZnO}} \simeq 5d_{\text{LSMO}}$, as described in Section 6.2.

substrate-induced unit cell compression is the dominant effect on the unit cell distortion from bulk values.

6.3 A. c. and d. c. temperature dependent dielectric response

Normalized zero-field d.c. resistance was measured as a function of temperature to extract the metal-insulator transition temperature (T_{MI}). Transport measurements were performed on the surface of the film using the four-point probe method. T_{MI} manifests as a maximum in the normalized d.c. resistivity in Fig. 6.4(b). This means that for our LSMO:ZnO thin film, $T_{\text{MI}} \simeq 300$ K, which is lower than the temperature for pure LSMO films grown using the same process at 344 K [68].

The MI transition is not clear in the THz conductivity data as there are only two data points above 240 K. However, both the a.c. conductivity and d.c. resistivity follow the same trend in Fig. 6.4. Heating above 300 K would be necessary to precisely characterise the MI transition in the THz frequency range. The difference in THz conductivity between room temperature and 10 K is $500 \Omega^{-1}\text{cm}^{-1}$ which is of the same order of magnitude as the change in d.c. conductivity ($\sim 220 \Omega^{-1}\text{cm}^{-1}$ [68]) but smaller than that measured in a separate study using THz-TDS on pure LSMO films ($10,000 \Omega^{-1}\text{cm}^{-1}$ [181]).

THz transmission, $E_{\omega}(T)/E_{\omega}(T = 10 \text{ K})$, spectra in the frequency range 0.2–2.2 THz, shown in Fig. 6.3, exhibit significant changes with temperature and are discussed further in Section 6.6. This ratio increases at higher temperature as the resistivity rises.

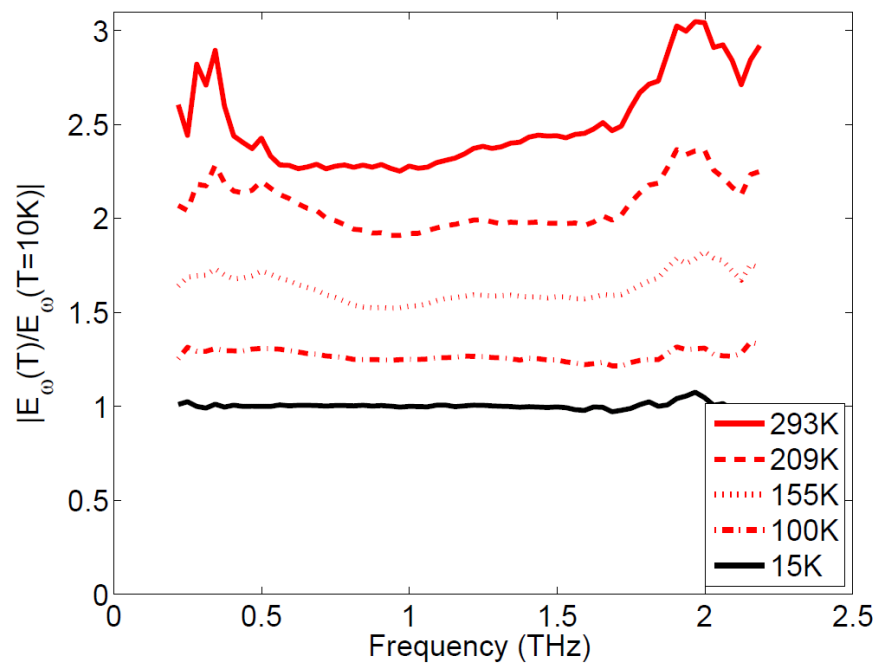


Figure 6.3: THz transmission relative to $T=10$ K, for $B=0$ T.

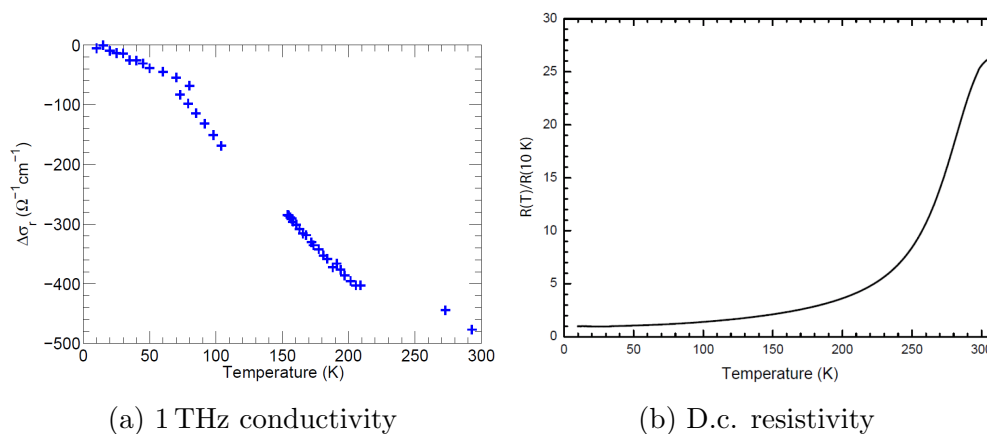


Figure 6.4: **Static resistivity and dynamic conductivity as a function of temperature.** (a) Change in conductivity at 1 THz as a function of temperature relative to THz conductivity at 10 K. (b) Static resistivity normalized by the 10 K resistivity.

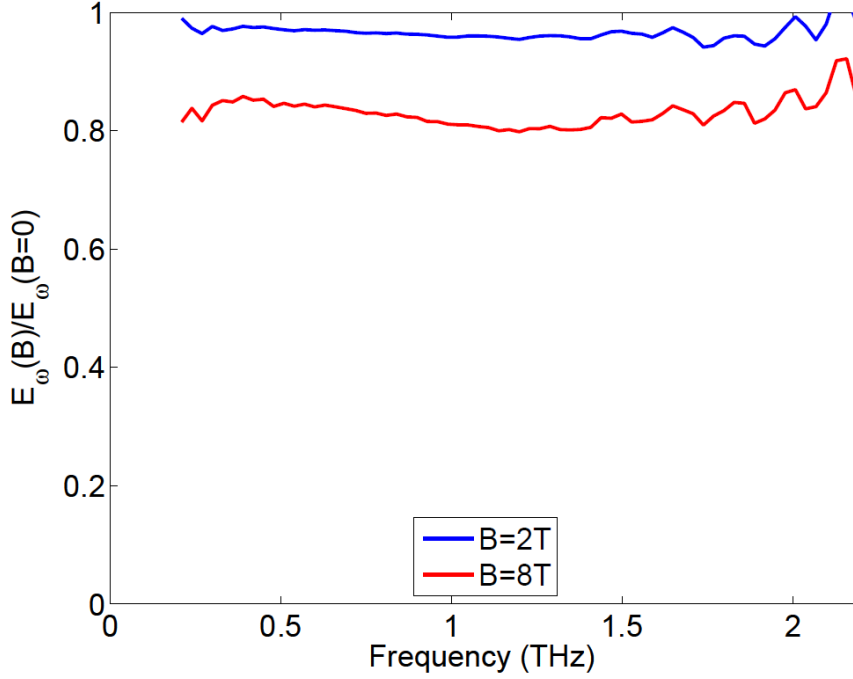


Figure 6.5: THz transmission relative to $B=0$ T, for $T=200$ K.

6.4 A. c. and d. c magnetoconductivity

The magneto-conductivity of LSMO:ZnO was measured at 200 K, which, as can be seen from the temperature dependence of the conductivity, is below T_{MI} . Both static (d.c. resistance measurement) and dynamic (1 THz) conductivities increase with applied magnetic field, see Fig. 6.6. The d.c. magnetoconductivity at 50 K (not shown) is almost identical to the 200 K data although the noise level increases at this temperature. Fig. 6.5 shows that the THz conductivity is not strongly dependent on frequency up to 8 T in the range 0.2–2.2 THz. A $200 \Omega^{-1}\text{cm}^{-1}$ increase in conductivity at 1 THz can be seen under an applied magnetic field of 8 T. The d.c. magnetoresistance (MR) of the LSMO:ZnO film is $\frac{\Delta\rho}{\rho_0} = -2.6\%$ at 1 T. For comparison, the THz MR is $\sim -17\%$, significantly larger.

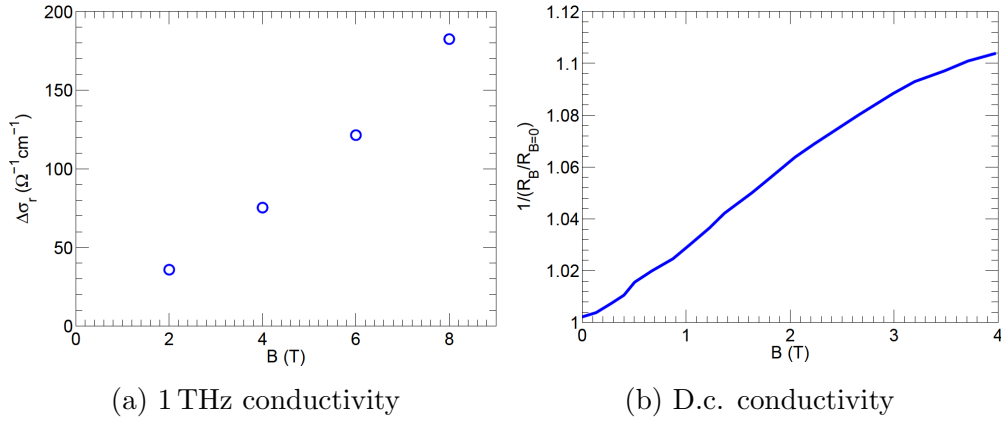


Figure 6.6: **Static and dynamic magnetoconductivity at 200 K.** (a) Change in conductivity at 1 THz as a function of magnetic field relative to zero-field THz conductivity. (b) Static conductivity at 200 K normalized by the zero-field static conductivity.

6.5 Pump-probe conductivity

In order to explore the dynamics of mobile charges in the LSMO:ZnO film, time resolved 1.55 eV-pump, THz-probe measurements were performed. Fig. 6.7 shows the change in transmitted THz electric field $\Delta E/E$ as a function of delay after the arrival of the pump beam at $t = 0$. InAs, a well known direct band gap semiconductor, is shown for comparison [182; 183]. In InAs, photoexcited carriers are promoted to the conduction band thereby increasing conductivity resulting in greater absorption of THz radiation, smaller transmitted THz electric field and therefore positive photoconductivity via Eqn. 3.16. After an initial rapid increase in InAs, the photoconductivity decays back to its pre-pump value on a nanosecond timescale as electrons and holes recombine. In LSMO:ZnO the conductivity actually decreases on application of the pump pulse, as can be seen because $\Delta E/E < 0$. This will be discussed later in Section 6.6. Unusually, LSMO:ZnO exhibits not only negative photoconductivity, but a long lifetime with the magnitude of the photoconductivity still increasing up to 500 ps. The inset

to Fig. 6.7(b) is a semilog plot of $\Delta E/E$ showing fits to the initial short-lived increase in the magnitude of the photoconductivity with a lifetime of 50 ps and the slower later increase with a lifetime of 1.2 ns. The decay of the photoconductivity back to zero occurs on a timescale longer than scanned in this experiment, but constrained to be less than 200 μs due to the repetition rate of the laser. The two lifetimes suggest two distinct processes occur immediately after photoexcitation and before the maximum photoconductivity is reached at 500 ps.

6.6 Discussion

The metal-insulator transition in the CMR manganites has been widely described as a transition from a poorly-conducting paramagnet to a ferromagnetic metal [72–74]. For $T < T_{\text{MI}}$ electrons in the e_g orbital can hop between Mn ions under the double exchange mechanism described in Section 1.3. Above T_{MI} , the electron-phonon coupling, dominated by a dynamic Jahn-Teller effect, localises the electrons as polarons. Models using these ideas can qualitatively reproduce the resistivity and magnetoresistance data [184]. More sophisticated models exist but will not be discussed here as this simple description is sufficient for our purpose [72–74].

Both $\Delta\sigma_r(1\text{ THz}) = \sigma_T - \sigma_{10\text{ K}}$ and $\rho_T/\rho_{10\text{ K}}(\text{d.c.})$ show the same trend of increasing conductivity as the temperature is reduced below T_{MI} down to low temperatures. The magnetisation increases below the ordering temperature as spin fluctuations about the ground state decrease, reducing magnetic scattering of the itinerant electrons and therefore increasing the conductivity [185].

The THz transmission spectra are consistent with a shift from Drude-like conductivity at low temperatures, with the characteristic peak at zero frequency,

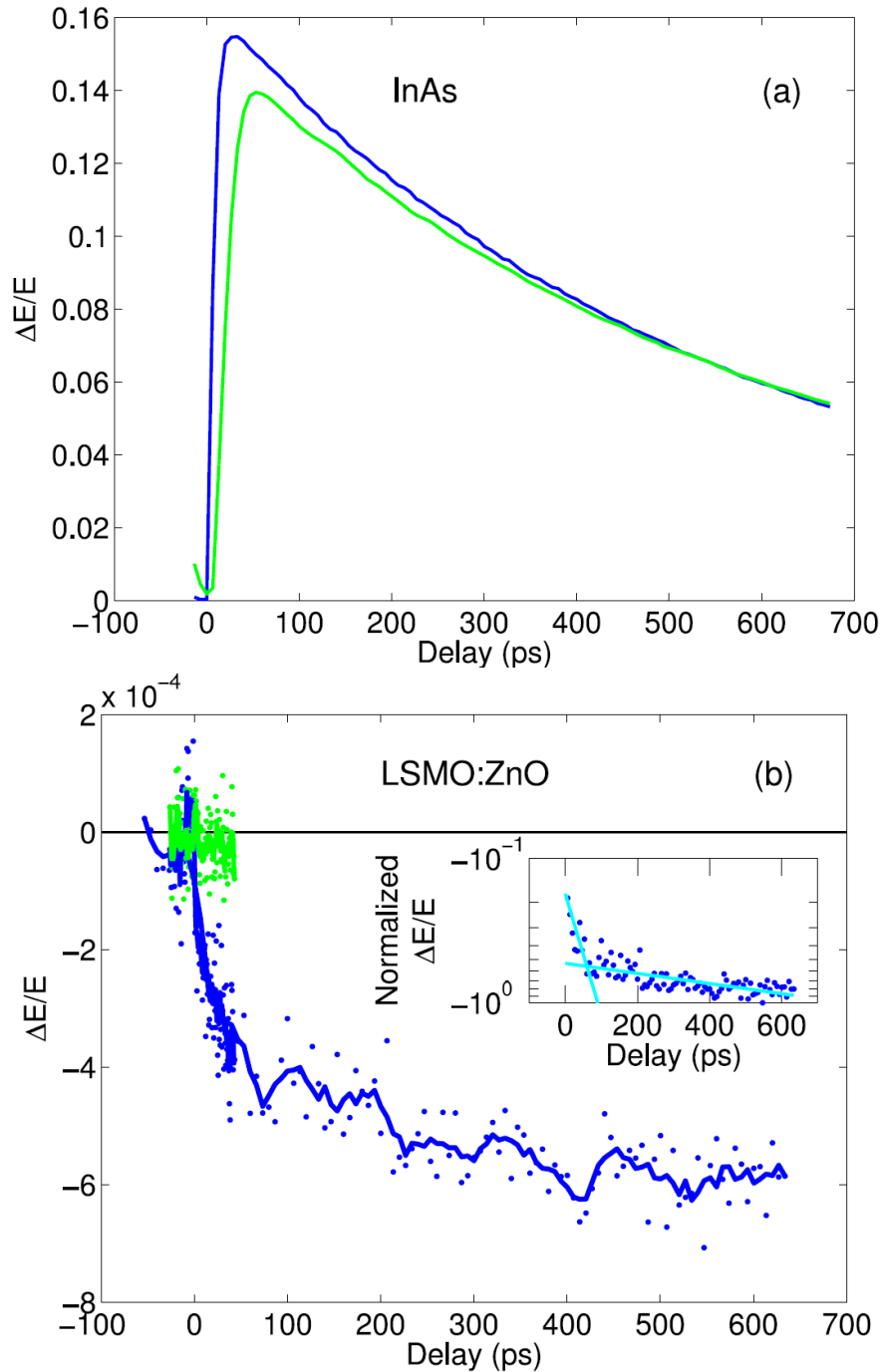


Figure 6.7: **Pump-induced change in THz electric field $\Delta E/E$** as a function of delay after photoexcitation at $t = 0$. Photoexcitation in InAs was measured at room temperature (green) and 200 K (blue). For the same pump fluence, the change in $\Delta E/E$ is over 200 times smaller for LSMO:ZnO at 200 K [blue line and points in (b)] in comparison to InAs [blue line and points in (a)], and is too small to measure at room temperature [green line and points in (b)].

to a more polaron-like conductivity at higher temperatures, as reported elsewhere for pure LSMO thin films [181; 186; 187]. The peak at low frequency in the transmission spectrum at 293 K is indicative of a reduction in conductivity at low frequency. The broad dip in conductivity in the spectra towards higher temperatures shows the incipient polaron-like peak forming over a background of increasing conductivity across the measured frequency range. It should be noted that no spectra were taken above the metal-insulator transition and so the full strength of the polaron peak will not be evident from these measurements. Certainly we can say that the LSMO:ZnO nanocolumn films show broadly the same behaviour in the THz range as has been previously reported for pure LSMO films [188].

Magnetoresistance in the manganites can be treated in terms of two distinct regimes; close to T_{MI} where the MR is often strongly peaked, and below the transition where the MR is more weakly temperature dependent and often proportional to the magnetisation - sometimes called 'LFMR regime' [178]. That the d.c. MR is essentially unchanged on cooling from 200 K to 50 K suggests that this is in the 'LFMR regime' for the $\text{La}_{0.7}\text{Sr}_{0.3}\text{MnO}_3\text{:ZnO}$ nanocolumn films, and the properties at 200 K are unrelated to the transition. The MR is dependent on extrinsic sample properties such as grain size. That means for a given composition, applied field and temperature the magnetoresistance will be largely determined by grain boundaries. This means that one can exert good control over the resistivity if one can control the morphology of the film [189]. When grain boundaries are the dominant factor in determining the resistivity, then it is discussed in terms of spin polarised tunneling [178]. A recent paper on a similar system, $\text{La}_{0.7}\text{Sr}_{0.3}\text{MnO}_3\text{:ZnO}$ nanocolumn films grown on SrTiO_3 , used a parallel connection channel model to find that the resistivity of the ZnO phase was

three orders of magnitude larger than the LSMO phase [68]. Measurements of the THz conductivity of ZnO and our THz conductivity measurements suggest this is applicable to our films too [190], meaning that the semiconducting ZnO phase can essentially be regarded as insulating when thinking about the conduction pathways in our samples.

The d.c. magnetoresistance of 2.6 % seen in our LSMO:ZnO film is comparable to those previously reported in a study on the growth of similar films and is larger than some pure LSMO films [68]. However the change in optical conductivity $\sim 500 \Omega^{-1} \text{cm}^{-1}$ is much smaller than that reported in pure LSMO films on LAO ($\sim 10000 \Omega^{-1} \text{cm}^{-1}$) [181] suggesting that the effects of the nanocolumns may in fact be greater on the optical conductivity than on the d.c. conductivity. This can be attributed to the fact that ZnO phases provide barriers to macroscopic electron transport.

The photoconductivity experiment exposes more contrasts between LSMO:ZnO nanocolumn samples and pure LSMO films. In pure LSMO, Averitt *et al.* [181] measured a negative photoconductivity with two characteristic timescales. They saw a short (~ 2 ps) reduction in photoconductivity which stayed roughly constant over the temperature range 0–350 K, attributed to an optically induced modification of the effective phonon temperature. A further reduction in photoconductivity took place over a longer timescale due to spin-lattice relaxation processes caused by spin-orbit coupling and momentum scattering. The timescale of the slower process varied from 5 ± 3 ps at 100 K to 50 ± 15 ps at 350 K - a maximum at around T_{MI} . We see an initial change in $\Delta\sigma$ on a ‘short’ timescale of 50 ps at 200 K and then a further reduction on a timescale of 1.2 ns before the conductivity flattens and subsequently decreases back to its equilibrium value.

6.7 Summary

Preliminary investigations of epitaxial $\text{La}_{0.7}\text{Sr}_{0.3}\text{MnO}_3\text{:ZnO}$ self-assembled vertically-aligned nanocomposite thin-films grown on LaAlO_3 (001) substrates have shown interesting differences between static and dynamic conductivities. X-ray diffraction revealed that the films are under compression in the plane of the substrate and in tension out of the plane, unlike LSMO:ZnO films on substrates such as STO. D.c. resistivity data determined that $T_{\text{MI}} \sim 300$ K. The conductivity monotonically increases below T_{MI} down to 10 K in both a.c. and d.c. measurements. The magnitude of the a.c. conductivity change is twice as large as the d.c. change. MR is also larger at THz frequencies than static, by a factor of six at 200 K and 1 T.

Further measurements are needed to fully understand the results presented in this chapter. Specifically, a reference sample of identical LAO substrate is necessary in order to accurately extract absolute rather than just relative conductivities. LAO is not an ideal substrate for THz measurements due to its strong birefringence and frequency and temperature dependent refractive index due to the lowest TO phonon [191]. Determination of absolute conductivities would enable modelling and thus quantitative comparison with other systems. Above room temperature measurements would provide information about the high temperature phase and magnetisation measurements will determine T_{C} .

Chapter 7

Conclusions

To conclude this thesis I will briefly summarise the key results, putting them in context of the wider research programme, and outlining some possible directions for further work to build on the foundations laid herein.

Chapter 4 reported an investigation of the dynamic magnetoelectric response of the multiferroic CuO. An electromagnon, at the highest temperature for an induced ferroelectric multiferroic as far as I am aware at the time of writing, was discovered and attributed to spin-lattice coupling between different Cu sublattices. The selection rules of the electromagnon and also a magnon in the antiferromagnetic phase were characterised. Room temperature electromagnons present an exciting opportunity for novel device applications and this work has been a significant step in this direction. Finding an electromagnon at such an elevated temperature compared to those previously studied in the multiferroic manganite systems immediately begs two questions:

- What exactly is the microscopic mechanism for this electromagnon?
- Can CuO be manipulated in order to further increase the temperature of

the multiferroic phase?

During the time of writing this thesis neutron scattering data providing dispersion relations along all pertinent directions of the Brillouin-zone became available and a Hamiltonian describing the collinear AFM phase has been successfully tested against these (unpublished) results [192]. Now it will be possible to extend this model in the manner described in Chapter 2 to find a theoretical description of the electromagnon.

Chapter 5 largely describes an attempt at the challenge set out by the second question. Theoretical predictions of a dramatic enhancement of the magnetic ordering temperature due to hydrostatic and chemical pressure had been made by others. Single crystals of $\text{Cu}_{1-x}\text{Zn}_x\text{O}$ were grown for $x < 0.05$. The effects of non-magnetic substitution on unit cell parameters, phonons, magnons, and electromagnons was investigated. A reduction in T_N was discussed in terms of spin dilution and a broadening of the multiferroic phase was observed. The large spin-lattice coupling of the A_u^3 phonon was preserved on substitution highlighting its importance at the magnetic transition.

Further work along these lines raises the possibility of combining the observed temperature-broadening of the multiferroic phase with higher transition temperatures, which is particularly exciting. Unfortunately there are no other $S = 1/2$ divalent transition metal or rare earth ions, preventing a clean investigation of chemical pressure alone, without the effects of spin dilution. However, replacing Cu with Mn for example could be a fruitful candidate for a non-spin diluted alloy. Despite the difficulties of growing monoclinic thin films, this has been achieved for CuO on a silicon substrate [193] and could also be an interesting route for investigating the effects of strain on multiferroic properties.

Chapter 6 is an investigation into the effect not only of substrate-induced

strain, but also vertical strain introduced through a second phase in epitaxial thin films made by pulsed laser deposition. Magnetoresistance in the half-metallic manganites is a very timely topic with potential implications for many varieties of spintronic devices. The metal insulator transition temperature of $\text{La}_{0.7}\text{Sr}_{0.3}\text{MnO}_3:\text{ZnO}$ films on LaAlO_3 substrates was determined from the static resistivity. Magnetoresistance was found to be significantly larger at 1 THz than in static measurements, highlighting the difference between macroscopic and local conductivity in these compounds, where grain boundaries and phase separation are of key importance.

Extending the study to encompass the effect of deposition frequency (which determines grain size) and epitaxial strain on the resistivity and magnetoresistivity would be of great benefit in the process of materials design and optimisation for incorporation of this class of material into working devices.

Bibliography

- [1] P. Babkevich, A. Poole, R. D. Johnson, B. Roessli, D. Prabhakaran, and A. T. Boothroyd, *Phys. Rev. B* **85**, 134428 (2012).
- [2] Y. Tokura and H. Y. Hwang, *Nat. Mater.* **7**, 694 (2008).
- [3] I. Osborne, M. Lavine, and R. Coontz, *Science* **327**, 1595 (2010).
- [4] M. Bibes and A. Barthelemy, *IEEE Trans. Electron Devices* **54**, 1003 (2007).
- [5] A. Kumar, R. S. Katiyar, and J. F. Scott, *IEEE Trans. Ultrason. Ferroelectr. Freq. Control* **57**, 2237 (2010).
- [6] W. Eerenstein, N. D. Mathur, and J. F. Scott, *Nature* **442**, 759 (2006).
- [7] E. Fatuzzo and W. J. Merz, *Ferroelectricity* (North-Holland Publishing Co., Amsterdam, Netherlands, 1967).
- [8] I. Dzyaloshinsky, *J. Phys. Chem. Solids* **4**, 241 (1958).
- [9] T. H. O'Dell, *The Electrodynamics of Magneto-Electric Media* (North-Holland Publishing Co., Amsterdam, Netherlands, 1970) ISBN 7204-1461.
- [10] K. F. Wang, J. M. Liu, and Z. F. Ren, *Adv. Phys.* **58**, 321 (2009).
- [11] E. Ascher, H. Rieder, H. Schmid, and H. Stossel, *J. Appl. Phys.* **37**, 1404 (1966).
- [12] H. Schmid, *Ferroelectrics* **162**, 317 (1994).
- [13] van Aken, J. P. Rivera, H. Schmid, and M. Fiebig, *Nature* **449**, 702 (2007).
- [14] M. E. Lines and A. M. Glass, *Principles and Applications of Ferroelectrics and Related Materials* (Oxford University Press, Great Clarendon Street, Oxford OX2 6DP, 1977) ISBN 0-19-850778-X.
- [15] N. Kida, Y. Takahashi, J. S. Lee, R. Shimano, Y. Yamasaki, Y. Kaneko, S. Miyahara, N. Furukawa, T. Arima, and Y. Tokura, *J. Opt. Soc. Am. B-Opt. Phys.* **26**, A35 (2009).

-
- [16] S. J. Blundell, *Magnetism in Condensed Matter* (Oxford University Press, Great Clarendon Street, Oxford OX2 6DP, 2001) ISBN 0-19-850591-4.
- [17] R. E. Newnham, *Properties of Materials* (Oxford University Press, Great Clarendon Street, Oxford OX2 6DP, 2005) ISBN 0-19-852076-x.
- [18] N. A. Hill, *J. Phys. Chem. B* **104**, 6694 (2000).
- [19] C. Ederer and N. A. Spaldin, *Phys. Rev. B* **76**, 214404 (2007).
- [20] E. Ressouche, M. Loire, V. Simonet, R. Ballou, A. Stunault, and A. Wildes, *Phys. Rev. B* **82**, 100408 (2010).
- [21] D. Khomskii, *Phys* **2**, 1 (2009).
- [22] J. T. Zhang, X. M. Lu, J. Zhou, H. Sun, F. Z. Huang, and J. S. Zhu, *Phys. Rev. B* **87**, 075127 (2013).
- [23] S. Y. Yang, L. W. Martin, S. J. Byrnes, T. E. Conry, S. R. Basu, D. Paran, L. Reichertz, J. Ihlefeld, C. Adamo, A. Melville, Y. H. Chu, C. H. Yang, J. L. Musfeldt, D. G. Schlom, J. W. Ager, and R. Ramesh, *Appl. Phys. Lett.* **95**, 062909 (2009).
- [24] M. Gajek, M. Bibes, S. Fusil, K. Bouzehouane, J. Fontcuberta, A. E. Barthelemy, and A. Fert, *Nat. Mater.* **6**, 296 (2007).
- [25] G. Lawes and G. Srinivasan, *J. Phys. D-Appl. Phys.* **44**, 243001 (2011).
- [26] A. Shuvaev, V. Dziom, A. Pimenov, M. Schiebl, A. A. Mukhin, A. C. Komarek, T. Finger, M. Braden, and A. Pimenov, *Phys. Rev. Lett.* **111**, 227201 (2013).
- [27] P. Rovillain, R. de Sousa, Y. Gallais, A. Sacuto, M. A. Measson, D. Colson, A. Forget, M. Bibes, A. Barthelemy, and M. Cazayous, *Nat. Mater.* **9**, 975 (2010).
- [28] M. P. Kostylev, A. A. Serga, T. Schneider, B. Leven, and B. Hillebrands, *Appl. Phys. Lett.* **87**, 153501 (2005).
- [29] H. Schmid, *J. Phys.-Condes. Matter* **20**, 434201 (2008).
- [30] M. Fiebig, *J. Phys. D-Appl. Phys.* **38**, R123 (2005).
- [31] A. Pimenov, T. Rudolf, F. Mayr, A. Loidl, A. A. Mukhin, and A. M. Balbashov, *Phys. Rev. B* **74**, 100403 (2006).
- [32] A. Pimenov, A. A. Mukhin, V. Y. Ivanov, V. D. Travkin, A. M. Balbashov, and A. Loidl, *Nat. Phys.* **2**, 97 (2006).

-
- [33] T. Kimura, G. Lawes, T. Goto, Y. Tokura, and A. P. Ramirez, *Phys. Rev. B* **71**, 224425 (2005).
- [34] D. Sedff, P. Link, N. Aliouane, D. N. Argyriou, and M. Braden, *Phys. Rev. B* **77**, 174419 (2008).
- [35] D. Senff, N. Aliouane, D. N. Argyriou, A. Hiess, L. P. Regnault, P. Link, K. Hradil, Y. Sidis, and M. Braden, *J. Phys.-Condes. Matter* **20**, 434212 (2008).
- [36] N. Kida, Y. Yamasaki, R. Shimano, T. Arima, and Y. Tokura, *J. Phys. Soc. Jpn.* **77**, 123704 (2008).
- [37] R. Vald'es Aguilar, M. Mostovoy, A. B. Sushkov, C.-L. Zhang, Y. J. Choi, S. W. Cheong, and H. D. Drew, *Phys. Rev. Lett.* **102**, 047203 (2009).
- [38] A. Pimenov, A. Shuvaev, A. Loidl, F. Schrettle, A. A. Mukhin, V. D. Travkin, V. Y. Ivanov, and A. M. Balbashov, *Phys. Rev. Lett.* **102**, 107203 (2009).
- [39] P. Rovillain, M. Cazayous, Y. Gallais, A. Sacuto, M. A. Measson, and H. Sakata, *Phys. Rev. B* **81**, 054428 (2010).
- [40] Y. Takahashi, Y. Yamasaki, N. Kida, Y. Kaneko, T. Arima, R. Shimano, and Y. Tokura, *Phys. Rev. B* **79**, 214431 (2009).
- [41] H. Katsura, A. V. Balatsky, and N. Nagaosa, *Phys. Rev. Lett.* **98**, 027203 (2007).
- [42] A. Pimenov, A. M. Shuvaev, A. A. Mukhin, and A. Loidl, *J. Phys.-Condes. Matter* **20**, 434209 (2008).
- [43] M. Mochizuki, N. Furukawa, and N. Nagaosa, *Phys. Rev. Lett.* **105**, 037205 (2010).
- [44] R. Vald'es Aguilar, A. B. Sushkov, C.-L. Zhang, Y. J. Choi, S. W. Cheong, and H. D. Drew, *Phys. Rev. B* **76**, 060404 (2007).
- [45] A. Pimenov, A. Loidl, A. A. Mukhin, V. D. Travkin, V. Y. Ivanov, and A. M. Balbashov, *Phys. Rev. B* **77**, 014438 (2008).
- [46] J. S. Lee, N. Kida, S. Miyahara, Y. Takahashi, Y. Yamasaki, R. Shimano, N. Furukawa, and Y. Tokura, *Phys. Rev. B* **79**, 180403 (2009).
- [47] Y. Takahashi, S. Ishiwata, S. Miyahara, Y. Kaneko, N. Furukawa, Y. Taguchi, R. Shimano, and Y. Tokura, *Phys. Rev. B* **81**, 100413 (2010).

-
- [48] A. B. Sushkov, R. Valdés Aguilar, S. Park, S. W. Cheong, and H. D. Drew, *Phys. Rev. Lett.* **98**, 027202 (2007).
- [49] C. Fang and J. P. Hu, *EPL* **82**, 57005 (2008).
- [50] A. B. Sushkov, M. Mostovoy, R. Valdés Aguilar, S. W. Cheong, and H. D. Drew, *J. Phys.-Condes. Matter* **20**, 434210 (2008).
- [51] D. Huvonen, U. Nagel, T. Room, Y. J. Choi, C.-L. Zhang, S. Park, and S. W. Cheong, *Phys. Rev. B* **80**, 100402 (2009).
- [52] C. Fang, T. Datta, and J. P. Hu, *Phys. Rev. B* **79**, 014107 (2009).
- [53] N. Kida, D. Okuyama, S. Ishiwata, Y. Taguchi, R. Shimano, K. Iwasa, T. Arima, and Y. Tokura, *Phys. Rev. B* **80**, 220406 (2009).
- [54] S. Seki, N. Kida, S. Kumakura, R. Shimano, and Y. Tokura, *Phys. Rev. Lett.* **105**, 097207 (2010).
- [55] I. Kezsmarki, N. Kida, H. Murakawa, S. Bordacs, Y. Onose, and Y. Tokura, *Phys. Rev. Lett.* **106**, 057403 (2011).
- [56] T. Kubacka, J. A. Johnson, M. C. Hoffmann, C. Vicario, P. Beaud, S. Grubel, S. W. Huang, L. Huber, L. Patthey, Y. D. Chuang, J. J. Turner, G. L. Dakovski, W. S. Lee, M. P. Minitti, W. Schlotter, R. G. Moore, C. P. Hauri, S. M. Koohpayeh, and V. Scagnoli, *Science* **343**, 1333 (2014).
- [57] N. Kida and Y. Tokura, *J. Magn. Magn. Mater.* **324**, 3512 (2012).
- [58] V. N. Krivoruchko, *Low Temp. Phys.* **38**, 807 (2012).
- [59] G. H. Jonker and J. van Santen, *Physica* **16**, 337 (1950).
- [60] Web Of Science search for: TOPIC = manganites* on 03/06/2014.
- [61] J. van Santen and G. H. Jonker, *Physica* **16**, 599 (1950).
- [62] J. Volger, *Physica* **20**, 49 (1954).
- [63] E. O. Wollan and W. C. Koehler, *Phys. Rev.* **100**, 545 (1955).
- [64] C. Zener, *Phys. Rev.* **82**, 403 (1951).
- [65] S. Jin, T. H. Tiefel, M. McCormack, R. A. Fastnacht, R. Ramesh, and L. H. Chen, *Science* **264**, 413 (1994).
- [66] A. Urushibara, Y. Moritomo, T. Arima, A. Asamitsu, G. Kido, and Y. Tokura, *Phys. Rev. B* **51**, 14103 (1995).

- [67] B. Wiedenhorst, C. Hofener, Y. F. Lu, J. Klein, M. S. R. Rao, B. H. Freitag, W. Mader, L. Alff, and R. Gross, *J. Magn. Magn. Mater.* **211**, 16 (2000).
- [68] A. Chen, Z. Bi, C. Tsai, J. Lee, Q. Su, X. Zhang, Q. Jia, J. L. MacManus-Driscoll, and H. Wang, *Adv. Funct. Mater.* **21**, 2423 (2011).
- [69] M. Bowen, J. L. Maurice, A. Barthelemy, M. Bibes, D. Imhoff, V. Bellini, R. Bertacco, D. Wortmann, P. Seneor, E. Jacquet, A. Vaures, J. Humbert, J. P. Contour, C. Colliex, S. Blugel, and P. H. Dederichs, *J. Phys.-Condes. Matter* **19**, 315208 (2007).
- [70] L. E. Hueso, J. M. Pruneda, V. Ferrari, G. Burnell, J. P. Valdes-herrera, B. D. Simons, P. B. Littlewood, E. Artacho, A. Fert, and N. D. Mathur, *Nature* **445**, 410 (2007).
- [71] X. Moya, L. E. Hueso, F. Maccherozzi, A. I. Tovstolytkin, D. I. Podyalovskii, C. Ducati, L. C. Phillips, M. Ghidini, O. Hovorka, A. Berger, M. E. Vickers, E. Defay, S. S. Dhesei, and N. D. Mathur, *Nat. Mater.* **12**, 52 (2013).
- [72] E. Dagotto, *Nanoscale Phase Seperation and Colossal Magneto-resistance* (Springer, Heidelberg, Germany, 2003) ISBN 3-540-43245-0.
- [73] Y. Tokura, *Rep. Prog. Phys.* **69**, 797 (2006).
- [74] D. M. Edwards, *Adv. Phys.* **51**, 1259 (2002).
- [75] D. N. Basov, R. D. Averitt, D. van der Marel, M. Dressel, and K. Haule, *Rev. Mod. Phys.* **83**, 471 (2011).
- [76] A. Shuvaev, "Spectroscopic study of manganites with magnetoelectric coupling," (2012).
- [77] L. D. Landau and E. M. Lifshitz, *Phys. Zeitsch. der Sow.*(1935).
- [78] T. L. Gilbert, *IEEE Trans. Magn.* **40**, 3443 (2004).
- [79] C. Kittel, *Introduction to Solid State Physics* (Wiley, 1953).
- [80] M. Nauciel-Bloch, A. Castets, and G. Sarma, *Phys. Rev. B* **5**, 4603 (1972).
- [81] H. Katsura, N. Nagaosa, and A. V. Balatsky, *Phys. Rev. Lett.* **95**, 057205 (2005).
- [82] I. A. Sergienko and E. Dagotto, *Phys. Rev. B* **73**, 094434 (2006).
- [83] T. Moriya, *Phys. Rev.* **120**, 91 (1960).

-
- [84] M. Mochizuki, N. Furukawa, and N. Nagaosa, *Phys. Rev. Lett.* **104**, 177206 (2010).
- [85] J. Lloyd-Hughes and T.-I. Jeon, *J Infrared Milli Terahz Waves* **33**, 871 (2012).
- [86] G. P. Williams, *Rep. Prog. Phys.* **69**, 301 (2006).
- [87] B. P. Gorshunov, A. A. Volkov, A. S. Prokhorov, and I. E. Spektor, *Phys. Solid State* **50**, 2001 (2008).
- [88] I. Hosako, N. Sekine, M. Patrashin, S. Saito, K. Fukunaga, Y. Kasai, P. Baron, T. Seta, J. Mendrok, S. Ochiai, and H. Yasuda, *Proc. IEEE* **95**, 1611 (2007).
- [89] C. A. Schmuttenmaer, *Chem. Rev.* **104**, 1759 (2004).
- [90] P. R. Smith, D. H. Auston, and M. C. Nuss, *IEEE J. Quantum Electron.* **24**, 255 (1988).
- [91] C. Fattinger and D. Grischkowsky, *Appl. Phys. Lett.* **53**, 1480 (1988).
- [92] M. C. Beard, G. M. Turner, and C. A. Schmuttenmaer, *J. Phys. Chem. B* **106**, 7146 (2002).
- [93] For example, the TPS spectra 3000 made by Teraview.
- [94] M. Tonouchi, *Nat. Photon.* **1**, 97 (2007).
- [95] I. R. Kenyon, *The Light Fantastic* (Oxford University Press, Great Clarendon Street, Oxford OX2 6DP, 2008) ISBN 978-0-19-856645-8.
- [96] X.-C. Zhang, B. B. Hu, J. T. Darrow, and D. H. Auston, *Appl. Phys. Lett.* **56**, 1011 (1990).
- [97] B. Ferguson and X.-C. Zhang, *Nat. Mater.* **1**, 26 (2002).
- [98] L. Xu, X.-C. Zhang, and D. H. Auston, *Appl. Phys. Lett.* **61**, 1784 (1992).
- [99] N. Vagelatos, D. Wehe, and J. S. King, *J. Chem. Phys.* **60**, 3613 (1974).
- [100] A. S. Barker, *Phys. Rev.* **165**, 917 (1968).
- [101] D. F. Nelson and E. H. Turner, *J. Appl. Phys.* **39**, 3337 (1968).
- [102] Kaye and L. Online, "Tables of physical & chemical constants. 2.5.11 electro-optic materials.." (2008).

-
- [103] M. van Exter, C. Fattinger, and D. Grischkowsky, *Opt. Lett.* **14**, 1128 (1989).
- [104] Q. Wu and X.-C. Zhang, *Appl. Phys. Lett.* **67**, 3523 (1995).
- [105] A. B. Kuzmenko, *Guide to Reffit: Software to fit Optical Spectra*, <http://optics.unige.ch/alexey/reffit.html> (2004).
- [106] D. Harris and M. Bertolucci, *Symmetry and Spectroscopy* (Oxford University Press, Great Clarendon Street, Oxford OX2 6DP, 1978) ISBN 0-19-502001-4.
- [107] M. Cardona, *Light Scattering in Solids* (Springer Verlag, Berlin, Germany, 1975).
- [108] C. M. Foster, M. Grimsditch, Z. Li, and V. G. Karpov, *Phys. Rev. Lett.* **71**, 1258 (1993).
- [109] T. Kimura, Y. Sekio, H. Nakamura, T. Siegrist, and A. P. Ramirez, *Nat. Mater.* **7**, 291 (2008).
- [110] J. B. Forsyth, P. J. Brown, and B. M. Wanklyn, *J. Phys. C: Solid State Phys.* **21**, 2917 (1988).
- [111] M. Ain, A. Menelle, B. M. Wanklyn, and E. F. Bertaut, *J. Phys.-Condes. Matter* **4**, 5327 (1992).
- [112] G. X. Jin, K. Cao, G. C. Guo, and L. X. He, *Phys. Rev. Lett.* **108**, 187205 (2012).
- [113] M. Ain, W. Reichardt, B. Hennion, G. Pepy, and B. M. Wanklyn, *Physica C* **162**, 1279 (1989).
- [114] D. A. Yablonskii, *Physica C* **171**, 454 (1990).
- [115] F. Wang, T. Zou, Y. Liu, L. Q. Yan, and Y. Sun, *J. Appl. Phys.* **110**, 054106 (2011).
- [116] G. Giovannetti, S. Kumar, A. Stroppa, J. van den Brink, S. Picozzi, and J. Lorenzana, *Phys. Rev. Lett.* **106**, 026401 (2011).
- [117] P. Toledano, N. Leo, D. D. Khalyavin, L. C. Chapon, T. Hoffmann, D. Meier, and M. Fiebig, *Phys. Rev. Lett.* **106**, 257601 (2011).
- [118] R. Villarreal, G. Quirion, M. L. Plumer, M. Poirier, T. Usui, and T. Kimura, *Phys. Rev. Lett.* **109**, 167206 (2012).

-
- [119] T. Hoffmann, K. Kimura, T. Kimura, and M. Fiebig, *J. Phys. Soc. Jpn.* **81**, 124714 (2012).
- [120] X. Rocquefelte, K. Schwarz, P. Blaha, and S. Kumar, *Nat. Commun.* **4**, 2511 (2013).
- [121] S. R. Å sbrink and L. J. Norrby, *Acta Cryst. B* **26**, 8 (1970).
- [122] D. Prabhakaran and A. T. Boothroyd, *J. Cryst. Growth* **250**, 77 (2003).
- [123] S. Wilkins, “Q-laue,” (2010), <http://sourceforge.net/projects/qlaue/>.
- [124] A. B. Kuz'menko, D. van der Marel, P. van Bentum, E. A. Tishchenko, C. Presura, and A. A. Bush, *Phys. Rev. B* **63**, 094303 (2001).
- [125] C. C. Homes, M. Ziaei, B. P. Clayman, J. C. Irwin, and J. P. Franck, *Phys. Rev. B* **51**, 3140 (1995).
- [126] J. van Kranendonk and J. van Vleck, *Rev. Mod. Phys.* **30**, 1 (1958).
- [127] K. I. Doig, F. Aguesse, A. K. Axelsson, N. M. Alford, S. Nawaz, V. R. Palkar, S. P. P. Jones, R. D. Johnson, R. A. Synowicki, and J. Lloyd-Hughes, *Phys. Rev. B* **88**, 094425 (2013).
- [128] A. M. Shuvaev, V. D. Travkin, V. Y. Ivanov, A. A. Mukhin, and A. Pimenov, *Phys. Rev. Lett.* **104**, 097202 (2010).
- [129] N. Kida, Y. Ikebe, Y. Takahashi, J. P. He, Y. Kaneko, Y. Yamasaki, R. Shimanoto, T. Arima, N. Nagaosa, and Y. Tokura, *Phys. Rev. B* **78**, 104414 (2008).
- [130] K. Cao, G. C. Guo, and L. X. He, *J. Phys.-Condes. Matter* **24**, 206001 (2012).
- [131] A. Pimenov, M. Biberacher, D. Ivannikov, A. Loidl, A. A. Mukhin, Y. G. Goncharov, and A. M. Balbashov, *Phys. Rev. B* **73**, 220407 (2006).
- [132] P. Rovillain, M. Cazayous, Y. Gallais, M. A. Measson, A. Sacuto, H. Sakata, and M. Mochizuki, *Phys. Rev. Lett.* **107**, 027202 (2011).
- [133] M. Schmidt, C. Kant, T. Rudolf, F. Mayr, A. A. Mukhin, A. M. Balbashov, J. Deisenhofer, and A. Loidl, *Eur. Phys. J. B* **71**, 411 (2009).
- [134] D. S. Rodbell, E. A. Harris, J. Owen, and I. S. Jacobs, *Phys. Rev. Lett.* **11**, 10 (1963).

- [135] T. Moriyasu, S. Wakabayashi, and T. Kohmoto, *J Infrared Milli Terahz Waves* **34**, 277 (2013).
- [136] S. L. Johnson, R. A. de Souza, U. Staub, P. Beaud, Móhr-Vorobeva, G. Ingold, A. Caviezel, V. Scagnoli, W. F. Schlotter, J. J. Turner, O. Krupin, W. S. Lee, Y. D. Chuang, L. Patthey, R. G. Moore, D. Lu, M. Yi, P. S. Kirchmann, and M. Trigo, *Phys. Rev. Lett.* **108**, 037203 (2012).
- [137] K. Pasrija and S. Kumar, *Phys. Rev. B* **88**, 144418 (2013).
- [138] A. T. Boothroyd, A. Mukherjee, S. Fulton, T. G. Perring, R. S. Eccleston, H. A. Mook, and B. M. Wanklyn, *Physica B* **234**, 731 (1997).
- [139] T. Shimizu, T. Matsumoto, A. Goto, T. V. C. Rao, K. Yoshimura, and K. Kosuge, *Phys. Rev. B* **68**, 224433 (2003).
- [140] S. Jung, J. Kim, E. J. Choi, Y. Seiko, T. Kimura, and J. Lorenzana, *Phys. Rev. B* **80**, 140516 (2009).
- [141] K. Y. Choi, W. J. Lee, A. Glamazda, P. Lemmens, D. Wulferding, Y. Sekio, and T. Kimura, *Phys. Rev. B* **87**, 184407 (2013).
- [142] H. Ohta, S. Okubo, T. Kobayashi, T. Sakurai, W. Zhang, C. Yokoyama, X. G. Zheng, S. Nishihara, K. Inoue, M. Fujisawa, H. Kikuchi, E. Matsuoka, and H. Sugawara, *IRMMW2012* **1**, 1 (2012).
- [143] P. Monod, A. A. Stepanov, V. A. Pashchenko, J. P. Vieren, G. Desgardin, and J. Jegoudez, *J. Magn. Magn. Mater.* **177**, 739 (1998).
- [144] R. M. Moon, T. Riste, and W. C. Koehler, *Phys. Rev.* **181**, 920 (1969).
- [145] W. Reichardt, F. Gompf, M. Ain, and B. M. Wanklyn, *Z. Phys. B-Condens. Mat.* **81**, 19 (1990).
- [146] F. Marabelli, G. B. Parravicini, and F. Salghettidrioli, *Phys. Rev. B* **52**, 1433 (1995).
- [147] P. Carretta, F. Cintolesi, and A. Rigamonti, *Phys. Rev. B* **49**, 7044 (1994).
- [148] T. I. Arbutova, I. B. Smolyak, S. V. Naumov, and A. A. Samokhvalov, *Phys. Solid State* **40**, 1702 (1998).
- [149] C. T. Meneses, J. G. S. Duque, L. G. Vivas, and M. Knobel, *J. Non-Cryst. Solids* **354**, 4830 (2008).
- [150] S. G. Yang, T. Li, B. X. Gu, Y. W. Du, H. Y. Sung, S. T. Hung, C. Y. Wong, and A. B. Pakhomov, *Appl. Phys. Lett.* **83**, 3746 (2003).

-
- [151] R. A. Borzi, S. J. Stewart, G. Punte, R. C. Mercader, G. A. Curutchet, R. D. Zysler, and M. Tovar, *J. Appl. Phys.* **87**, 4870 (2000).
- [152] P. Shah, A. Gupta, and D. K. Avasthi, *Nucl. Instrum. Methods Phys. Res. Sect. B-Beam Interact. Mater. Atoms* **152**, 343 (1999).
- [153] R. D. Shannon and C. T. Prewitt, *Acta C.* **25**, 925 (1969).
- [154] R. D. Shannon and C. T. Prewitt, *Acta Cryst. B* **26**, 1046 (1970).
- [155] S. P. P. Jones, S. M. Gaw, K. I. Doig, D. Prabhakaran, E. M. H. Wheeler, A. T. Boothroyd, and J. Lloyd-Hughes, *Nature Communications* **5**:3787(2014).
- [156] S. P. P. Jones, S. M. Gaw, K. I. Doig, D. Prabhakaran, E. Hétyroy Wheeler, A. T. Boothroyd, and J. Lloyd-Hughes, *Nat. Commun.* **5**, 3787 (2014).
- [157] X. G. Zheng, N. Tsutsumi, S. Tanaka, M. Suzuki, and C. N. Xu, *Physica C* **321**, 67 (1999).
- [158] D. L. Rousseau, R. P. Bauman, and S. P. S. Porto, *J. Raman Spectrosc.* **10**, 253 (1981).
- [159] S. N. Narang, V. B. Kartha, and N. D. Patel, *Physica C* **204**, 8 (1992).
- [160] G. Kliche and Z. V. Popovic, *Phys. Rev. B* **42**, 10060 (1990).
- [161] A. P. Litvinchuk, A. Möller, L. Debbichi, P. Krüger, M. N. Iliev, and M. M. Gospodinov, *J. Phys.-Condes. Matter* **25**, 105402 (2013).
- [162] X. K. Chen, J. C. Irwin, and J. P. Franck, *Phys. Rev. B* **52**, 13130 (1995).
- [163] B. X. Yang, J. M. Tranquada, and G. Shirane, *Phys. Rev. B* **38**, 174 (1988).
- [164] C. H. Lee, K. Kihou, K. Horigane, S. Tsutsui, T. Fukuda, H. Eisaki, A. Iyo, H. Yamaguchi, A. Q. R. Baron, M. Braden, and K. Yamada, *J. Phys. Soc. Jpn.* **79**, 014714 (2010).
- [165] M. Kall, A. P. Litvinchuk, L. Borjesson, P. Berastegui, and L. G. Johansson, *Phys. Rev. B* **53**, 3566 (1996).
- [166] H. Y. Xu, Y. C. Liu, C. S. Xu, Y. X. Liu, C. L. Shao, and R. Mu, *J. Chem. Phys.* **124**, 074707 (2006).
- [167] J. B. Wang, H. M. Zhong, Z. F. Li, and W. Lu, *J. Appl. Phys.* **97**, 086105 (2005).
- [168] C. Dupas and J. P. Renard, *Phys. Rev. B* **18**, 401 (1978).

-
- [169] D. Hone, P. A. Montano, T. Tonegawa, and Y. Imry, *Phys. Rev. B* **12**, 5141 (1975).
- [170] A. Paduan, C. C. Becerra, and F. Palacio, *Phys. Rev. B* **58**, 3197 (1998).
- [171] N. Fujiwara, J. R. Jeitler, C. Navas, M. M. Turnbull, T. Goto, and N. Hosoito, *J. Magn. Magn. Mater.* **140**, 1663 (1995).
- [172] A. L. Chernyshev, Y. C. Chen, and A. H. C. Neto, *Phys. Rev. B* **65**, 104407 (2002).
- [173] T. Edagawa, Y. Fukumoto, and A. Oguchi, *J. Magn. Magn. Mater.* **310**, E406 (2007).
- [174] N. Papinutto, P. Carretta, S. Gonthier, and P. Millet, *Phys. Rev. B* **71**, 174425 (2005).
- [175] C. L. Henley, *Phys. Rev. Lett.* **62**, 2056 (1989).
- [176] L. Meddar, M. Josse, P. Deniard, C. La, G. Andre, F. Damay, V. Petricek, S. Jobic, M. H. Whangbo, M. Maglione, and C. Payen, *Chem. Mat.* **21**, 5203 (2009).
- [177] B. S. Kang, H. Wang, J. L. MacManus-Driscoll, Y. Li, Q. X. Jia, I. Mihut, and J. B. Betts, *Appl. Phys. Lett.* **88**, 192514 (2006).
- [178] P. K. Siwach, H. K. Singh, and O. N. Srivastava, *J. Phys.-Condes. Matter* **20**, 273201 (2008).
- [179] Y. M. Kang, H. J. Kim, and S. I. Yoo, *Appl. Phys. Lett.* **95**, 052510 (2009).
- [180] O. Lee, S. A. Harrington, A. Kursumovic, E. Defay, H. Y. Wang, Z. X. Bi, C. F. Tsai, L. Yan, Q. X. Jia, and J. L. MacManus-Driscoll, *Nano Lett.* **12**, 4311 (2012).
- [181] R. D. Averitt, A. I. Lobad, C. Kwon, S. A. Trugman, V. K. Thorsmølle, and A. J. Taylor, *Phys. Rev. Lett.* **8701**, 017401 (2001).
- [182] D. E. Aspnes and A. A. Studna, *Phys. Rev. B* **27**, 985 (1983).
- [183] K. L. Vodopyanov, H. Graener, C. C. Phillips, and T. J. Tate, *Phys. Rev. B* **46**, 13194 (1992).
- [184] A. J. Millis, B. I. Shraiman, and R. Mueller, *Phys. Rev. Lett.* **77**, 175 (1996).
- [185] H. Y. Hwang, S. W. Cheong, and B. Batlogg, *Appl. Phys. Lett.* **68**, 3494 (1996).

-
- [186] M. Quijada, J. Cerne, J. R. Simpson, H. D. Drew, K. H. Ahn, A. J. Millis, R. Shreekala, R. Ramesh, M. Rajeswari, and T. Venkatesan, *Phys. Rev. B* **58**, 16093 (1998).
- [187] E. Saitoh, A. Asamitsu, Y. Okimoto, and Y. Tokura, *J. Phys. Soc. Jpn.* **69**, 3614 (2000).
- [188] R. D. Averitt and A. J. Taylor, *J. Phys.-Condes. Matter* **14**, R1357 (2002).
- [189] A. Anshul, S. S. Amritphale, S. Kaur, and R. Hada, *J. Mater. Sci. Technol.* **27**, 691 (2011).
- [190] J. B. Baxter and C. A. Schmuttenmaer, *Phys. Rev. B* **80**, 235205 (2009).
- [191] J. Lloyd-Hughes, S. P. P. Jones, E. Castro-Camus, K. I. Doig, and J. L. MacManus-Driscoll, *Opt. Lett.* **39**, 1121 (2014).
- [192] S. Gaw, private communication (May 2014).
- [193] A. P. Chen, G. Yang, H. Long, F. Li, Y. H. Li, and P. X. Lu, *Thin Solid Films* **517**, 4277 (2009).